

Good enough: Intermediate complexity atmospheric models improve the representation of processes affecting seasonal snow

Présentée le 21 juin 2024

Faculté de l'environnement naturel, architectural et construit
Laboratoire des sciences cryosphériques
Programme doctoral en génie civil et environnement

pour l'obtention du grade de Docteur ès Sciences

par

Dylan Stewart REYNOLDS

Acceptée sur proposition du jury

Prof. J. Chappellaz, président du jury
Prof. M. Lehning, Dr R. M. Mott-Grünewald, directeurs de thèse
Prof. C. Schär, rapporteur
Dr V. Vionnet, rapporteur
Prof. J. Schmale, rapporteuse

Eventually, all things merge into one,
and a river runs through it.
— Norman Maclean

To my family, I got pretty lucky...

Acknowledgements

This thesis has been a ride and there's a lot of people to thank.

Rebecca has been a fantastic advisor. You've always been happy to have a discussion and trusted me from the start. You knew when to push me further, and when I rather needed to relax. Your approach to research, and in particular your balance with life, is really something I aspire to. I might have quit if not for you.

My professor, Michi Lehning, has the rigor of a scientist and the curiosity of an artist. This is of course great for going on ski tours with, and has also lead to wonderful exchanges which have shaped the course of the research within this thesis.

My third, unofficial advisor, Michi Haugeneder, has also contributed immensely to this thesis by keeping me sane. Many of my best memories from Davos have been shared with you, and you've helped me to get through the lows and enjoy the highs.

I have been especially grateful for our meetings (Michi, Rebecca, Michi, and I), which would draw attention from down the hall due to the eruptive laughter.

Ethan Gutmann was kind enough to spend an hour each week for the first couple years meeting via zoom to discuss model development. To this, Bert Kruyt was helpful in setting up much of the development and testing environment which saved me months of time in the first year. Franziska Gerber was both an inspiration for, and great help consulting on, the high-resolution atmospheric modeling done in this thesis. I would like to thank Fanny Kristianti, Sebastian Hoch, and Franziska Gerber for their help in setting up the Wind LiDAR near Gaudergrat, and Moritz Oberrauch, Mahdi Jafari, and Michi Haugeneder for retrieving it in the late-season mud. Mahdi Jafari endured many untested commits and abrupt model changes with me, and we've shared as many nights in Montana. Louis Quéno helped a lot with the tuning and development of HICARsnow, and I am very thankful for his input.

To anyone who has ever written a line of open source python code, particularly the team working on xarray: science is built on your backs – thank you! Similarly, I want to thank the staff at CSCS who build, maintain, and deal with us users – you guys enable some really cool science.

I'm also grateful to the whole Snow Hydrology group at SLF, past and current, who made

Acknowledgements

me feel at home in Davos from Day 1 on. In particular I want to thank Giulia Mazzotti for her enthusiasm, which has been a source of inspiration professionally and recreationally throughout the thesis. Adam Winstal, Chris Hoyle, and Clare Webster showed me that you can build a life in a far away place, and I am thankful for their example. I'll thank Tobi here too, wherever he is, for sharing a few Christmases on some frozen island. You should write a book one day. There are many good friends and colleagues in Davos who have made these 4 years so enjoyable – too many to thank here. Michael Lombardo keeps me in line, except for when he doesn't, and I am grateful for both.

To my friends back home, thanks for getting me here. Mac, Alex, Dane, Andrew, I'm glad that we've stayed in touch over the distance, your friendships balance me. Justine, you make me excited for whatever happens next. Lastly, my family has supported me through this whole journey, not making the distance any harder on me. You guys are one of a kind.

Davos, 20 February 2024

D. R.

Abstract

Snow plays a crucial role in processes regulating ecosystems, the climate, and human development. Mountain snowpack in particular has great relevance for downstream communities. Knowledge about the distribution and properties of the snowpack thus help in planning how to live with this dynamic resource. Snow models employed to simulate mountain snowpack cover a range of physical complexity, but all of them are incredibly dependent on accurate input data. This input data must resolve relevant atmospheric processes at the scales at which snow models are run, often down to 100 m or higher. Processes such as preferential deposition of precipitation, where near-surface flow features and microphysical processes enhance precipitation at the ridge scale, should thus be accounted for. One of the best methods for providing snow models with input data is dynamic downscaling, where meteorological input data is calculated at the resolution of snow models using numerical weather prediction models. This technique has many advantages over statistical downscaling, with the large caveat that is it computationally unfeasible to perform over large areas or time scales. In this thesis, we introduce an intermediate-complexity atmospheric model, HICAR, capable of running at the resolution of most snowpack models. The HICAR model makes use of techniques developed in the field of pollutant transport to efficiently solve for a 3D wind field at the hectometer scale. The technique allows for direct modification of the wind field, enabling parameterizations of steady-state eddy-like structures and thermally driven slope flows. Validation of HICAR's flow fields against non-hydrostatic atmospheric models, as well as observations, demonstrate HICAR's ability to resolve flow features relevant to snowpack modeling. These improvements to the model flow field, in combination with improvements to the model's physics, result in accurate simulation of near-surface atmospheric variables. 2m air temperature, radiative inputs, and precipitation outputs of the model are evaluated against observations from automated weather stations and grided precipitation products. A process-level view of precipitation at the 50m scale is presented using a state-of-the-art microphysics scheme. Results from this evaluation reveal HICAR's ability to simulate preferential deposition of snow, and alter the understanding of the process to include the interaction of near-surface flow features with microphysical process. Finally, the relevancy of the model for snowpack modeling is addressed. HICAR is coupled with an intermediate complexity snow model, FSM2trans. This coupled model, HICARsnow, is shown to resolve patterns of snow accumulation and ablation through-

Acknowledgements

out the snow season. The ability of HICAR to simulate preferential deposition is shown to improve the distribution of snow depth in complex terrain relative to snow model runs using statistical downscaling of precipitation. Feedbacks from blowing snow sublimation on humidity also limit the rate of blowing snow sublimation over the winter season for the two-way coupled snow model compared to the snow model run with statistical downscaling. The arc of this thesis shows that intermediate-complexity atmospheric modeling at the hectometer scale is possible, that it is capable of resolving atmospheric variables relevant to land surface models, and that this translates to better process representation within snow models.

Key words: Atmospheric Modeling, Snow-Atmosphere Modeling, Wind Fields, Preferential Deposition, Evaluation, Intermediate-complexity Modeling, Complex Terrain, Wind LiDAR Scans, Surface Energy- and Mass Balance

Zusammenfassung

Schnee spielt eine wichtige Rolle in Prozessen, die Ökosysteme, das Klima und die menschliche Entwicklung beeinflussen. Insbesondere die Schneedecke in den Bergen ist für die Bevölkerung flussabwärts von großer Bedeutung. Eine Planung über den Umgang mit dieser dynamischen Ressource ist nur mit dem Wissen über die Verteilung und Eigenschaften der Schneedecke möglich. Schneemodelle, die zur Simulation von der Schneedecke in Bergen verwendet werden, variieren in ihrer physikalischen Komplexität, sind jedoch alle stark von genauen Input-Daten abhängig. Diese Daten müssen in der Lage sein atmosphärische Prozesse in Skalen aufzulösen, die für Schneemodelle häufig verwendet werden mit Auflösungen von 100 m oder höher. Prozesse wie die bevorzugte Ablagerung von Niederschlag, bei dem bodennahe Strömungsmerkmale und mikrophysikalische Prozesse den Niederschlag auf der Kammskala verstärken, müssen daher berücksichtigt werden. Eine der besten Methoden zur Bereitstellung von Input-Daten für Schneemodelle ist das dynamische Downscaling, bei dem meteorologische Input-Daten mit der Auflösung von Schneemodellen mithilfe numerischer Wettervorhersagemodelle berechnet werden. Diese Technik hat viele Vorteile gegenüber statistischem Downscaling, jedoch ist sie aufgrund des enormen Rechenaufwands für große Gebiete oder Zeitskalen oft nicht realisierbar. In dieser Dissertation stellen wir ein Modell mit mittlerer Komplexität vor, HICAR, das in der Lage ist, mit der Auflösung der meisten Schneemodelle zu laufen. Das HICAR-Modell verwendet Techniken aus dem Bereich des Schadstofftransports, um effizient ein 3D-Windfeld im Hektometer Maßstab zu lösen. Die Methode ermöglicht eine direkte Modifikation des Windfelds und erlaubt Parametrisierungen von stationären Wirbelstrukturen und thermisch getriebenen Hangwinden. Diese Verbesserungen des Strömungsfelds, in Kombination mit Verbesserungen der Physik des Modells, führen zu einer akkuraten Simulation bodennaher atmosphärischer Variablen. Die 2m Lufttemperatur, Strahlungseingänge und der Niederschlag des Modells werden mit Beobachtungen von automatischen Wetterstationen und gerasterten Niederschlagsprodukten verglichen. Eine prozessorientierte Betrachtung des Niederschlags mit einer Auflösung von 50 m wird unter Verwendung eines hochmodernen Mikrophysik-Schemas vorgestellt. Die Ergebnisse dieser Bewertung zeigen die Fähigkeit von HICAR, die bevorzugte Ablagerung von Schnee zu simulieren, während außerdem das Prozessverständnis durch die Interaktion bodennaher Strömungsmerkmale mit mikrophysikalischen Prozessen erweitert wird. Schließlich wird die Relevanz

Zusammenfassung

des Modells für die Schneemodellierung gezeigt. HICAR wird mit einem Schneemodell mittlerer Komplexität, FSM2trans, gekoppelt. Das gekoppelte Modell, HICARsnow, ist in der Lage, Muster von Schneeakkumulation und -ablation während der Schneesaison zu simulieren. Die Fähigkeit von HICAR, die bevorzugte Ablagerung von Schnee zu simulieren, verbessert die Verteilung der Schneehöhe in komplexem Gelände im Vergleich zu Schneemodellläufen mit statistischem Downscaling. Diese Dissertation zeigt, dass eine atmosphärische Modellierung mittlerer Komplexität im Hektometer Maßstab möglich ist, dass sie in der Lage ist, atmosphärische Variablen relevant für Oberflächenmodelle aufzulösen, und dass sich dies in eine bessere Darstellung von Prozessen in Schneemodellen übersetzen lässt.

Stichwörter: Atmosphärische Modellierung, Schnee-Atmosphären-Modellierung, Windfelder, Preferential Deposition, Auswertung, Modellierung mittlerer Komplexität, komplexes Gelände, Wind LiDAR Scans, Oberflächenenergie- und Massenbilanz

Contents

Acknowledgements	i
Abstract (English/Deutsch)	iii
List of figures	ix
List of tables	xi
1 Introduction	1
1.1 Background	1
1.1.1 Accumulation Processes	2
1.1.2 Ablation Processes	3
1.1.3 Snow Modeling	4
1.1.4 High-resolution NWP Modeling	7
1.1.5 Intermediate-Complexity Atmospheric Models	12
1.2 Objectives and Outline	15
2 The HICAR Model	17
2.1 Introduction	18
2.2 Model Development	19
2.2.1 Direct Adjustment of Wind Field	20
2.2.2 Mass-Conserving Wind Solver	24
2.2.3 Advection and Physics Parameterizations	29
2.2.4 Asynchronous I/O	29
2.3 Model Setup and Datasets	30
2.3.1 COSMO Model	30
2.3.2 WRF Model	30
2.3.3 ICAR/HICAR Setup	30
2.3.4 Spatio-temporal Domains	31
2.3.5 Gridded Datasets	32
2.4 Model Demonstrations	34
2.4.1 Wind Fields	34
2.4.2 Precipitation Distribution	36
2.4.3 Cold Air Pooling	39

Contents

2.4.4	Computational Efficiency	41
2.5	Conclusions	42
3	Intermediate Complexity Atmospheric Modeling: Is it Right?	45
3.1	Introduction	45
3.2	Methods	47
3.2.1	Observational Campaign	47
3.2.2	Model Changes	50
3.2.3	Modeling Setup	52
3.3	Model Evaluation	53
3.3.1	Point Comparisons	53
3.3.2	Ridge Crest Wind Patterns	57
3.3.3	Leeside Structures	58
3.3.4	Turbulent Flow Features	60
3.3.5	Thermal Flows	61
3.4	Conclusions	65
4	Seasonal Snow-Atmosphere Modeling: Let's do it	69
4.1	Introduction	70
4.2	Methods	72
4.2.1	Model Coupling	72
4.2.2	Parallelization of Snow Redistribution	73
4.2.3	Observational Datasets	74
4.2.4	Model Setup	75
4.3	Results and Discussion	76
4.3.1	Snow accumulation Processes	76
4.3.2	Ablation Processes	86
4.3.3	Snow-Atmosphere Interactions	88
4.4	Conclusions	92
5	Conclusions	95
6	Limitations and Outlook	99
	Bibliography	120
	Curriculum Vitae	121

List of Figures

1.1	Terrain as a function of model resolution	5
2.1	HICAR runtime schematic	20
2.2	Conceptual diagram of S_x + TPI corrections	25
2.3	ICAR v. HICAR vertical winds	26
2.4	Variational wind solver solutions for stable and unstable atmospheric conditions	28
2.5	Comparison of modeled surface flow fields: WRF, HICAR, ICAR	35
2.6	Leeside flow structures: ICAR, HICAR, WRF	37
2.7	50m resolution precipitation patterns: WRF, HICAR	38
2.8	Comparison of precipitation estimates over eastern switzerland	40
2.9	Evidence of cold air pooling	41
3.1	Map of the study domain	48
3.2	Schematic of Reynolds-Haugeneder-Elevation wind LiDAR scans	49
3.3	Comparison of HICAR with AWS observations – air temperature and winds	54
3.4	Comparison of HICAR with AWS – shortwave and longwave radiation	57
3.5	Comparison of HICAR Winds with Observations – ridge crests	59
3.6	Comparison of HICAR Winds with observations – leeside structures	60
3.7	Comparison of HICAR Winds with observations – turbulent structures	61
3.8	Modeled radiation, sensible heat fluxes, and air temperature from HICAR	62
3.9	Comparison of HICAR Winds with observations – thermally driven flows	64
3.10	Effect of HICAR thermal wind parameterization on surface flows	65
4.1	Overview of the upper Dischma domain	75
4.2	Peak accumulation snow depth maps: observed, HICARsnow, FSM2trans	78
4.3	Cross-ridge snow depth transect	79
4.4	Observed and modeled snow depth binned by aspect and elevation	80
4.5	Probability density functions of observed and modeled snow depth	81
4.6	Ridge-scale snowfall differences for two microphysics schemes	82
4.7	Process-level view of preferential deposition	83
4.8	Comparison of part of the Dischma domain at 50 m or 2 m resolution	85
4.9	Maps of observed and modeled snow difference between two dates	88
4.10	Improvement to 2m air temperature from coupling to FSM2trans	89
4.11	Impact of coupling HICAR to FSM2trans on near-surface air temperature	90

List of Figures

4.12 Effect of two-way model coupling on blowing snow sublimation 92



List of Tables

2.1	Model configurations	33
2.2	HICAR speed-up relative to WRF	42
3.1	Model configurations	53
3.2	RMSE and Mean Bias Error of HICAR and COSMO1 2 m air temperature	56

1 Introduction

1.1 Background

Mountains have been termed the "water towers of the world", with 50% of the earth's mountainous regions playing an essential or supportive role in the hydrology of downstream communities (Viviroli et al., 2007). This is due in part to mountain snowpack, with an estimated 17% of the world population relying on snow melt for their water supply (Barnett et al., 2005). This comparison of mountain snowpack with human infrastructure reflects the concept of "Ecosystem Services" (Costanza et al., 1997). Stated briefly, engineered structures built to replace these natural water towers would be costly, and likely garish. While water towers require the use of pumps to store water, the processes which form and distribute mountain snowpack are entirely free of charge. Solar heating of the earth's surface evaporates water, converting it into a vapor which can then rise thousands of meters into the atmosphere. This water then travels great distances until it encounters atmospheric conditions facilitating its condensation and, eventually, precipitation. The volume of water involved in precipitation events can be staggering, with some types of precipitation events earning the name "Atmospheric Rivers", because they can transport more water than flows out of the Amazon river (Zhu & Newell, 1998). When this water falls as snow, its entrance into the local hydrological system is delayed. Instead, months of precipitation, in some locations up to 50% of the annual precipitation (Sturm et al., 2017), become locked away until the spring. This allows ecosystems to benefit from a steady supply of water even months later during warm, dry summer months. When the release of water is steady, it has benefits for hydroelectric energy production, fish populations, and downstream communities. When the release of water is sudden, it can lead to catastrophic springtime flooding as weeks of stored precipitation enter the water cycle in a matter of days (Henn et al., 2020). Forecasting of the releases from this natural reservoir are thus crucial to allow downstream communities to plan with the natural variability in seasonal snowpack. And understanding snow melt begins with understanding the processes acting on the snowpack. These can be broadly grouped into accumulation processes, which determine the spatial distribution of the snowpack at the end of the winter, and ablation processes, which determine the timing and magnitude of snow melt.

1.1.1 Accumulation Processes

The accumulation of snow on the ground is determined first by snowfall processes, and later by redistribution processes which shape this initial distribution.

Snowfall Processes

Snowfall over complex terrain is influenced by processes occurring at a variety of scales. Starting at the largest, orographic precipitation occurs when an air mass is forced to rise over terrain. As a parcel of air ascends higher into the atmosphere, it finds itself under less pressure from the kilometers of air above it. This reduced pressure allows the parcel to expand into equilibrium with the relatively low pressure air at this elevation. As the air expands, it cools adiabatically until condensation. This cooling reduces the amount of water vapor that an air parcel can hold. If the cooling is strong enough, the parcel can no longer hold all of its water, the excess condenses as cloud water. This is a simplified view of the process, with what follows in cloud microphysics to be more complex still. Suffice to say, the lifting of air over mountains generates precipitation patterns over scale lengths of the obstacle itself (Mott et al., 2018).

Moving down to finer resolutions, interactions between local terrain maxima (ridges, peaks) and the flow field lead to a similar process of cloud formation. These near-surface clouds may result in precipitation on their own, leading to elevation-gradients in snowfall, or they may act as a feeder cloud (Bergeron, 1965). Feeder clouds exist as part of the seeder-feeder mechanism, where some precipitating cloud aloft "seeds" clouds below with hydrometeors. As hydrometeors pass through feeder clouds below, the saturated atmosphere leads to riming or vapor growth of the hydrometeors, increasing the transport of mass to the surface and improving precipitation efficiency (Houze & Medina, 2005).

Lastly, preferential deposition acts at the scale of individual slopes to alter snowfall patterns (Lehning et al., 2008). Preferential deposition was originally introduced to describe the alteration of hydrometeor fall speeds by near-surface vertical winds, but has expanded to include interactions between the mean flow aloft and microphysical processes. In this process, the peak in precipitation from a seeder-feeder cloud may be shifted downwind by the flow (Mott et al., 2014; Zängl, 2008). Preferential deposition has been observed both in maps of snow depth (Lehning et al., 2008), radar observations of precipitation (Mott et al., 2014), and numerical studies of the process (Comola et al., 2019; Z. Wang & Huang, 2017). A more comprehensive review of the literature around preferential deposition is provided in section 4.1.

All of the processes described here are germane to the formation of snowfall in winter over complex terrain, and do not address all of the processes affecting precipitation patterns in mountains.

Redistribution Processes

Redistribution processes act on the pattern of snow set up by snowfall events. They include wind-driven redistribution and gravitational redistribution. Wind-driven redistribution can be separated further into three processes: creep, saltation, and suspension. Creep occurs when individual grains of snow are rolled along the surface by wind. This process contributes little to the total transport of mass via wind-redistribution. Saltation involves the ejection of snow particles from the surface by wind (Doorschot & Lehning, 2002). Once ejected, the particles are blown downwind by the near-surface flow, smashing into the snow surface typically under a meter away. This impact can eject further snow particles, and the process repeats itself, resulting in a net transport of snow (Melo et al., 2023). And, lastly, transport via suspension occurs when snow in the saltation layer is ejected high enough to become entrained in the turbulent surface layer. Once here, snow particles can travel large distances in this cloud of suspended snow. The transport of snow depends both on the surface conditions of the snowpack, and on the wind speeds present (Filhol & Sturm, 2015; Gallée et al., 2001). Surface crusts caused by rain or sun increase the threshold friction velocity needed to result in ejection of snow particles from the snowpack. Wind transport itself also results in firmer snow surfaces, where the fragmentation of wind-transported snow results in finer particles which pack together more easily (Comola et al., 2017; Sommer et al., 2017). Once wind speeds exceed this threshold friction velocity, transport initiates, with a non-linear relationship between wind speeds and transport rates (Melo et al., 2022; Sturm & Stuefer, 2013). While transport via suspension can have the highest rate of transport, for small-scale terrain features and obstacles in flat terrain where wind speeds are lower, saltation can comprise most of the wind-redistribution over a season (Gossart et al., 2017; Wever et al., 2023). During wind-redistribution, snow may also sublime in the presence of dry air, which can result in saltation or suspension becoming a net ablative process (G. Liston & Sturm, 2004).

Gravitational redistribution is perhaps best known as avalanching, where large sections of the snowpack detach and rumble down slope in a single event (Sovilla et al., 2006). Other forms of gravitational redistribution include sloughing, where excess snow on steep terrain features is shed (Bernhardt & Schulz, 2010; Sommer et al., 2015), and cornice fall, where hardened, wind-transported snow which juts out from ridges breaks off and falls down slope.

1.1.2 Ablation Processes

Ablation processes are those which remove snow from the snowpack. This can occur through direct removal of mass, either via sublimation, or via wind scour and avalanching. Because wind scour and avalanching simply move snow elsewhere, we define these as redistribution processes above. Sublimation, however, removes mass directly from the snowpack. Ablation can also occur through melt. Thus, most ablation processes are those with add energy to the snowpack. This means positive alterations to the energy balance equation of the snowpack:

$$\frac{dH}{dt} = SW_{in}(1 - \alpha) + LW_{in} + LW_{out} + Q_{SH} + Q_{LH} + Q_p + G \quad (1.1)$$

Here, $\frac{dH}{dt}$ represents changes to the snowpack enthalpy through time. This is related to various fluxes, where LW_{in} and LW_{out} represent incoming and outgoing longwave, respectively, Q_{SH} is fluxes from turbulent sensible heat exchange, Q_{LH} is fluxes from turbulent latent heat exchange, Q_p is heat advected with precipitation, and G is the ground heat flux. Lastly, $SW_{in}(1 - \alpha)$ is the net shortwave radiation absorbed by the snow. It is expressed more explicitly here than the other terms to highlight the strong dependency of this term on α , the snow pack albedo.

1.1.3 Snow Modeling

In the past decade, direct observation of the mountain snowpack has been made possible through the use of airborne Light Detection And Ranging (LiDAR) technology (Deems et al., 2013; Painter et al., 2016). Terrestrial LiDAR scanning of the snowpack is also possible, offering much more temporal flexibility at the cost of reduced spatial extent (Grünwald et al., 2010; Mott et al., 2010a, 2011; Sommer et al., 2015; Voordendag, Goger, Klug, et al., 2023). This technology has a high spatial resolution capable of mapping the mountain snowpack at the basin scale with a horizontal resolution below 10 m. However, the technology is limited in its temporal resolution, let alone the significant cost of each flight or sensor. For these reasons, direct observation of mountain snowpack remains impractical for forecasting purposes, and estimates of the snowpack state are required. Numerical simulations, where the state of the snowpack is simulated using physical equations and computers, is promising for locations where comprehensive snowpack mapping is either unfeasible due to cost or extent, or for periods between comprehensive surveys. Additionally, some numerical models allow for snowpack properties such as the internal energy content, density, and structure of the snowpack to be estimated, whereas LiDAR-based observations only observe snow depth.

The simplest form of snow models are temperature-index models, which estimate snow melt rates from air temperature. This simplistic formulation finds success despite the greater physical importance of radiation due to the influence of radiation on ambient air temperature (Ohmura, 2001). Temperature-index models are often employed in glacier or hydrologic models where the precise timing of melt and a spatially distributed model structure are of lesser importance. However, temperature-index models are generally inaccurate over short time periods, or in resolving complex melt patterns arising from an interaction of topography and radiation (Hock, 2003). Bulk snowpack models exist one step up the ladder of complexity, where the energy balance (EB) of the snowpack is solved for. Still, the entirety of the snowpack and its properties are represented with bulk values (Ek et al., 2003). A further improvement are multi-layer snowpack models, which consider an arbitrary number of layers in the snowpack, allowing for a finer representation of heterogeneous snowpack properties (Anderson, 1976;

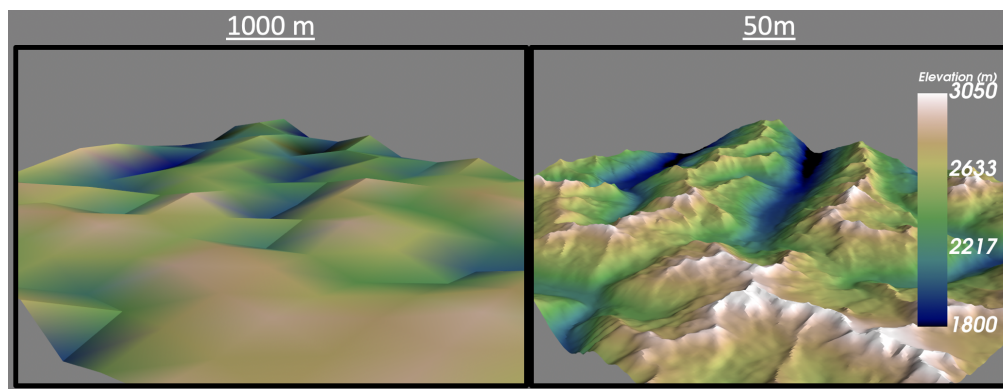


Figure 1.1: Comparison of the Upper Dischma Catchment outside of Davos, represented using either 50 m topography (right side) or 1000 m topography (left side).

Essery, 2015). And, lastly, there are microphysical snowpack models (Lehning et al., 2006a; Vionnet et al., 2012). Similar to multi-layer EB snow models, these models solve for the total snowpack energy balance and resolve the stratigraphy of the snowpack. Additionally, these models consider more physical processes affecting the snowpack than multi-layer EB models, including heat flow through the snowpack, the evolution of the snowpack microstructure, and snow settling based on the microstructure.

From a hydrologic perspective, the goal for any one of these snow model varieties is to determine how much snow is melting and when it is melting. Of course, the melt that occurs in spring is dependent on the amount of and the distribution of snow in a catchment. Luce et al., 1998 found that representing drifting snow, which contributes to the pattern of snow at peak SWE, was as important for modeling runoff from a sparsely vegetated, continental basin as representing spatial variation in radiation input. This finding supports the broader argument that capturing the distribution of snow around peak accumulation is as important for modeling snow melt as capturing the spatial variation in melt rates (Egli et al., 2012).

Other studies have identified a scale break in the spatial auto-correlation of snow depth around 20-40 m, implying that statistically significant heterogeneities in snowpack begin at these scales Deems et al., 2006; Mott et al., 2011. The authors of these studies note that this scale break varies according to the dominant processes at a site, and the heterogeneity of the topography. Figure 1.1 shows what model topography looks like at a 1000 m vs 50 m resolution. Clearly, the representation of processes such as terrain shading or blowing snow on such a smoothed grid will be different than what is possible on the higher resolution grid (Magnusson et al., 2019). All of which is to say that in order to simulate releases of water from snow dominated catchments, the processes affecting the snowpack at the hectometer scale (section 1.1.1) must be accounted for.

To quantify many of the processes introduced in section 1.1.1, snow models rely on meteorological forcing data. This data is provided as input to the models, which they use to update their internal state through time. Across the range of snow model complexities, uncertainty

in input data has been identified as a significant source of error in snow models (Magnusson et al., 2015; Schlögl et al., 2016; Voordendag et al., 2021). An accurate estimation of snow albedo is rendered inadequate if input shortwave radiation has a significant bias. Precipitation is singled out in particular, with Raleigh et al., 2015 and Magnusson et al., 2015 showing that typical biases in precipitation amounts contribute as much to model uncertainty at peak accumulation as variation in model process representation. Snow models themselves do not represent the various snowfall processes, and thus require input data to account for these processes. Unfortunately, observations of precipitation in mountainous terrain at the spatial scales needed for snow modeling have proved intractable (Germann et al., 2022). A recent analysis of various precipitation products in complex terrain has also suggested that model output now rivals observational capabilities in these areas (J. Lundquist et al., 2019). In lieu of accurate, specialized observations of meteorological forcing data, various techniques have been developed to generate such data. These techniques are collectively termed "downscaling".

Statistical Downscaling

Before downscaling, data used for force distributed snow models often comes in two forms: gridded data from numerical weather prediction (NWP) models (section 1.1.4) or point data from observations. Point data exists as observations from sensors deployed in the environment to measure meteorological variables relevant to snow modeling. These point data must then be distributed in space, such that each grid point of a distributed snow simulation receives some value. Statistical downscaling can have the most success for variables which vary broadly as a function of elevation, such as air temperature, pressure, or precipitation. In these cases, lapse-rates can be used as a first-order approximation, and are still often employed in snow hydrological modeling (Mott et al., 2023; Pomeroy et al., 2022). If a sensor network is dense enough, these forms of point-data interpolation can be successful, but scenarios such as cold-air-pooling in valleys or preferential deposition at the slope scale pose difficulties for point-data interpolation. Sensor networks also often have poor coverage of higher elevation areas of a domain, where terrain is steeper and atmospheric conditions are harsher (Frei, 2014; Matthews et al., 2020). This leads to a lack of information at high-elevation areas, and extrapolation to these elevations, with corresponding assumptions, is needed (Mott et al., 2023). The second form of statistical downscaling involves using gridded output from NWP models. These data are already somewhat distributed, but need to be further refined to the snow model grid. Gridded NWP output is rarely at the same resolution of distributed snow models for reasons discussed later in section 1.1.4. Using gridded NWP model output may offer a denser set of initial data to downscale from, but may include intrinsic errors since it is model output, and not observations. Some of the most successful statistical downscaling approaches combine both point observations and distributed output from NWP models (Magnusson et al., 2014). Some variables such as temperature or humidity are also better suited for statistical downscaling than others. This is related to the spatial variability and importance of each variable. For example, air temperature is generally more spatially homogeneous than wind speed near ridge crests, and a 10% bias in humidity has a more mild impact on spring snow

melt than a 10% bias in shortwave radiation. In particular for wind speeds, there is a growing consensus in the literature that statistic downscaling methods are insufficient for modeling snow-transport via wind (Marsh et al., 2020; Musselman et al., 2015; D. S. Reynolds et al., 2021). To improve the accuracy of downscaled forcing data, a second downscaling technique, dynamic downscaling, can be employed.

Dynamic Downscaling

Dynamic downscaling relies on the use of physical models to produce estimates of meteorological forcing data. This often takes the form of running numerical weather prediction (NWP) models at the desired resolution of the forcing data. Dynamic downscaling is often used in the climate modeling community, and in this way refers to the use of regional climate models (RCMs) to downscale GCMs (Giorgi & Gutowski, 2015). Dynamic downscaling in general refers to resolving meteorological variables for a target fine-resolution grid in a physically consistent manner, ensuring that inter-variable dependencies are accounted for (Boé et al., 2007; Kruyt et al., 2022). Hence, changes to the wind field resulting from higher resolution topography lead to corresponding changes to the precipitation field. The clouds which produce this precipitation will block incoming shortwave radiation at the surface, changing the surface temperature field in the process. These complex interactions are difficult to account for with statistical downscaling alone. One demonstrative example of this is precipitation phase partitioning. Most snow models partition precipitation into either solid or liquid precipitation based on surface temperature measurements (Harder & Pomeroy, 2014). During surface inversions, surface temperatures may indicate solid precipitation, while liquid precipitation falling aloft does not freeze when passing through a shallow surface inversion. Such a situation is avoided with dynamic downscaling, which should resolve the relevant microphysics that result in liquid precipitation at the surface. Some phase-partitioning methods have been developed which mix the statistic and dynamic downscaling, using more information about the 3D atmosphere to downscaling precipitation than surface temperature alone (Vionnet et al., 2022). While attractive, dynamic downscaling has remained limited in its application. To better understand why dynamic downscaling may succeed in supplying more accurate forcing data and why it has been limited in its use as of yet, we explore high-resolution NWP models in the next section.

1.1.4 High-resolution NWP Modeling

Dynamic downscaling is just one usage of powerful, modern NWP models. To better understand the potential and limitations of dynamic downscaling for snow models, an overview of NWP models is warranted. Broadly speaking, NWP models consist of two parts: dynamics and physics.

Dynamics

Dynamics are here defined as processes relating to the solution for a 3D pressure field, the resultant solution of a 3D wind field, and an advection scheme that calculates the transport of certain quantities. The motions of the atmosphere are considered by invoking Newton's second law and considering how a fluid parcel reacts to forces upon it. This treatment leads to the familiar Navier-Stokes equations, which are solved to calculate the temporal derivative of each component of the three-dimensional wind vector. The Navier-Stokes equations are expressed in their incompressible form as:

$$\frac{\delta \mathbf{u}}{\delta t} + (\mathbf{u} \cdot \nabla) \mathbf{u} = -\frac{1}{\rho} \nabla p + \nu \nabla^2 \mathbf{u} + \mathbf{F} \quad (1.2)$$

In this equation, **bolded** terms represent three-dimensional vectors. \mathbf{u} is the wind vector, t is the model time, ρ is the density of air, p is the pressure field, ν is the kinematic viscosity, and \mathbf{F} are any external forces acting on the fluid, such as gravity or Coriolis forces. The first term represents the rate of change of each component of the wind vector, the second term represents the flux through a grid cell, the third term shows forces introduced by pressure gradients in the fluid, the fourth term represents internal frictional forces in the fluid, and the fifth term accounts for external forces acting on the fluid. This equation is then solved by using either a Reynolds Averaged Navier-Stokes (RANS) form of the equation or using a Large Eddy Simulation (LES). RANS solvers work by taking a time-average of the wind vectors, decomposing each component into a mean component and a fluctuating component which averages to 0 over the chosen time interval. This allows for the Navier-Stokes equations to be solved stably on larger grid resolutions and resolves steady structures in the flow. LES solvers perform a similar averaging, this time in space, allowing for a consideration of sub-grid scale turbulence. Both types of solutions to the Navier-Stokes equations are used throughout fields concerned with environmental flows. The necessary iterative solution to the Navier-Stokes equations is computationally intensive and contributes a significant portion to the overall run time of NWP models.

For the sake of this thesis, we will briefly focus on the pressure gradient expressed in this equation. The Navier-Stokes equation is solved to obtain a temporal derivative, which is used to update each velocity component. In this way, the Navier-Stokes equations give a numerical approximation through time for the continuous function of wind velocities. To ensure stability of this integration through time, the time step is limited to make the change to the velocity field at each time step small. As the horizontal resolution of a model grid increases, steeper topographic features may be better represented. This means that, for terrain-following grids, two lateral faces of a grid cell will occupy different elevations over a relatively short distance. Assuming that vertical pressure variations are larger than horizontal pressure variations in the atmosphere, this result implies larger horizontal pressure gradients on the computational grid when higher horizontal resolutions are used. But, we just noted that the integration

time step is limited by the magnitude of the pressure gradient. This results in a modeling choice: does one use the true topography and accept smaller integration time steps to allow for convergence, or does one smooth the topography to allow for larger integration time steps. This dependency of the model time step on resolution will be further expanded upon in the later sub-section "NWP Model Run Times".

Physics Parameterizations

The second main part of NWP models, physics parameterizations, represent processes occurring in the atmosphere, as well as the land surface. These physical parameterizations are sorted according to which processes they seek to represent, trading variables to facilitate interactions between, say, radiative energy input and a thermal response from the land surface. Four parameterizations of relevance to this thesis are the radiation, microphysics, planetary boundary layer (PBL), and land surface model (LSM) schemes. The prior schemes are listed in order of average computational demand, with some variation to be expected between parameterizations of different complexity.

Microphysics Schemes

Microphysics schemes parameterize interactions involving water species in the atmosphere which lead to precipitation. Simulations examining precipitation patterns in complex terrain thus depend heavily on the accuracy of the microphysics scheme used. For atmospheric modeling with the WRF model in the Rocky Mountains and the Alps, Liu et al., 2011 and Gerber et al., 2018 have noted that the Morrison microphysics scheme (Morrison et al., 2005) performs better than other popular microphysics schemes when predicting winter snowfall. The Morrison microphysics scheme belongs to a class of microphysics schemes referred to as two-moment schemes. This means that for certain types of condensed water, or hydrometeors, the microphysics scheme tracks two physical properties, or moments. For example, cloud water is represented by a single value in the Morrison scheme, namely how much mass for a given model grid volume is comprised of cloud water. For snow particles, however, the Morrison microphysics scheme tracks the number of particles per grid volume, in addition to the amount of mass. This two-moment approach allows for hydrometeors and their properties to be considered in more detail. Is there a large mass of snow distributed among many particles, or concentrated into relatively fewer particles? One can imagine that snow particles in the former case should have lower densities, and thus slower fall speeds, than the later case. Two-moment schemes then use this information to diagnose additional particle properties given an assumed relationship between number concentration and mass concentration.

Modeling studies using two-moment microphysics schemes at the hectometer resolution or finer have found that such schemes simulate ridge-scale differences in precipitation patterns. Vionnet et al., 2017 showed that microphysical processes affect snowfall patterns at a 50 m resolution, finding that riming of snowflakes caused by updrafts resulted in enhanced down-

Chapter 1. Introduction

wind precipitation. Gerber et al., 2019 reached similar conclusions, namely that microphysical processes could contribute up to two-thirds of the larger process of preferential deposition. The findings of these modeling studies are in agreement with observations of precipitation patterns in complex terrain (Lehning et al., 2008; Mott et al., 2014).

While an improvement over single-moment schemes, the assumed mass-diameter relationships of two-moment schemes do not fully represent how the properties of frozen hydrometers change. As an example of this, we can consider the shape of frozen hydrometeors, sometimes referred to as "habit". As ice particles change their shape habit, important properties such as riming efficiency or fall speed will also change. Microphysics schemes that do not account for a spectrum of particle shapes must discretize the distribution into sorted ice particle classes. These classes then use fixed parameters to determine particle density or fall speed, resulting in large sensitivity to which parameter values are chosen (McFarquhar et al., 2006). Thus, adaptive habit (AHAB) microphysics schemes have been introduced, which effectively add additional moments for frozen hydrometeor types, allowing for changes to particle shape to be considered. These schemes improve the representation of particle fall speed and mass evolution relative to two-moment schemes (Jensen et al., 2017; Morrison & Milbrandt, 2015). Studies of high-resolution precipitation patterns have as of yet not employed AHAB schemes in their study of solid precipitation, leaving open the question of whether the added process representation of AHAB schemes warrants their complexity at high resolutions.

Land Surface Models

LSMs compute the state of the land surface and any surface-atmosphere exchanges. This is where the representation of snow in NWP models is handled. When NWP models are used for estimating changes to global temperatures under climate change, the representation of snow plays a crucial role. Incoming shortwave radiation heats the earth's surface, and this energy is then remitted in the longwave spectrum. Longwave radiation is what ultimately becomes "trapped" by greenhouse gases, contributing to a warming trend. Thus, the absorption of radiative energy by the land surface contributes directly to the signal of rising global temperatures. The land surface albedo determines how much of the incoming shortwave radiation is absorbed, and how much is reflected back to the atmosphere as shortwave radiation (Eq. 1.1). Typical natural land surface types have albedos ranging from 0.08 for some coniferous forests, to 0.4 for sand. Fresh snow, with an albedo around 0.8, has one of the highest albedos for naturally occurring land covers in the earth system. This means that simulating the presence and properties of snow is of crucial importance for climate change studies.

A snow model intercomparison project designed to identify shortcomings in snow models implemented in General Circulation Models (GCMs) was performed by Krinner et al., 2018. One of the most distinct conclusions from this and prior intercomparison studies was to use multi-layer EB snow models instead of single-layer bulk models in GCMs. As a result, most operational weather models and climate models have recently adopted multi-layer EB snow models (Arduini et al., 2019; Sharma et al., 2023). However, the range of parameterizations

and parameter values present in these intermediate complexity snow models still leads to significant scatter between them, particularly in warmer snow climates or during spring melt (Essery et al., 2009; Nijssen et al., 2003). What's more, most of these evaluations have occurred at stations where adequate, high-quality forcing data is present (Ménard et al., 2019). This is critical for evaluating snow models, but using point-scale simulations means that re-distribution processes cannot be validated. This point is of lesser interest to GCMs though, which cannot run at the spatial resolutions where redistribution affects snow distribution. So, while these developments in coupling intermediate complexity snow models to GCMs have improved forecasts (Arduini et al., 2019), these models remain incapable of simulating blowing or drifting snow. For that, more involved coupling strategies are required.

Coupled Snow-Atmosphere Models

In an attempt to represent snow redistribution processes in existing NWP models, snow models developed for use in the world of snow physics/snow hydrology have been coupled to atmospheric models. In this way, we define coupled snow-atmosphere models to be the coupling of an atmospheric model with a snow model of an at least intermediate complexity, where a multi-layer snowpack and snow redistribution are represented. Such approaches have coupled NWP models with snow-physics models, the most complex form of snow models (Sharma et al., 2023; Vionnet et al., 2014). Other approaches have sought to augment existing snow models in NWPs with better process representations (Saigger et al., 2023; Xie et al., 2019). Studies using these coupled snow-atmosphere models at horizontal resolutions relevant for snow hydrology (i.e. ≤ 100 m) have been conducted, focusing on the ability of such models to represent wind-blown snow and internal snowpack properties such as temperature and density (Sharma et al., 2023; Vionnet et al., 2014; Voordendag, Goger, Prinz, et al., 2023). These studies have demonstrated the potential of coupled snow-atmosphere models to represent blowing snow processes at the scale of single storms. This process representation, combined with the ability of NWP models to represent preferential deposition, have shown the ability of these models to generally simulate accumulation patterns in complex terrain. What lacks is a quantification of how much these processes contribute to snow depth patterns at the seasonal scale, and whether such approaches improve the representation of seasonal snow cover relative to statistical downscaling.

NWP Model Run times

The various studies on high-resolution snow-atmosphere models discussed above have demonstrated the utility of NWP models in predicting meteorological variables relevant to snow modeling at these scales. Importantly, no studies employing NWP models in complex terrain and at the basin scale, run at resolutions below 100 m, have been conducted for longer than 7 days. This constraint on spatial and temporal extent arises from the computational demand of such models. This section details some of the factors leading to this computational demand.

All NWP models include prognostic and diagnostic variables. Prognostic variables are solved for by taking an initial state and evolving them through time by calculating rates and integrating them through time. This integration is performed numerically, requiring some finite time step between the initial and final times. Diagnostic variables, by contrast, are diagnosed from information at the current time, and therefore require no numerical integration to solve for. The size of the time step determines how often a variable's state must be updated per unit of model time, and this calculation of the updated variable state is what requires significant computation. For example, a model time step of 6 seconds may mean calculating rates 600 times per model hour, while a time step of 60 seconds means calculating rates 60 times per model hour. Thus, the computational cost of a simulation is related to the size of a model time step.

Unfortunately, time steps cannot be chosen arbitrarily, and instead have an upper limit on their values. This upper limit is chosen such that the numerical integration technique chosen converges to a stable solution, and is often influenced by the model grid resolution. For example, if an explicit time-stepping integration method is chosen, the model time step is roughly linearly and inversely proportional to the model grid resolution. This means that increasing the grid resolution one order of magnitude results in an increase in time step of at least one order of magnitude.

The second consideration behind model run times is the increase in computational elements. Simulating the same domain at a 100 m horizontal resolution as a 1 km horizontal resolution involves a 100-fold increase in the number of model elements, since the number of elements in each of the lateral dimensions increases 10-fold. This ignores additional vertical grid refinements necessary to avoid large horizontal pressure derivatives along the model grid (K. A. Lundquist et al., 2012; Schär et al., 2002). So, increasing the horizontal resolution by one order of magnitude increases the number of computations to be performed by at least two orders of magnitude. Taken all together, decreases to the model physics time step and the nature of discretization cause an increase in computational time of at least three orders of magnitude for each order of magnitude decrease in horizontal resolution. This is one main reason why kilometer-scale operational weather forecasts are common, but dynamic downscaling at the hectometer scale is not.

1.1.5 Intermediate-Complexity Atmospheric Models

Atmospheric models also have some continuum of physical rigor and computational intensity, where certain modeling strategies are chosen based on the questions asked and the resources available. In some sense, this concept has been around as long as NWP models, with the first (GCMs) neglecting any topography in order to run on the high-performance computers (HPCs) of the 1950s (Phillips, 1956). Other approaches to describing the state of the atmosphere without incurring significant computational costs have sought analytic solutions to atmospheric variables. Instead of solving for atmospheric dynamics numerically, as in section

1.1.4, analytic solutions may exist for some states which reasonably approximate the true state of the flow. Linear mountain wave theory, introduced by Smith, 1979, is one of the most famous example of such analytic approaches. Linear mountain wave theory gives reasonable estimates of mountain waves forced by topography at the kilometer scale, provided that the atmosphere is in a steady state and that the Boussinesq approximation is valid. This reflects a common caveat of intermediate-complexity modeling: some assumptions are made which allow for processes to be neglected, resulting in idealized models. Traditional NWP models also make assumptions in their formulations, for example that LES models resolve all of the turbulence down to their resolutions. Still, the assumption of a state state atmosphere clearly limits the applications of some intermediate complexity approaches.

Smith and Barstad, 2004 expanded on the theory of Smith, 1979 further, including a simplistic microphysics scheme and a simple advection scheme to model orographic precipitation as caused by linear mountain waves. The concept of intermediate complexity atmospheric models was further expanded upon by E. Gutmann et al., 2016 with the Intermediate Complexity Atmospheric Research (ICAR) model. This model contains many similarities to the model introduced by Smith and Barstad, 2004. ICAR also uses linear mountain wave theory to predict perturbations to the horizontal components of velocity, but then combines this with a kinematic closure of divergence (O'Brien, 1970), allowing for a mass-conserving wind field. A first-order upwind advection scheme was employed for calculating the transport of prognostic variables. Lastly, in contrast to Smith and Barstad, 2004 who followed a similar setup, E. Gutmann et al., 2016 added the Thompson microphysics scheme (Thompson et al., 2016). After all of these considered reductions in model complexity, an atmospheric model with up to 800x speed up relative to the WRF model was obtained (E. Gutmann et al., 2016).

Horak et al., 2019 compared results from 4 km ICAR simulations over the south island of New Zealand to station measurements distributed through the mountain range. The authors found that ICAR improved precipitation estimates at the stations located in the mountain range relative to reanalysis data used to force the model. ICAR performance declined at coastal stations, however, reflecting the model's theoretical foundation in predicting orographic precipitation. Kruyt et al., 2022 also showed good agreement between ICAR and WRF precipitation fields at a 250 m resolution. However, in this study ICAR was forced with hydrometeors from the driving model (a non-hydrostatic NWP model) at the high-resolution boundaries. Such a setup makes it difficult to determine what patterns result from interactions of ICAR's dynamics and physics, and what is simply fallout of the forced hydrometeors.

The authors of Horak et al., 2019 returned to the model in a subsequent study, seeking to validate ICAR's representation of precipitation processes. Horak et al., 2021 found that estimates of precipitation across a ridge were sensitive to the height of the model's highest level, and to the type of boundary condition enforced there. Efforts were made to correct for this sensitivity to the upper boundary condition of ICAR by Horak et al., 2021, but it likely arose from large vertical winds at the model top typical of approaches using the kinematic closure of the continuity equation Goodin et al., 1980. Horak et al., 2021 also found that ICAR had

Chapter 1. Introduction

difficulties in capturing the trend in precipitation patterns across an isolated ridge at the 4 km resolution. For their setup, precipitation peaks occurred on either the windward or leeward side for the ICAR or WRF models respectively. Overall, Horak et al., 2021 predicted that their model changes in pursuit of improved process representation would likely degrade the results of Horak et al., 2019. In commenting on the earlier study, Horak et al., 2021 concluded that "the seemingly correct results were produced for the wrong reasons". Taken together, the ICAR model proposed an exciting paradigm for atmospheric models, but required more work to be reliable for precipitation estimates in complex terrain.

The paradigm put forward by E. Gutmann et al., 2016 contains two ideas worth capitalizing upon. The first is the inclusion of physics parameterizations identical to those used in traditional NWP models. The second is the reliance on conventional NWP output. If NWP models resolve dynamics at a particular resolution, then further perturbations to their 3D wind field at higher resolutions should in the least consider processes emerging in this scale gap. This perturbation approach may not conserve momentum, but later processing of the perturbed field can ensure mass consistency. Unfortunately, ICAR only included perturbations to the 3D wind field arising from linear mountain wave theory, which is not the dominant influence on the wind field at the hectometer scale in the presence of steep terrain. To move ICAR to hectometer resolutions, a better incorporation of terrain-induced modifications to the wind field was needed.

Variational Wind Solvers

To solve for wind fields at the hectometer resolution, diagnostic wind solvers may be employed. The concept of diagnostic, mass-conserving wind solvers has existed for decades (Sasaki, 1958), and has a colorful history in the literature. These solvers work by taking some initial 3D wind field and eliminating any divergence present in the wind field. This adjustment step happens under the constraint that adjustments to the original wind vectors should be minimized. The full problem results in an optimization problem, which is then solved using techniques from variational calculus, hence the name. Sherman, 1978 provided one of the first widely used implementations of this method, developing the MATHEW wind model. MATHEW obtained its initial wind field by interpolating between sparse measurements of the 3D wind field. After Sherman, 1978, various other studies sought to adjust the technique, adding considerations for atmospheric stability and terrain-following coordinates (Moussiopoulos et al., 1988; Ross et al., 1988). Evaluations of this technique against wind tunnel data and ridge-top meteorological stations have consistently shown its ability to simulate flow blocking and speed up over topographic features (Finardi et al., 1993; Forthofer et al., 2014; Ross & Fox, 1991; Wagenbrenner et al., 2016). In addition to being derived from point data, the initial field can also be obtained by interpolating from coarser resolution, distributed wind fields. In this way, divergence is introduced into the initial wind field by interpolating the coarse resolution wind field to the finer grid. Unresolved topographic features at the coarse resolution now appear at the finer resolution, introducing divergence at the lower boundary. The review of

Homicz, 2002 provides an excellent overview of the history of this technique.

Most of the implementations of the Sasaki, 1958 approach mentioned above were used in the field of air quality modeling. Forthofer et al., 2014 first applied the technique to the field of wildland fire management, developing the model WindNinja. The WindNinja model was then used in a number of snow modeling studies to generate surface wind fields for forcing blowing snow models (Marsh et al., 2020; Quéno et al., 2023; D. S. Reynolds et al., 2021; Vionnet et al., 2021).

These studies, particularly recent applications of the variational technique to snow modeling, motivate using this variational approach in an intermediate complexity atmospheric model. Some applications for snow modeling have used an approach of generating libraries of wind fields for different atmospheric situations, and then selecting fixed wind fields which match observed atmospheric conditions at a given time (Groot Zwaaftink et al., 2013a; Marsh et al., 2023; Raderschall et al., 2008; Vionnet et al., 2021). This approach has yielded successes but is less transferable to 3D dynamic downscaling due to the difficulty in categorizing the variety of 3D atmospheric states. Other approaches to calculating surface wind fields have developed parameterizations which approximate reduced wind speeds from flow-separation or leeside eddies (Winstral & Marks, 2002), or buoyancy driven flows (Oerlemans & Grisono, 2002; Prandtl, 1942). The relationship between static terrain descriptors, which can be calculated prior to model run time, and surface flow fields has also been shown (Dujardin & Lehning, 2022). These parameterizations may also be combined with the diagnostic wind solver discussed above, but the resultant effect on the 3D flow field remains unknown.

1.2 Objectives and Outline

The preceding overview of NWP models and other methods to generate input for snow models highlights their respective strengths and weaknesses. Long model run times have prohibited studies using coupled snow-atmosphere models at the hectometer scale from running over entire seasons. This ability would make dynamic downscaling feasible for forcing operational snow models, improving one of the largest sources of error in such models: input data. Recent research into intermediate complexity atmospheric modeling at the kilometer scale shows that such an approach can significantly reduce model run time without significantly degrading model performance. This begs the question of if such an approach could be extended to higher resolutions. Existing studies forcing snow models with diagnostic wind solvers based on variational calculus have shown promising results, but the ability of these solvers to replace the dynamic core of an NWP has not yet been demonstrated.

This thesis aims to address this opportunity through the following chapters:

- In Chapter 2, a novel intermediate complexity atmospheric model capable of resolving flow features at the 50 m scale is presented. This model extends the ICAR model intro-

duced in the previous chapter, addressing model structural issues that plagued earlier studies. The development of the model focuses on the implementation of a wind solver based on the variational calculus technique, as well as direct modifications to introduce eddy-like features into the flow. Additional changes to the model numerics are detailed, resulting in precipitation fields in complex terrain that are in agreement with existing distributed precipitation products.

- Chapter 3 presents an evaluation of the HICAR model presented in Chapter 2. This evaluation employs observations of temperature, wind, and incoming radiation to compare the HICAR model against the operational forecast over Switzerland. A Doppler wind LiDAR is also deployed, allowing us to compare HICAR's representation of flow structures in snow-covered, complex terrain to observations. Results from Chapter 3 motivate the improvement of the snow model used by HICAR, particularly to better simulate surface air temperatures.
- Chapter 4 responds to Chapter 3, coupling HICAR with the FSM2trans snow model. The resulting coupled model, referred to as HICARsnow, verifies the results of previous studies where HICAR was used to force FSM2trans. Precipitation patterns in complex terrain are examined at the slope scale, with a process-level validation of HICAR's ability to represent preferential deposition. Output from HICAR suggests that preferential deposition involves the interplay between near-surface flow features and microphysical processes. Modeled snow depth distributions are compared to LiDAR snow depth observations, evaluating how well HICARsnow can capture snow heterogeneity. The chapter also explores the effects on the atmosphere resulting from the refined representation of snow processes.

2 The High-resolution Intermediate Complexity Atmospheric Research (HICAR v1.1) Model Enables Fast Dynamic Downscaling to the Hectometer Scale

This chapter corresponds to the postprint version of the article published as:

Reynolds, D., Gutmann, E., Kruyt, B., Haugeneder, M., Jonas, T., Gerber, F., Lehning, M., and Mott, R.: The High-resolution Intermediate Complexity Atmospheric Research (HICAR v1.1) model enables fast dynamic downscaling to the hectometer scale, *Geosci. Model Dev.*, 16, 5049–5068, <https://doi.org/10.5194/gmd-16-5049-2023>, 2023.

Abstract High resolution (< 1km) atmospheric modeling is increasingly used to study precipitation distributions in complex terrain and cryosphere-atmospheric processes. While this approach has yielded insightful results, studies over annual time-scales or at the spatial extents of watersheds remain unrealistic due to the computational costs of running most atmospheric models. In this paper we introduce a High-resolution variant of the Intermediate Complexity Atmospheric Research (ICAR) model, HICAR. We detail the model development that enabled HICAR simulations at the hectometer scale, including changes to the advection scheme and the wind solver. The latter uses near surface terrain parameters which allow HICAR to simulate complex topographic flow features. These model improvements clearly influence precipitation distributions at the ridge scale (50m), suggesting that HICAR can approximate processes dependent on particle-flow interactions such as preferential deposition. A 250 m HICAR simulation over most of the Swiss Alps also shows monthly precipitation patterns similar to two different gridded precipitation products which assimilate available observations. Benchmarking runs show that HICAR uses 594x fewer computational resources than the WRF atmospheric model. This gain in efficiency makes dynamic downscaling accessible to ecohydrological research, where downscaled data is often required at hectometer resolution for whole basins at seasonal time scales. These results motivate further development of HICAR, including refinement of parameterizations used in the wind solver, and coupling of the model with an intermediate complexity snow model.

2.1 Introduction

Atmospheric models have seen remarkable improvements over the past decades, spurred on by their importance to society. Their usage within science ranges from climate and weather predictions to downscaling atmospheric variables as input to further geophysical models. Specific applications have included generating forcing data over sparsely instrumented domains (Khadka et al., 2022), downscaling global climate model output to study regional impacts (Spinoni et al., 2018), and coupling with land surface models to better simulate land-atmosphere feedbacks (Sharma et al., 2023). The concept intrinsic to all of these applications is one of scale. As model resolution increases, processes which were previously parameterized can be explicitly resolved, and the representation of the underlying terrain improves, allowing for more accurate dynamics (Chow et al., 2019; Prein et al., 2013; Wyngaard, 2004).

High-resolution (< 1km) simulations of winter storms in complex terrain have been used to augment our process-level understanding of particle-flow interactions such as preferential deposition (Gerber et al., 2018; Lehning et al., 2008; Mott et al., 2010b; Vionnet et al., 2017). Some of these simulations aimed at very high resolutions of 25 m and below and thus used stationary wind fields (Raderschall et al., 2008) or a decomposition of wind field into a limited number of dominating (stationary) patterns to enable simulations for the length of a storm (Mott et al., 2010b) to a full season (Groot Zwaafink et al., 2013b). Coupled glacier-atmosphere models have been developed and run at a range of spatial scales, demonstrating an ability to better simulate surface-atmosphere energy exchanges over glaciers (Collier et al., 2013; Goger et al., 2022). And, coupled snow-atmosphere models have been developed which explicitly resolve snow-atmosphere interactions (Sharma et al., 2023; Vionnet et al., 2014). These studies have all demonstrated the ability of high-resolution atmospheric modeling to improve estimates of precipitation, wind speeds, and surface-atmosphere interactions. However, all of them have focused on limited spatial and temporal extents due to the huge computational demand required of running modern atmospheric models at the hectometer resolution. In one study performing 50m simulations of winter precipitation using the WRF model, nearly 34,000 core hours were required to perform 1 day of simulation over a <100km² domain (Kruyt et al., 2022). Any practical application of high-resolution atmospheric modeling to questions concerning future climate scenarios or downscaling for land surface models is currently limited by the computational demand of atmospheric models.

This issue is no news to the community, and idealized atmospheric models of orographic precipitation and mountain waves have been developed and employed in the past (Smith, 1979; Smith & Barstad, 2004). Recently, the Intermediate Complexity Atmospheric Research (ICAR) model was introduced in E. Gutmann et al., 2016 (hereafter G16) to provide an alternative to highly idealized models and modern non-hydrostatic, compressible atmospheric models. In their 2016 paper, Gutmann et al., demonstrated excellent agreement between ICAR and WRF when simulating mountain waves and orographic precipitation over idealized terrain. Further demonstration over real, complex terrain at a 4km resolution gave good agreement on precipitation between the two models during the winter months. Most importantly, the ICAR

simulations used 143x fewer computational resources than the WRF model. The ability of ICAR to simulate orographic precipitation at the kilometer-scale has been replicated in other studies (Horak et al., 2019). ICAR has since occupied a niche in modeling studies where downscaling of long time series would otherwise be limited by computational resources. These results motivate the design philosophy behind ICAR that dramatic reductions in computational time may justify modest reductions in model accuracy for certain applications.

Such an approach is perfectly suited for high-resolution atmospheric modeling, where computational demands severely limit the experimental design of studies. However, the dynamics and physics of the base ICAR model, namely linear mountain wave theory and first-order upwind advection, are not suitable when modeling at the hectometer scale. Here we introduce a high-resolution variant of the ICAR model, HICAR, which adapts the ICAR model to be suitable at resolutions below the kilometer scale. In section 2.2 of the paper, key parts of HICAR's model development are detailed, with a focus on the model's wind solver, advection scheme, and input/output (I/O) operations. In the third section, information is given about other atmospheric models and gridded datasets used in this study, as well as details about model simulation setups. These models and datasets are then compared in section 2.4, where various demonstrations of the HICAR model provide a limited validation and are used to discuss the model performance. Lastly, a synthesis of the paper and a concluding discussion about the utility of the HICAR model is presented in section 2.5.

2.2 Model Development

In the original ICAR model, the 3-D wind field can either be generated through 3-D interpolation between the coarse resolution forcing data and the high-resolution grid, or it can be further modified using linear mountain wave theory (Smith, 1979). This modification alone simulates the disturbance of the meso-scale flow field caused by mountain ranges, namely the generation of mountain waves depending on the atmospheric stability. These effects are the dominant influence of the terrain on the meso-scale flow from scales of 10s of kilometers down to the kilometer scale, which is the scale range which ICAR was originally developed for. Increasingly, output from kilometer-scale compressible, non-hydrostatic atmospheric models run by regional weather forecasting offices are available (Benjamin et al., 2016; Seifert et al., 2008; Seity et al., 2011). These models are expected to capture the dynamics approximated by linear mountain wave theory. When using these models as forcing data for high-resolution simulations with ICAR, it would thus be redundant to run with the linear theory solution. Left with only an interpolated kilometer-scale wind field for a 3-D wind field, we found it necessary to implement a new wind solver capable of capturing dynamics induced by the underlying high-resolution terrain. These flow features should be necessary to simulate particle-flow interactions which lead to heterogeneous snowfall patterns. In addition to changes to the wind field, it was also necessary to modify the advection scheme of ICAR and the input/output (I/O) routines. ICAR only offers the first order upwind advection scheme, which has been shown to be highly diffusive, especially in complex terrain (Schär et al., 2002). When simulating

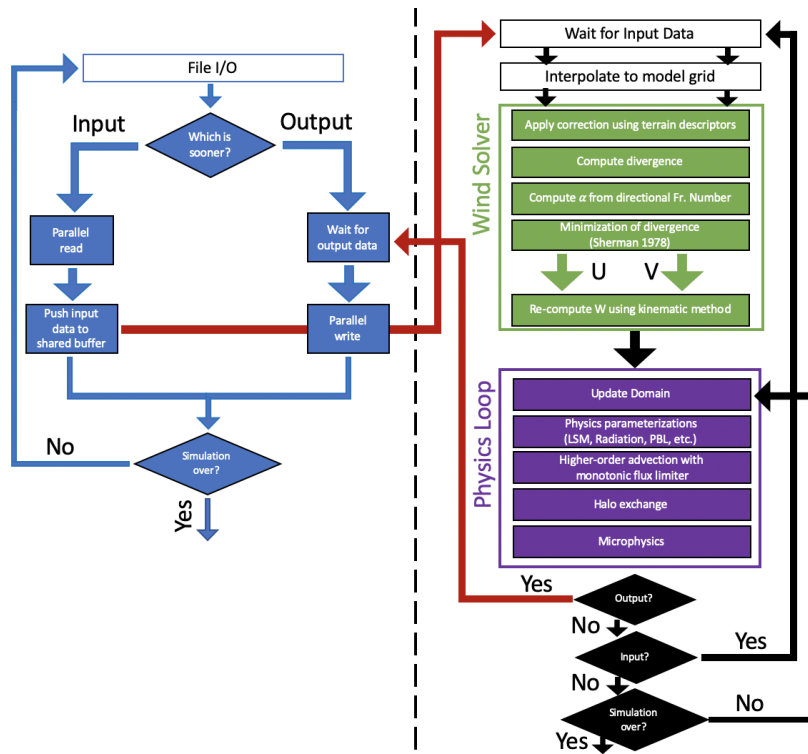


Figure 2.1: Schematic of major changes to HICAR’s runtime loop compared to figure 2.1 of G16. The left side of the figure features the I/O loop handled by I/O processes, while the right side features the runtime loop of HICAR, with a focus on the steps discussed in sections 2.2.2 and 2.2.3. Blue colors correspond to I/O processes, green to steps of the wind solver, purple to steps of the physics integration loop, and red to communication between I/O and compute processes. Within the wind solver and physics loop, downward arrows are implied between the steps where not indicated.

precipitation events, it is important that heterogeneities in moisture and temperature are maintained and do not become too smooth. Finally, as model resolution and speed increased, it became paramount to be able to efficiently read and write large volumes of data without significantly affecting run time. The following two subsections focus on new options for the wind solver in HICAR, while the last two focus on changes affecting the advection scheme and model input/output (I/O)(Figure 2.1).

2.2.1 Direct Adjustment of Wind Field

Taking a cue from existing statistical models of surface winds in complex terrain (Dujardin & Lehning, 2022; G. E. Liston & Elder, 2006b; Winstral & Marks, 2002; Winstral et al., 2017), we first develop corrections to the interpolated wind field near the surface based on the underlying terrain. This is done through terrain descriptors calculated at model initialization and then applied to the wind field at runtime. Terrain descriptors represent some qualitative information about the terrain quantitatively, such as if a particular location is sheltered from

a particular wind direction. Parameterizations can then be developed using these values, enabling non-local interactions between the topography and winds to be accounted for in a computationally efficient manner.

Terrain Descriptors

Topographic Position Index (TPI)

When downscaling winds from coarse to high resolutions, the representation of the model terrain can vary drastically. What appears as a small depression in the terrain at a 1km resolution may actually be a steep valley when viewed at a 100m resolution. To find areas in the high-resolution domain where large differences with the coarse Digital Elevation Model (DEM) may affect wind fields, we use the Topographic Position Index (TPI, Jenness 2006, Weiss 2001). TPI is calculated as the difference in elevation between a given terrain element, and the average terrain height within a given radius around that terrain element:

$$TPI = z_{hi} - \bar{z}_{radius} \quad (2.1)$$

Where z_{hi} is the high-resolution elevation and \bar{z}_{radius} is the mean elevation of the high-resolution grid within a given radius around z_{hi} . We set the search radius to be 4 km. The chosen search radius will depend upon the resolutions of the model and the forcing data being used. In general, larger search radii lead to wider bands of positive and negative TPI, while smaller radii select just the valley bottoms and tops of peaks, resulting in a more heterogeneous distribution of TPI (Weiss 2001). TPI has previously been used as a variable in other wind downscaling schemes (Winstral et al., 2017), serving to highlight areas where winds are expected to be higher, such as an exposed ridge. TPI was chosen as a terrain descriptor instead of locally differencing the model and forcing DEMs because it gives a description of exposure, which is a non-local concept. For example, a hill in a valley may have the same elevation on the high-resolution grid as on the smoother, coarse-resolution forcing grid, and the terrain difference would be 0. However, if this hill is in a valley, it is still relatively lower than the surrounding terrain, and this would result in a negative TPI.

3D Sx

The Sx parameter was first introduced by Marks et al., 2002, quantifying the maximum slope from a surface grid cell to a terrain element in the upwind direction. The Sx parameter was thus interpreted as a proxy for how sheltered a surface grid cell was from incoming winds, as the upwind terrain element was expected to disrupt the flow. Sx has since been used in many parameterizations of surface wind (Grünwald et al., 2013; Marks et al., 2002;

Winstral et al., 2013). Importantly, the S_x parameter gives directional information about terrain-wind interactions, which supplements the omni-directional TPI. Here we extend the original concept of Marks et al., 2002 into three dimensions, calculating S_x not just for the surface grid cells, but for all model grid cells in the vertical dimension. The motivation behind this is that the sheltering effects provided by an upwind terrain element will be felt above the surface as well as on the ground. The procedure for calculating 3D S_x is similar to that for 2D S_x : it is the maximum upwind slope between a grid cell (this time allowed to be above the surface) and the largest upwind terrain element. We add an important caveat that the largest upwind terrain element must also have a positive TPI value. This is done under the assumption that flow separation is more likely to occur for exposed terrain elements (positive TPI). The following equation:

$$S_{x_{A,d_{\max}}}(x, y, z) = \max \left(\tan^{-1} \left(\frac{DEM(x_v, y_v) - Z(x, y, z)}{\sqrt{(x_v - x)^2 + (y_v - y)^2}} \right) \right) \quad (2.2)$$

gives the S_x value for a given azimuth angle A , calculated at a specific point (x, y, z) , using a search radius of d_{\max} . DEM is the high-resolution DEM (2D) and Z is the grid cell height on the mass grid (3D). (x_v, y_v) give the location of the terrain element for which S_x is being calculated against. d_{\max} is a namelist variable which the user can define. A qualitative illustration of the 3D S_x parameter is given in Figure 2.2.

Application of Terrain Descriptors

The two terrain descriptors, TPI and S_x , seek to highlight areas of the domain where direct adjustment to the interpolated wind field are necessary. TPI indicates relative differences between the high-resolution terrain and a low-resolution representation, which is to say areas where the interpolated, high-resolution wind field are experiencing terrain features which the forcing terrain's lower resolution DEM may not resolve. Because TPI is non-directional, we only consider adjustments to the wind speed, and consider to increase wind speeds at areas of positive TPI (HICAR terrain higher than forcing terrain) and decrease them at areas of negative TPI. Testing showed that the wind solver discussed in section 2.2.2 adequately increases wind speeds over areas of positive TPI without a direct TPI-based adjustment, so only adjustments in areas of negative TPI are performed. This can be explained conceptually as reducing wind speeds in valleys deeper, and thus more removed from mesoscale wind speeds, than the forcing terrain suggests. This correction is only considered within the first 200m above the surface and is gradually decreased up to this height. This height limit was chosen empirically after testing multiple decay heights. Corrections based on TPI can thus be formulated as:

$$TPI_{cor} = \frac{TPI}{TPI_{max}} \frac{z_{top} - z}{z_{top}}, \quad TPI < 0 \quad (2.3)$$

where TPI is the surface TPI computed at each grid cell and z is the height of the grid cell in question. TPI_{max} is a scaling factor controlling the correction, and was set to 200 in our simulations. z_{top} controls the height at which the correction goes to 0, in this case 200m.

Corrections based on the Sx parameter are considered for all grid cells with a negative Sx value. For these cells, a threshold Sx angle, Sx_{thresh} , is calculated at the surface:

$$N = \sqrt{\frac{g}{\theta} \frac{d\theta}{dz}} \quad (2.4)$$

$$Ri = \frac{N^2}{\left(\frac{du}{dz}\right)^2 + \left(\frac{dv}{dz}\right)^2} \quad (2.5)$$

$$Sx_{thresh} = 180^\circ \min(\max(0, Ri), 0.25) \quad (2.6)$$

where N is the Brunt-Väisälä frequency, θ is potential temperature, and Ri is the Richardson Number. All vertical gradients are calculated over the first 100m above the surface. This is following the methodology of Menke et al., 2019 where the Richardson number used to classify stable and unstable conditions for leeside re-circulation was calculated over the first 100m above the surface. EQ #2.6 says that for Ri values greater than 0.25 [Stable], no sheltering effects occur, and for negative Ri values [Unstable], the threshold Sx angle is 0° . Although Sx_{thresh} is only calculated at the surface, it is used throughout the column to apply the following corrections in 3D. This threshold angle is then used to calculate an Sx correction factor

$$Sx_{corr} = \frac{Sx - Sx_{thresh}}{\phi_{def}} \quad (2.7)$$

Where Sx is the Sx angle for the given grid cell, Sx_{thresh} is the threshold angle calculated for that column, and ϕ_{def} , a scaling factor, is set to 30° . Sx_{corr} is then applied to the U and V wind vectors by divvying up the correction according to the slope of the underlying topography. This is shown conceptually in Figure 2.2, and follows the equation:

$$SLOPE = \sqrt{\left(\frac{dz}{dx}\right)^2 + \left(\frac{dz}{dy}\right)^2} \quad (2.8)$$

$$Sx_{u,cor} = -\frac{dz}{dx} \frac{Sx_{cor}}{SLOPE^2} \left(\frac{dz}{dx} U_m + \frac{dz}{dy} V_m \right) \quad (2.9)$$

$$Sx_{v,cor} = -\frac{dz}{dy} \frac{Sx_{cor}}{SLOPE^2} \left(\frac{dz}{dx} U_m + \frac{dz}{dy} V_m \right) \quad (2.10)$$

Where U_m and V_m are the U and V velocities staggered to the mass-grid, and $SLOPE$ is the terrain slope. Vertical gradients shown here are calculated over the grid cell. The net effect is to apply both a correction to the wind speed, and to rotate the wind vector about the slope-tangent. Finally, the two correction factors for TPI and Sx are applied as such:

$$U = U - Sx_{u,corr} \quad (2.11)$$

$$V = V - Sx_{v,corr} \quad (2.12)$$

$$U = U(1 + TPI_{cor}) \quad (2.13)$$

$$V = V(1 + TPI_{cor}) \quad (2.14)$$

We note that parameter values and correction formulations used in this section are somewhat arbitrary. The logic behind the corrections is explained above, and the exact values were reached through a sparse sampling of the parameter space. The goal of the current study is to demonstrate the potential of combining a pre-conditioning step, described in the current section, with the diagnostic wind solver described in the following section. The effects of this currently under-constrained approach to correcting the wind field is discussed further in Section 2.4.1, and these corrections will be further refined in a future study by using observations of the 3D wind field in complex terrain.

2.2.2 Mass-Conserving Wind Solver

After adjusting the wind field according to terrain descriptors, or after ingesting any arbitrary wind field from forcing data, the resultant wind field is not guaranteed to be divergence-free. Because ICAR is an incompressible atmospheric model, this would mean a violation of mass-conservation. Thus, some further correction to the 3D wind field must be applied to ensure mass-conservation. In the original ICAR model, this is ensured by calculating the divergence for each model layer and prescribing the grid-relative vertical velocity at the top of each layer such that divergence is eliminated. This is sometimes referred to as the "kinematic method" of balancing the winds (Homicz, 2002; O'brien, 1970). Unfortunately, this method is known to produce excessive vertical motion even for modest amounts of residual divergence (Goodin

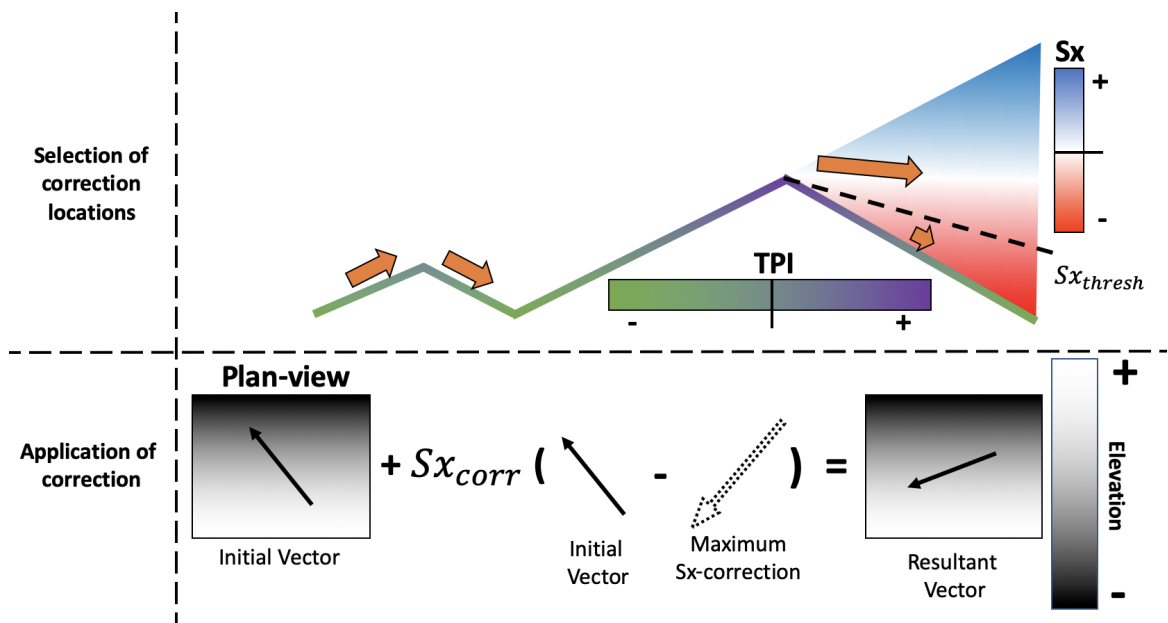


Figure 2.2: A conceptual outline of the Sx sheltering process. Areas where a correction should be applied are first selected, as indicated in the upper row. Only terrain elements with a positive TPI value are considered to be potential sheltering terrain elements. The smaller hill on the left has no positive TPI values along its slopes, so it does not produce an area of reduced wind speeds in the lee. The hill on the right does have a positive TPI value at its peak, so it is considered for sheltering. The Sx values in the leeside of the peak are examined and compared to the threshold Sx value, Sx_{thresh} , calculated in Eq. #2.6. Grid cells with Sx angles larger than this threshold angle experience a correction to their U and V wind speeds, as detailed in the second row of the figure. We consider that the maximum deflection of the leeside vector would be a rotation about the elevation gradient of the grid cell. This maximum correction is then applied to the initial vector with a correction factor, Sx_{corr} , as calculated in Eq. #2.7. The resultant vector is thus a mixture between the initial vector and the maximum possible correction.

et al., 1980). Figure 2.3 shows the strong vertical winds which are often observed in high-resolution simulations using the ICAR model with the kinematic method for balancing the 3D wind field. The strong vertical winds observed in the ICAR simulations are due to a) large grid distortions in complex terrain at high resolutions, b) the use of high-resolution forcing data from a compressible atmospheric model, and c) the kinematic solution for vertical wind itself (EQ #9 in G16). As the horizontal resolution is reduced, the magnitude and variations of the vertical motions are reduced. As a result, simulations with the ICAR model at coarser resolutions exhibit less strong vertical motion than shown here. However, such simulations still exhibit increasing vertical motion as a function of height due to the use of the kinematic solution for vertical velocity (O'Brien, 1970). This results in excessively strong vertical motion at the model top, and explains the sensitivity of ICAR to the height of the model top and choice of upper boundary condition reported in Horak et al., 2019 and Horak et al., 2021.

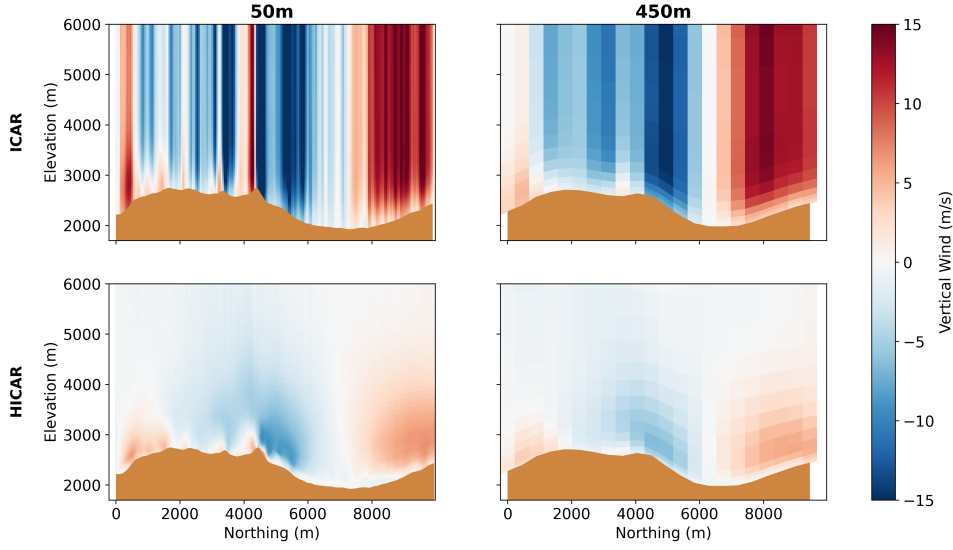


Figure 2.3: Comparison of vertical motion between ICAR and HICAR at 50m and 450m resolutions for an arbitrary simulation time step. ICAR is shown in the first row, HICAR in the second.

This issue alone motivates the implementation of a new approach to balancing the 3D wind field. When using the empirical adjustment of the 3D wind field described above, even more divergence is introduced to the wind field, resulting in entirely nonphysical vertical velocities. Clearly another technique for calculating vertical velocity is required for high-resolution applications.

HICAR employs a method for calculating a mass-conserving wind field which is based on a variational calculus technique. This technique has been developed over prior decades of wind modeling and pollutant transport (Ross & Fox, 1991; Sasaki, 1958; Sherman, 1978), and has been adapted into a variety of wind models (Forthofer et al., 2014; Moussiopoulos et al., 1988). Wind Tunnel experiments and field observations have routinely demonstrated this techniques ability to simulate speed up and deflection of flow around obstacles (Forthofer et al., 2014; Ross & Fox, 1991; Wagenbrenner et al., 2016). The method works by solving an optimization problem where two functions are reduced: the divergence of the wind field and the total deviations of the solution wind field from the initial wind field.

$$Div = \frac{d\rho u}{dx} + \frac{d\rho v}{dy} + \frac{d\rho w}{dz} \quad (2.15)$$

$$Diff = (u_i - u)^2 + (v_i - v)^2 + \alpha(w_i - w)^2 \quad (2.16)$$

Where u and v refer to the east- and north-ward wind speeds, w refers to the vertical wind

speed, and \dot{w} refers to the contravariant, grid-relative wind speed. All of the x_i variables indicate initial values. The distinction between w and \dot{w} is necessary when the optimization is performed on a grid with a vertical coordinate transformation such as sigma or SLEVE coordinates (Gal-Chen & Somerville, 1975; Schär et al., 2002) and is further detailed in Ross et al., 1988. An excellent overview of the maths used to solve this optimization problem and a discussion of various considerations is given in Homicz, 2002 and a general review is provided by Ratto et al., 1994. Because an initial guess is required for w_i , HICAR allows the user to specify vertical motion as an input variable. Otherwise, w_i is taken to be 0, such that vertical motion is minimized. In the above equations, the variable α is used to control the relative weighting of changes to horizontal or vertical motion. This allows the solution to account for effects of atmospheric stability if one makes α a function of atmospheric stability. For example, larger values of α increase the weighting of changes to w from its initial value relative to changes of u and v from their initial values. This means that a better solution to the minimization would be found by preferring changes to u and v over w when eliminating divergence. The result of this is more deflection around terrain and less vertical motion, which one would expect during stable atmospheric conditions. A demonstration of the effects of different values of α is given in Figure 2.4, showing the wind field generated by the maximum (1.0) and minimum (0.1) values that α is allowed to take. For the stable condition ($\alpha = 1.0$) we see surface wind speeds approaching 10 m s⁻¹ over the ridge crest and blocking of flow upwind of the ridge. Correspondingly, vertical motion is around +/- 2 m s⁻¹ over the ridge. For the unstable case ($\alpha = 0.1$), there is comparatively little deflection of the flow field upwind of the ridge, and little speed up over the ridge crest. Vertical motion is significantly enhanced in the unstable case versus the stable case. As such, α can be used to select different solutions to the optimization problem depending on atmospheric stability.

In our implementation, the α variable is calculated at each input time step and for each grid cell according to the atmospheric stability at that location according to:

$$\alpha = \sqrt{1 - 0.5 \frac{\sqrt{1 + 4Fr^4} - 1}{Fr^4}} \quad (2.17)$$

$$Fr = \frac{WS}{L * N} \quad (2.18)$$

Where Fr is the Froude number, WS is the wind speed, L is the scale length, and N is the Brunt-Väisälä frequency (BVF). Equation #2.17 comes from Moussiopoulos et al., 1988 and is straight forward, but the calculation of the Froude number deserves further discussion. In order to calculate α in 3D, the Froude number must also be calculated in 3D. To do this, WS, L, and N are calculated for each grid cell. The scale length, L, is the height difference between the grid cell height and the largest downwind terrain element, plus some constant to ensure a minimum value for L. L is calculated for each grid cell and each wind direction at initialization so that it can be easily looked up at run time. Some search radius must be imposed when

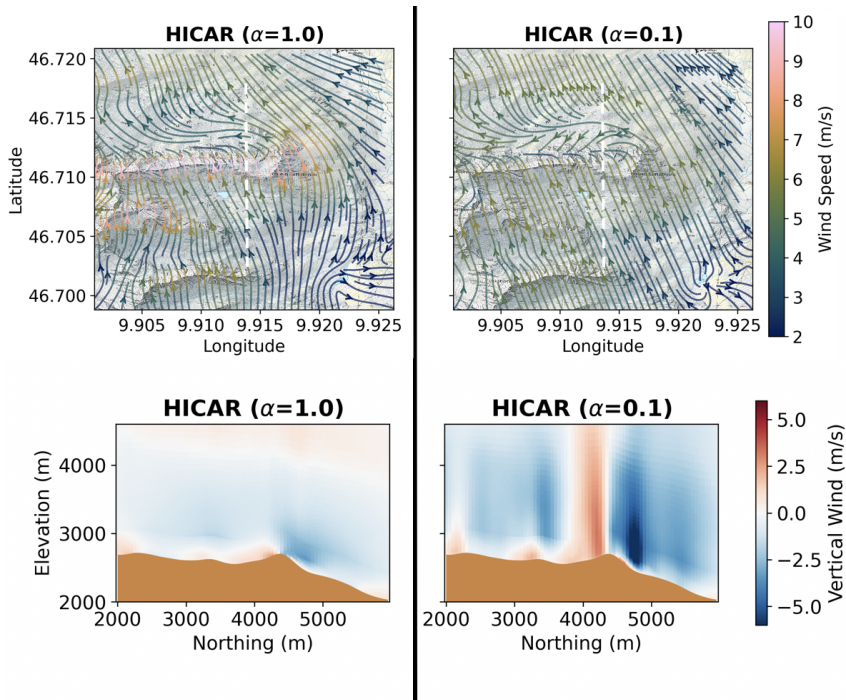


Figure 2.4: Demonstration of the two end-member solutions for HICAR's wind solver under the two extreme stability conditions. The plan view panels in the top row are centered on a ridge cutting horizontally across the figure. A vertical transect across this ridge is shown in the lower panels, with the location of the transect indicated in the upper panels by the white dotted line. Surface wind flow lines are overlaid on a topographic base map in the upper panels, with flow line color corresponding to wind speed. The left column of the figure displays the maximum stable condition, while the right column shows the maximum unstable condition.

calculating L , which we set to 4km. Brunt-Väisälä frequency is then calculated by considering the column of air above the grid cell for which it is calculated. If there is a downwind obstacle, the column of air extends from the current grid cell height up to the altitude of the downwind obstacle. If there is no obstacle, BVF is calculated using a difference over the current grid cell. The effect of these considerations is a Froude number which describes the ease of lifting a parcel of air over a given downwind obstacle. This approach of using a spatial-temporally varying α differs from prior implementations of Sherman 1978's technique, where either α was set to be 1.0 (Forthofer et al., 2014) or where α varied in time but not in space (Moussiopoulos et al., 1988). Thus our approach can handle complex situations where flow blocking varies as a function of height, such that flow may be blocked at the foot of a mountain but rise over the obstacle at higher altitudes. The computational demands of this technique are relatively small in comparison to other components of HICAR (advection, microphysics), since most of its calculations are performed once at initialization, and the solution of equations # 2.15 and 2.16 are only performed when ingesting new input data instead of at every physics time step.

2.2.3 Advection and Physics Parameterizations

The original ICAR model offers a first-order upwind advection scheme. Although this scheme is highly diffusive (Schär et al., 2002), it has the advantage of low computational demand, making it suitable for ICAR’s original development purposes and target resolutions. For our application at higher resolutions, and particularly with an interest for strongly heterogeneous precipitation patterns at the ridge-scale, a less-diffusive advection scheme was required. The issue of numerical diffusivity in complex terrain has been well documented (K. A. Lundquist et al., 2012; Westerhuis et al., 2021). Higher order advection stencils (odd-ordered up to 5th order) have thus been implemented in the HICAR model. These schemes, in combination with the SLEVE coordinate system (Kruyt et al., 2022; Schär et al., 2002), reduce numerical diffusion in HICAR simulations. To achieve larger physics time steps, a pseudo-Runge-Kutta-3 (RK3) advection integration is added to HICAR (Wicker & Skamarock, 2002). Lastly, the use of RK3 time stepping required the addition of a monotonic flux-limiter for the standard advection scheme (H. Wang et al., 2009).

Since the original publication of G16, numerous physics parameterizations have been added to the model, and will be detailed in Kruyt et al., 2023, *in prep.* Of importance to this paper, the Noah land surface model (LSM) (Ek et al., 2003), Morrison microphysics scheme (Morrison et al., 2005), RRTMG radiation scheme (Thompson et al., 2016), and the YSU PBL scheme (Hong et al., 2006) have all been added to the model and will be used for the simulations which follow in later sections.

2.2.4 Asynchronous I/O

As model efficiency increases, it is natural to push the model to run for larger domains and larger time periods. Additionally, as the simulation resolution increases, forcing data of a higher resolution is needed. The cumulative effect of these two points is that efficient, high-resolution models must output and input large amounts of data (Prein et al., 2015). For example, for the setup used in section 2.4.2, one day of simulation requires reading 11GB of forcing data and outputting 14.5GB of data, depending on output variables selected. To avoid blocking I/O operations on the runtime loop and to facilitate a many-programs one-file access pattern, an asynchronous I/O strategy was adopted. This is shown in Figure 2.1 via the blue elements on the left. Input and output is handled by a few processes which are split from the simulation processes at initialization. These I/O processes then coordinate their file access through parallel netCDF I/O, resulting in less demand on the file system and eliminating the need for stitching together output files in post-processing. These changes make the model faster by overlapping I/O with physics processes, and make it possible to directly use simulation output to force one-way nested runs, as done in section 2.4.2.

2.3 Model Setup and Datasets

2.3.1 COSMO Model

The Consortium for Small-scale Modeling (COSMO) model is run operationally by the Swiss weather service, MeteoSwiss, over a domain encompassing Switzerland (www.cosmo-model.org). COSMO is a non-hydrostatic, compressible atmospheric model capable of simulating the state of the atmosphere over complex terrain such as the Swiss Alps. Predicted variables from COSMO such as temperature, humidity, and wind speeds are made available by MeteoSwiss. Output from the 1.1km and 2km resolution COSMO simulations, COSMO1 and COSMO2, respectively, are used in this study. COSMO2 output is used to force the 1350m WRF, ICAR, and HICAR simulations discussed in section 2.4.1 and 2.4.2, while COSMO1 output is used to force the 250m HICAR simulation in 2.4.2 and 2.4.3, and the 450m HICAR simulation in section 2.4.4. The HICAR simulations are forced with specific humidity, temperature, pressure, and the 3-D wind field (U/V/W) from the COSMO model. All COSMO variables are bi-linearly interpolated in 3D to the HICAR grid using latitude, longitude, and vertical height. Then, specific humidity and temperature are forced at the boundaries, while pressure and winds are input for the full 3-D grid, with the winds being further modified using the downscaling scheme described in section 2.2.

2.3.2 WRF Model

The Weather Research and Forecasting (WRF) model (Skamarock et al., 2008) is a non-hydrostatic and compressible atmospheric model used widely in research and operational forecasting (Benjamin et al., 2016). WRF has also been successfully run at very high resolutions (50m) over the complex terrain of the alps (Gerber et al., 2018; Gerber et al., 2019; Goger et al., 2022; Kruyt et al., 2022). For these reasons, we use WRF in this study to demonstrate a "gold-standard" for atmospheric modeling in comparison to HICAR runs. All output from the WRF model comes from prior simulations first presented in Gerber et al., 2018, and thus guided the choice of spatio-temporal domain for some of the simulations presented in section 2.4. All WRF data presented is at a 50m horizontal resolution.

2.3.3 ICAR/HICAR Setup

Simulations using the ICAR and HICAR models, introduced in section 2.2, are presented in section 2.4. The HICAR simulations utilize the YSU PBL scheme, the Noah land surface model, RRTMG radiation scheme, and the Morrison two-moment microphysics scheme. The surface scheme implemented follows that detailed in (F. Chen & Dudhia, 2001). The Morrison microphysics scheme was chosen due to its demonstrated efficacy in forecasting precipitation in complex terrain (Liu et al., 2011), and use in the WRF simulations of Gerber et al., 2018. Only the wind fields from the ICAR simulations are analyzed, and because there is no physics-dynamics coupling in either ICAR or HICAR, ICAR was not run with these physics

parameterizations enabled.

HICAR has been developed as a variant of the ICAR model, as these models share a core code base. The HICAR variant of ICAR can be turned on by passing "HICAR" to the variant option of the namelist file. This switches on a number of namelist options, ensuring that the configuration is optimized for high-resolution runs in complex terrains. Specifically, the namelist options which designate a run with the HICAR model include: terrain-following SLEVE coordinates, variational-calculus-based wind solver, and wind modifications based on terrain-descriptors.

2.3.4 Spatio-temporal Domains

Sections 2.4.1 and 2.4.2, as well as the figures presented in section 2.2, use the same 50m domain introduced in Gerber et al., 2018. It is roughly 10km x 10km square, with the 50m horizontal resolution simulations covering a 24 hour period over the day of March 5th, 2016. This domain covers the Upper Dischma valley outside of Davos, Switzerland. We adopt the terminology "xx m simulation" to refer to the horizontal resolution of a simulation. The 50m HICAR and ICAR simulations for this run are nested within 150m, 450m, and 1350m simulations of the same respective model, following the methodology of Gerber et al., 2018 for their WRF runs. Importantly, ICAR/HICAR allows the use of a coarser vertical grid than WRF (Horak et al., 2021). As a result, the WRF simulations use 40, 40, 60, and 90 vertical levels for the 1350m, 450m, 150m, and 50m simulations, while ICAR/HICAR used only 20, 20, 60, and 60.

Sections 2.4.2 and 2.4.3 discuss results from a 250m simulation of HICAR covering most of the Swiss Alps from Lausanne in the west to Val Müstair in the east, for a roughly 280km X 170km domain. The simulation was run for the month of January 2017.

Section 2.4.4 repeats a benchmarking setup from Kruyt et al., 2022, running the HICAR model at a 50m resolution for five days in March 2019 over a roughly 7.5km x 7.5km domain. This 50m domain is nested within a 450m domain, following the methodology of Kruyt et al., 2022.

High-resolution domain data for all simulations comes from Gerber and Lehning, 2021, which provides ASTER Global Digital Elevation Model V002 and Corine land use data at a resolution of 1 arcsec (Agency, 2006; Spacesystems & Team, 2019). For the HICAR simulations, this terrain data was then upscaled to the desired target resolution with no smoothing applied. In order to run the WRF model at resolutions approaching 50m, certain considerations must be applied to the model topography. For the WRF simulations, to ensure model stability at reasonably long time steps, the terrain for all high-resolution simulations is smoothed using a 1-2-1 smoothing filter with 14 passes, and the terrain near the boundaries of the outer-most domain is smoothed to match the COSMO topography. Although this smoothing procedure is not required to run ICAR/HICAR, the same smoothed terrain data as the WRF simulation is used for one HICAR simulation presented in section 2.4.2. This is done in order to enable a

direct comparison between WRF and HICAR for the same topography. In a future publication, potential improvements of using unsmoothed topography on wind speeds in HICAR will be examined.

2.3.5 Gridded Datasets

In section 2.4.2, two gridded datasets for precipitation are used, MeteoSwiss's RhiresD product (MeteoCH, 2013), and the precipitation product produced by the SLF Operational Snow Hydrology Service (OSHD) using an Optimal Interpolation (OI) technique (Magnusson et al., 2014; Mott et al., submitted). RhiresD is constructed by taking precipitation data from a dense network of precipitation gauges distributed throughout the Alps, and then applying a climatological precipitation-elevation gradient to extrapolate observations beyond gauges, using a version of the PRISM algorithm (Daly et al., 1994). The OSHD precipitation product is obtained by first partitioning RhiresD into solid and liquid precipitation and then updating the snowfall fraction by assimilating snow station data from 350 locations using optimal interpolation (Magnusson et al., 2014). This allows for a higher station density at higher elevations relative to RhiresD, and minimizes underestimates of precipitation during snowfall events due to gauge undercatch. Of course, selecting for snow station sites introduces other spatial biases in station representativeness (Grünewald & Lehning, 2015). A full description of the OI procedure used in the OSHD product can be found in Mott et al., submitted.

Table 2.1: Model Configurations. For advection order, "#H" refers to the numeric order of the horizontal advection stencil, and "#V" to that of the vertical.

	Run	Wind-solver	Advection	Terrain Smoothing	Microphysics	PBL	LSM
4.1, 4.2.1							
WRF	50m	Navier-Stokes	5H, 3V	Yes	Morrison	None (LES)	Noah-MP
HICAR	50m	Variational Solver + Sx & TPI	3H, 3V	No	Morrison	YSU	Noah-LSM
HICAR, No Sx+TPI	50m	Variational Solver	3H, 3V	No	Morrison	YSU	Noah-LSM
HICAR, WRF-topo	50m	Variational Solver + Sx & TPI	3H, 3V	Yes	Morrison	YSU	Noah-LSM
ICAR	50m	Interpolation	1H, 1V	No	N/A	N/A	N/A
4.2.2, 4.3							
HICAR	250m	Variational Solver + Sx & TPI	3H, 3V	No	Morrison	YSU	Noah-LSM
4.4							
WRF	50m	Navier-Stokes	5H, 3V	Yes	Thompson-Eidhammer	LES + (Shin & Hong, 2015)	Noah-MP
HICAR	50m	Variational Solver + Sx & TPI	3H, 3V	No	Morrison	YSU	Noah-LSM
ICAR	50m	Interpolation	1H, 1V	Yes	Thompson-Eidhammer	(Hong & Pan, 1996)	Noah-LSM

2.4 Model Demonstrations

2.4.1 Wind Fields

In section 2.2.2, the effects of the changes to the wind solver were shown for comparison with ICAR (Figure 2.3) and for a demonstration of their ability to simulate atmospheric stability (Figure 2.4). To discuss the wind solver of HICAR in the context of existing atmospheric models, we present here results comparing HICAR to the WRF model. Figure 2.5 shows a plan view of multiple model simulations at 50m over complex terrain in the Upper Dischma valley of Davos, Switzerland. As discussed in section 2.2, the COSMO forcing data provided is expected to capture the effects of mountain waves which the linear wind solver of ICAR is designed to capture, so this module of ICAR was turned off. As a result, the ICAR simulation shown is bilinearly interpolated COSMO2 data. The surface flow field from ICAR is quite homogenous as a result, with uniform south-westerly flow over the domain and a narrow range of wind speeds over the domain. This is in contrast to the WRF simulation, which reports various modifications to the flow pattern (blocking, cross-slope flow, terrain-induced speed-up), as well as a larger range of wind speeds. This result is instructive that ICAR alone is not suitable for high-resolution simulations. WRF also reports higher wind speeds at ridge crests than any of the HICAR simulations, but WRF has been found to overestimate speed up of winds over topography (Gerber et al., 2018; Goger et al., 2022; Gómez-Navarro et al., 2015; Umek et al., 2021).

For examining the effects of the wind solver detailed above, we present two HICAR simulations: one with the empirical adjustments based on terrain-descriptors and one without. The simulation without terrain-descriptors uses a procedure to diagnose its winds which is similar to that employed by models like WindNinja (Forthofer et al., 2014) but, with the distinction of using a spatio-temporally varying value for α (EQ #2.17). This simulation already captures a wider range of surface wind speeds than the base ICAR model, and offers some of the flow field deflection observed with the WRF model. This is consistent with prior studies which have employed the technique from Sherman, 1978. Once the terrain descriptors are used, we see that certain features of the flow field present in the WRF simulation also emerge in the full HICAR run. Of note are the cross-slope flows and lee-side reductions in wind speed. Due to the improved terrain representation capable with the ICAR/HICAR model, these flow features develop for secondary valleys not fully resolved in the WRF topography. This demonstrates the added value of this two-step approach to generating a diagnostic, mass-conserving wind field.

The advantages of the terrain descriptors are on show in Figure 2.6 as well. This figure presents a vertical cross section of modeled flow across the Sattelhorn ridge, which is in the upper-center of Figure 2.5. The WRF model shows a large eddy in the lee-side of the ridge, with a long horizontal extent and reduced wind speeds relative to the flow outside of the lee. This eddy also gives rise to up-slope flow at the surface of the lee of the ridge. The HICAR run simulates a similar dynamic structure. The eddy present in HICAR has a shorter horizontal extent and is stronger, resulting in higher wind speeds within the eddy and faster reverse flow

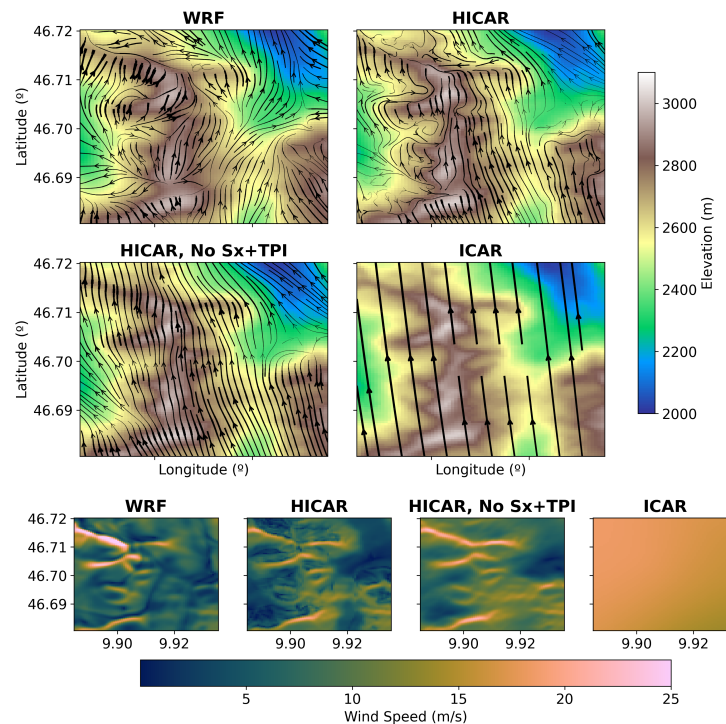


Figure 2.5: Comparison of surface flow fields at a 50m resolution between models and model setups for March 5th, 2016, 00:00 UTC+1. The upper four panels show flow fields overlaid on model topography. Model topography is smoothed for the WRF run compared to the HICAR/ICAR runs. Thickness of flow lines corresponds to wind speed, with thicker flow lines indicating higher wind speeds. The lower row of panels displays the surface wind speeds of the various model runs. The sparser flow lines for the ICAR simulation are a plotting decision to avoid redundancy and do not reflect a difference in the simulation setup. The orange arrow indicates the location of the Sattelhorn Ridge, which is shown in profile in Figure 2.6.

at the surface of the lee. Despite these differences in the properties of the eddy, the ability of HICAR to predict the presence of such flow features is a surprising result, since no prior applications of Sherman 1978's technique have reported such behavior. We attribute this to our use of terrain-descriptors, which predispose the solution of Sherman 1978 to generate an eddy in the lee, all of which may be due to the sharper terrain represented by HICAR. It is easy to imagine how this approach of pre-conditioning a wind field and then using a diagnostic, mass-conserving solver, could be used to parameterize other dynamic effects, and has previously been shown to yield reasonable results when parameterizing thermally driven winds (Forthofer, 2007). We also note that the calculation of the terrain-descriptor based corrections depends upon somewhat arbitrary constants, and thus could be adjusted to yield eddies of varying horizontal extent. This tuning of the terrain-descriptor-based adjustments

will be done in a future study, using distributed observations of winds in complex terrain as a basis for tuning and validation.

The differences in terrain representation between WRF and ICAR/HICAR are also on display in Figures 5 and 6. WRF and other models which prognostically solve for winds rely on spatial gradients of pressure to calculate wind speeds. In order to simplify the lower boundary condition, these models also typically employ terrain following coordinates where model coordinate surfaces slope as the terrain does. This means that high-resolution simulations will feature large coordinate distortion, and pressure differences in the horizontal may become quite large as one vertical cell surface exists at lower elevations than another. This may lead to large pressure gradients which require very fine time steps to stably integrate. The model terrain is typically smoothed to allow for smaller grid distortions, smaller pressure gradients, and thus larger time steps. Recent implementation of an immersed boundary method in WRF allows for this entire consideration to be skipped, although such a domain discretization comes with its own trade-offs (K. A. Lundquist et al., 2012).

The above discussion is valid for atmospheric models which solve prognostic equations for momentum. Neither the ICAR model nor the HICAR variant do this, opting for diagnostic solutions for the wind field instead. As a result, issues of model stability arising from terrain steepness do not exist, and we can include model terrain without any artificial smoothing or implicit numerical diffusion. This is apparent in the elevation profile of Figure 2.6 and, to a lesser extent, in the DEM of Figure 2.5. The difference in terrain used may lead to the different lee-side dynamics when comparing the HICAR and WRF simulations. This ability of ICAR and HICAR to represent the terrain without any artificial smoothing is a major strength of both models. High-resolution atmospheric modeling is assumed to yield more accurate forecasts in part through improved representation of the underlying terrain. If HICAR can represent topography more accurately than WRF at the same horizontal resolution and without explicit numerical diffusion, it allows for effectively higher model resolutions than WRF.

2.4.2 Precipitation Distribution

Ridge-scale

The above discussion of terrain representation also plays an important role in precipitation distribution, as is on display in Figure 2.7. There are noticeable differences in the snowfall transects of the two HICAR simulations, one using the unsmoothed topography (HICAR) and the other using WRF's smoothed topography (HICAR, WRF-topo). This result supports the above point that HICAR's improved terrain representation leads to a higher effective model resolution, impacting the simulation results. We also note a strong wet-bias over the domain for the WRF model, with precipitation amounts nearly double what was recorded at a snow depth station located in the domain (Figure 2.7). This wet bias was attributed to excessive orographically enhanced precipitation in Gerber et al., 2018. The snowfall transects reveal ridge-scale differences in precipitation for all model simulations, with the windward (left) side

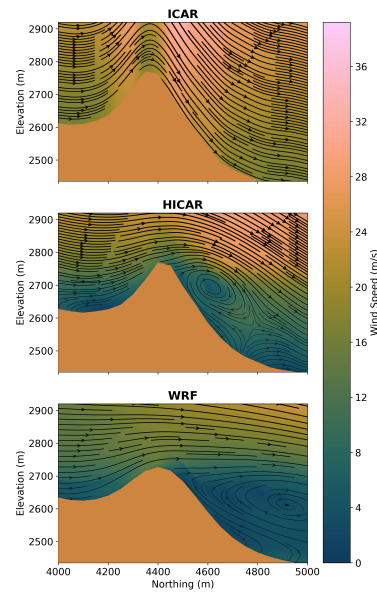


Figure 2.6: Profile view of flow fields at a 50m resolution between models for March 5th, 2016, 02:00 UTC+1. Wind direction is indicated by the flow lines, and line thickness corresponds to wind speed, where thicker lines show higher wind speeds. Wind speed is given by the background color. A profile of the underlying terrain is shown in each panel, with the WRF simulation having smoother terrain than the ICAR or HICAR simulations.

of the ridge receiving approximately 15% more snowfall than the leeward (right) side in the HICAR simulations. The WRF simulation shows a similar although more modest ridge-scale difference, with a positive snowfall anomaly (relative to mean over the transect) beginning on the windward side and continuing until just downwind of the ridge, followed by a steady decrease in snowfall anomaly. The main difference between the HICAR and WRF simulations are the magnitude of the windward and leeward differences. This can be partly explained by the leeside dynamics simulated by both models. Taking the flow profiles shown in Figure 2.6 to be representative of the flow differences over the 24-hour event, we note that HICAR has higher wind speeds aloft on the leeside of the ridge due to the presence of the eddy. The peak in precipitation on the windward side is likely due to blocking of the lowlevel flow and reduced wind speeds on this side of the peak (Figure 2.6). We note a positive anomaly in snow depth just downwind of the ridge, which we attribute to the strong horizontal wind speeds aloft, inline with previous studies of preferential deposition (Mott et al., 2014; Z. Wang & Huang, 2017). In fact, the HICAR snow depth distributions show a similar windward/leeward pattern to results obtained by Comola et al., 2019 using an LES model over ideal topography. This cumulative effect of the flow field on snow depth can be realized intuitively by tracing the flow lines of Figure 2.6 across the ridge and imagining snow sedimentation given a constant sedimentation rate. The question of if this flow pattern is accurate for this particular event

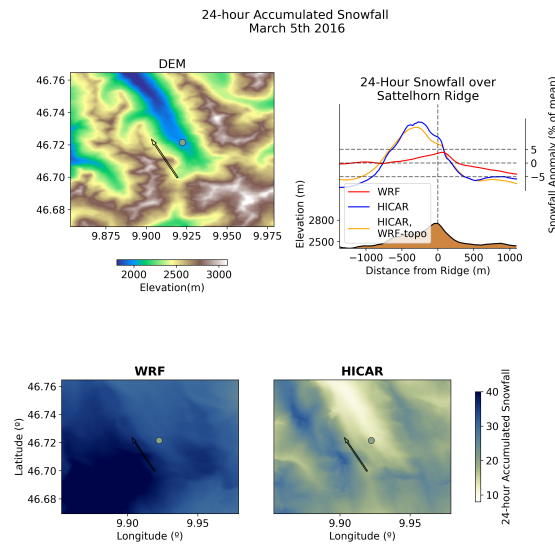


Figure 2.7: Differences in snowfall over the Upper Dischma Valley for a 24-hour snowfall event on March 5th, 2016. All terrain data displayed is from the unsmoothed HICAR run. All values of snowfall are reported in cm, with the WRF and HICAR snowfall values converted from mass to depth assuming a constant density of 100 kg m^{-3} . The upper left panel shows a DEM of the area, with a dot in the valley indicating the location of a snow depth sensor an arrow indicating the location and direction (left-right) of the transect shown in the upper right panel. This arrow points along the prevailing wind direction during the 24-hour snowfall. The upper right panel shows snow depth transects across the Sattelhorn ridge for three model simulations, WRF, HICAR, and HICAR run with the same smoothed topography as WRF. Mean snowfall is almost twice as large in WRF than in HICAR, so snow depth is reported as percentage of the mean snow depth along the transect in order to compare the HICAR and WRF simulations on the same graph. The lower two panels show the spatial distribution of snow depth across the domain, with the value recorded at the snow depth station over the 24-hour period (20.3cm) overlaid.

has not been demonstrated, but given the proven accuracy of HICARs advection scheme (H. Wang et al., 2009), the resultant deposition pattern is certainly physically consistent with the given flow field. This discussion demonstrates the research utility of HICAR: it can be used to efficiently (Section 2.4.4) test different flow patterns at the ridge scale and see how they affect particle-flow interactions. A later validation of HICARs flow fields would determine how predictive the simulated deposition patterns are.

Range-Scale

Accurate high-resolution precipitation estimates in complex terrain are a slippery target (Bonekamp et al., 2018; J. Lundquist et al., 2019). Gauge-based gridded products are subject

to gauge undercatch, and assumptions about the spatial patterns used to interpolate them (Collados-Lara et al., 2018; J. D. Lundquist et al., 2010; R. Rasmussen et al., 2012). Radar products meanwhile suffer from occlusion when scanning in complex terrain (Germann et al., 2022). As a result, high-resolution comparisons of modeled versus observed precipitation in complex terrain deserve careful consideration to offer any form of model validation. We spare any detailed quantitative validation for a future study, and instead offer a comparison of different gridded precipitation products for the sake of discussion.

Figure 2.8 shows accumulated precipitation for January 2017 from two gridded products and a 250m HICAR simulation. We first note that the majority of storms during January 2017 came from the northwest, and our simulation domain for HICAR extended slightly beyond the boundaries of the figure shown to just include the Swiss Plateau. The HICAR simulation is forced with only water vapor from COSMO1, so the microphysics requires some time to "spin-up", generating hydrometeors and thus precipitation. This may explain some of the lower precipitation amounts along the pre-Alps in the upper northwest of the figure relative to both RhiresD and the OSHD precipitation product.

Overall, Figure 2.8 shows remarkable agreement between HICAR and the two gridded precipitation products for a one month winter period. The OSHD precipitation product gives larger precipitation values at higher elevations than RhiresD since it is generated by back-calculating precipitation from snow water equivalent, avoiding gauge undercatch during snowfall events (Magnusson et al., 2014). This result suggests that the larger precipitation values obtained from the HICAR simulation are possible. The inter-alpine areas (center) of the domain however show less precipitation in HICAR than either gridded product, especially in the valleys. However, these differences between HICAR and the other gridded products are comparable to differences observed between the gridded products themselves. Lastly, we note that the product using climatological averages for its interpolation, RhiresD, returns a smoother field of precipitation than either HICAR or the OSHD product. The OSHD product yields stronger elevation gradients of precipitation, which is likely due to its higher station density at higher elevations relative to RhiresD, and its ability to capture unbiased precipitation during snowfall events. This suggests that the stronger gradients observed from HICAR are appropriate. None of this discussion is to assert an accuracy of one product over another, but is instead to demonstrate that HICAR's precipitation estimate is as consistent with existing precipitation products as those products are with each other.

2.4.3 Cold Air Pooling

Figure 2.9 shows a cold air pooling event on the morning of January 24th, 2017. We observe that, over the course of the early morning hours, strong mesoscale winds recede from over the valley, allowing a cool, stable boundary layer layer to develop and for that cool air to migrate toward lower elevations. This surface layer is ultimately re-mixed as wind speeds increase and surface cooling decreases around 9 AM local time. These results are somewhat

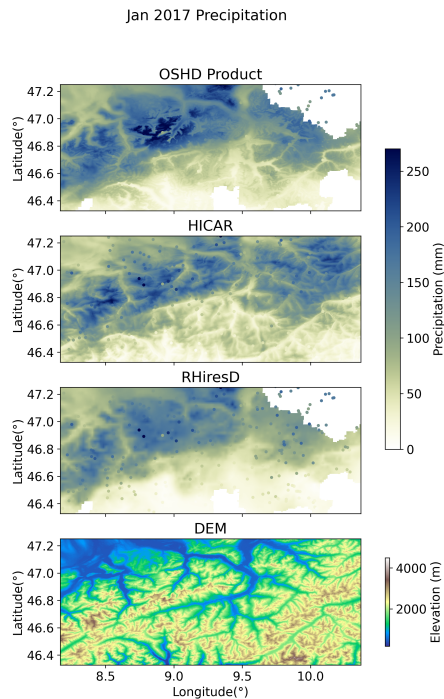


Figure 2.8: Precipitation over the central and eastern Swiss Alps during January 2017 at a 250m resolution. All three plots of precipitation have point data from the OSHD product overlaid as dots. Since these mostly coincide with the same values for the OSHD product, the dots are often indistinguishable from the background field in the top panel.

surprising, as a parameterization of thermally driven flows is not yet included in HICAR. Thus, the flow patterns shown are largely unaware of the evolving thermal stratification of the valley. However, the wind solver used in HICAR is designed to minimize differences between its wind field and the wind field supplied from the forcing data. The driving model, in this case COSMO1, has been shown to simulate valley winds supportive of cold air pooling (Goger et al., 2018), so if the LSM of HICAR simulates a cooling of the surface, cold air pooling as shown in Figure 2.9 is possible. This figure demonstrates an important caveat of the HICAR model: its dependency on physically consistent winds from forcing data. The simulation shown here was forced with COSMO1 data at the boundaries, while the model runs in prior sections examining HICAR’s wind field were forced with COSMO2 data. A test of HICAR’s sensitivity to the resolution of the driving model is needed, but is beyond the scope of this study. At present, only forcing data at resolutions where mountain waves can be expected to be resolved have been used. Yet, as noted in section 2.2, regional forecasting offices are increasingly providing model output at these resolutions.

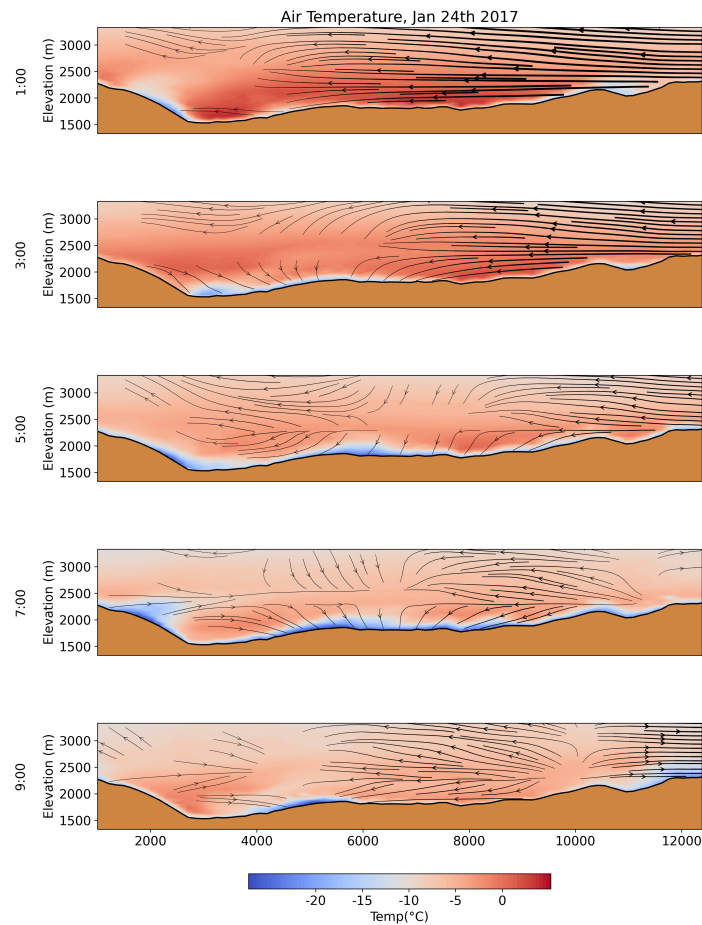


Figure 2.9: The development and diffusion of surface cooling for an alpine valley during dawn. The plot shows a small area of the 250m Swiss Alp domain introduced in section 2.3.4. The local time is indicated on the y-axis label. Wind vectors are plotted for wind directions along the transect. Thicker vectors indicate higher wind speeds, and winds below 0.2 m s^{-1} are not plotted.

2.4.4 Computational Efficiency

The main reason why HICAR may be attractive as a model is through its computational efficiency relative to existing atmospheric models such as WRF or COSMO. Aside from HICARs improved representation of terrain, the model is not expected to simulate physical phenomena better than more complex models. Thus, understanding its computational demand is central to establishing its utility. To quantify this demand, we repeat a benchmarking setup described in Kruyt et al., 2022. We run HICAR at a 50m resolution over a roughly $7.5 \times 7.5 \text{ km}$ domain for a 5 day period in March 2019, which includes several winter storms. The model numerics/physics setup is the same as those used for the above subsections for which results are shown. The results of the benchmarking test are presented in Table 2.2, alongside the results previously published in Kruyt et al., 2022. The main takeaway from this comparison

Table 2.2: Core-hours per simulation day for benchmarking run

	WRF	ICAR	HICAR
Core-hours	33,993	1,336	57
Speed-up over WRF	1.0	25.4	594.3

is that HICAR uses 594x fewer computational resources than WRF for the same simulation. Stated otherwise, a year of simulation over this domain with WRF would require a significant allotment of computing time (350,000 node hours, assuming 36 cores per node). With HICAR, the same simulation represents a fraction of a modest project allocation (590 node hours).

The more than twenty-fold speedup of HICAR relative to ICAR is also somewhat surprising. This result is best explained by the switch from the GNU fortran compiler to the Cray compiler and aggressive optimization of the model code outside of the physics parameterizations. Of these optimizations, one of the most effective at reducing runtimes was moving to batched message passing between parallel processes. Testing of Coarray fortran, on which ICAR is parallelized (S. Rasmussen et al., 2018), has revealed the Cray compiler to have a faster implementation of this fortran standard than GNU. Additionally, the high-performance computing architecture used in this study is the Piz Daint computer, featuring Cray XC40 compute nodes. The use of a native compiler may contribute to speed up as well. The WRF runs here were performed with the Intel compiler, and were not re-run for this study with the cray compiler due to constraints on computational resources. Prior studies using WRF on the same computing architecture additionally recommend the use of the Intel compiler (Gerber & Sharma, 2018).

2.5 Conclusions

In this paper we have introduced the High-resolution variant of the ICAR model, HICAR. We detailed its primary modifications to adapt it for simulations over high-resolution complex terrain. This consists primarily of a new approach to solving for a 3D wind field which utilizes terrain-descriptors, TPI and S_x , to pre-condition the input wind field to approximate some expected effects of the topography on the flow field (Figure 2.2). These effects are parameterized simply and rely on assumptions and somewhat arbitrary constants. The model's sensitivity to these constants will be further investigated in a future study. After this correction step, the pre-conditioned wind field is fed into an optimization routine, which makes the resulting field mass-conserving while minimizing changes to the pre-conditioned field (Figure 2.1). A novel approach to the diagnostic wind solver is adopted which allows atmospheric stability to influence the solution as it varies in time as well as space. This allows for low-level flow blocking, leeside recirculation, and cross-slope flows to be simulated by the model. These changes to the wind solver, in addition to a new advection scheme and physics parameterizations, enable the results demonstrated in section 2.4.

We observe a marked improvement in the representation of wind fields in complex terrain

over the base ICAR model when comparing against the WRF atmospheric model (Figure 2.5). By avoiding the Navier-Stokes equations, HICAR is also able to run stably over steeper terrain than WRF, and thus may resolve flow features induced by small-scale topography which WRF cannot (Figure 2.5). These improvements to the wind field make HICAR capable of simulating heterogeneous snow deposition patterns in complex terrain, which show clear signals resulting from terrain-flow interactions (Figures 6 and 7). At larger scales, precipitation patterns in complex terrain are represented to the same goodness as existing gridded precipitation products (Figure 2.9). ICAR/HICAR also forgoes any consideration of pressure gradients in its dynamics, allowing it to be run without any smoothing of the underlying terrain. Most importantly, all of these developments were done while maintaining the orders of magnitude speed up over WRF which ICAR originally demonstrated. The result is a model which is 594x faster than WRF and can run at very high resolutions (50m), extending intermediate complexity atmospheric modeling into the resolutions typically used by land surface modelers. HICAR's ability to handle very steep terrain, coupled with its computational speed, seems well suited for modeling efforts over High Mountain Asia, where testing of various model configurations is already performed with more computationally expensive models (Bonekamp et al., 2018). HICAR's computational efficiency also enables high resolution simulations over long time scales, supporting climate impact studies at the regional scale and seasonal studies of coupled glacier-atmosphere or snow-atmosphere models at hectometer scales. This last point will be expanded upon in future publications, where HICAR will be coupled with an intermediate complexity snow model to enable high-resolution forecasting of winter snowpack and spring melt. This will involve the addition of a thermal wind parameterization to improve surface flows over glaciers and snow (Mott et al., 2020), with the goal of better resolving advective surface-atmosphere processes such as turbulent heat exchange. As atmospheric models begin to regularly probe higher resolutions, HICAR enables rapid testing and iteration of various model configurations with relatively little computational cost. This makes HICAR a powerful companion to conventional atmospheric models.

Code and Data Availability

HICAR can be used for non-profit purposes under the GPLv3 license (<http://www.gnu.org/licenses/gpl-3.0.html>, last access: 1 February 2023). Code for the model is available at <https://github.com/HICAR-Model/HICAR>. The exact release (v1.1) used in this publication is available at <https://doi.org/10.5281/zenodo.7920422>. The model has dependencies for the netCDF4-parallel fortran and PETSc libraries. Parallellisation is achieved through fortran Coarrays, which utilizes different message passing protocols depending on the compiler used. For use with the GNU fortran compiler, OpenCoarrays is required.

Acknowledgements

The authors thank the funding source of this project, the Swiss National Science Foundation grant #188554. The computational resources needed to perform the simulations were provided by the Swiss National Supercomputing Center (CSCS) through projects s1148 and s999.

Chapter 2. The HICAR Model

The authors would like to thank Jean-Marie Bettems and Petra Baumann for their helpful correspondence when working with COSMO data hosted by MeteoSwiss. Developers of open source python toolboxes, particularly xarray and xesmf, have also played a crucial role in this study by enabling efficient analysis and manipulation of large datasets. Perceptually uniform colormaps are selected from the library provided by Crameri, 2021.

3 Intermediate Complexity Atmospheric Modeling in Complex Terrain: Is it Right?

This chapter corresponds to the version of the article submitted to the journal *Frontiers in Earth Science: Cryospheric Sciences* by the authors:

Dylan Reynolds, Michael Haugeneder, Michael Lehning, and Rebecca Mott

Abstract Dynamic downscaling of atmospheric forcing data to the hectometer resolution has shown increases in accuracy for landsurface models, but at great computational cost. Here we present a validation of a novel intermediate complexity atmospheric model, HICAR, developed for hectometer scale applications. HICAR can run more than 500x faster than conventional atmospheric models, while containing many of the same physics parameterizations. Station measurements of air temperature, wind speed, and radiation, in combination with data from a scanning Doppler wind LiDAR, are compared to 50 m resolution HICAR output during late spring. We examine the model's performance over bare ground and melting snow. The model shows a smaller root mean squared error in 2 m air temperature than the driving model, and approximates the 3D flow features present around ridges and along slopes. Timing and magnitude of changes in shortwave and longwave radiation also show agreement with measurements. Nocturnal cooling during clear nights is overestimated at the snow covered site. Additionally, the thermal wind parameterization employed by the model typically produces excessively strong surface winds, driven in part by this excessive nocturnal cooling over snow. These findings highlight the utility of HICAR as a tool for dynamically downscaling forcing datasets, and expose the need for improvements to the snow model used in HICAR.

3.1 Introduction

The state of the atmosphere is intertwined with land surface processes in a myriad of ways, affecting surface surface mass and energy balances through wind driven transport or radiative

forcing, to name just two. The scales of these processes are often very heterogeneous, with ridges and depressions modifying the wind field over horizontal scales of tens of meters (Mott et al., 2010b; Raderschall et al., 2008; Sauter & Galos, 2016). While land surface models have been run at the spatial scales of these heterogeneous processes for decades (Lehning et al., 2006b; G. E. Liston & Elder, 2006a; Sauter et al., 2020), they are not responsible for simulating these processes themselves. Instead, information about these processes are passed to land surface models through the atmospheric forcing data supplied to the models. One way of obtaining this forcing data is through dynamic downscaling, where atmospheric models are forced with coarse-resolution atmospheric data and run at a target horizontal resolution. Dynamic downscaling has been used at the scale of tens of kilometers for downscaling re-analysis data (Bozkurt et al., 2019) and has led to improvements in representing land surface processes at these scales (Gao et al., 2017; Sharma et al., 2023). Applications of dynamic downscaling for forcing land surface models at the hectometer scale are sparse, but similarly show improvements over other downscaling techniques (Vionnet et al., 2017; Voordendag, Goger, Prinz, et al., 2023). However, the computational demands of dynamic downscaling to the hectometer scale limit the application to short time series (hours to days) and small domains (catchment scale) (Gerber et al., 2018; Goger et al., 2022; Saigger et al., 2023; Sauter & Galos, 2016; Vionnet et al., 2021)).

This has led to widespread use of statistical downscaling in the land surface modeling community at the hectometer resolution. Statistical downscaling techniques have yielded reasonable simulations of seasonal snowpack (Dadic et al., 2010; Winstral & Marks, 2002), but often fail to capture inter-variable dependencies (Michel et al., 2021). Statistical downscaling treats variables in a "piece-wise" approach where each atmospheric variable is downscaled separately from one another. Thus dynamic downscaling is expected to better represent processes such as preferential deposition of snow (Lehning et al., 2008), where the interaction between terrain features and atmospheric stability induce changes in near-surface vertical winds, which in turn modify the deposition of precipitation (Z. Wang & Huang, 2017). Additionally, statistical downscaling approaches may assume spatial patterns to be temporally fixed, limiting their use in climate change studies where the validity of these assumptions is unknown (Gutiérrez et al., 2013; E. D. Gutmann et al., 2012). Thus, although they have high computational costs, physics-based dynamic downscaling remains attractive for many downscaling problems, especially under future climate scenarios.

To provide an alternative to weather models typically used in dynamic downscaling studies, the Intermediate Complexity Atmospheric Research (ICAR) model was proposed (E. Gutmann et al., 2016). ICAR was evaluated alongside the WRF model (Skamarock et al., 2008) in a previous study, showing predictive accuracy of wind speed and temperature similar to the WRF model at a handful of stations (Krutz et al., 2022). However, the ICAR model suffered from little diurnal variability at a valley site, as well as a lack of ridge-scale flow features when compared to observations or the WRF model. These issues largely stem from ICAR being developed with a focus on downscaling to target resolutions at the kilometer scale, and not at the hectometer scale, where the evaluation was performed. To improve on these shortcomings,

the High-resolution Intermediate Complexity Atmospheric Research (HICAR) model was recently introduced, addressing shortcomings in ICAR's dynamics at high resolutions while still more than 500x faster than the WRF model (D. Reynolds et al., 2023). A direct validation of the HICAR model is still needed to understand how useful it may be for applications of dynamic downscaling. This study presents such a validation, focusing on processes which are of particular relevance to seasonal snowpack modeling. At the hectometer scale, flow features such as leeside recirculation, turbulent eddies, and thermally driven slope flows all dominate the near-surface flow field. Leeside recirculation can result in preferential deposition during snowfalls (Lehning et al., 2008), turbulent eddies enhance surface energy exchange (Haugeneder et al., 2024), and thermal flows effectively distribute surface heating throughout the surface layer (Farina & Zardi, 2023). This surface heating is itself driven by radiative forcing, which depends upon both cloud cover as well as topographic shading. HICAR's ability to represent these processes is crucial for solving the surface energy balance and, particularly in the case of snowpack models, the surface mass balance.

This paper continues with section 3.2, where an overview of an observational campaign which occurred during winter 2021/2022 is given. Section 3.2 also contains a description of model changes implemented to represent some of the high-resolution processes discussed above. Section 3.3 presents a comparison of HICAR simulations with observations, focusing on near-surface flow features observed by a Doppler wind LiDAR. Lastly, a conclusion and summary of the study's main points are given in section 3.4.

3.2 Methods

3.2.1 Observational Campaign

In late April and Early May of 2022, a field campaign was conducted over a mountainous region outside of Davos, Switzerland, in the eastern Swiss Alps (Figure 3.1). A wind LiDAR (Section 3.2.1) was deployed within this domain, and five existing automatic weather stations (AWS) nearby recorded air temperature, wind speed, and wind direction during the period of the campaign. One station, located at the exposed summit Weissfluhjoch (WFJ), lies roughly 2km south of and 400 m above the wind LiDAR. In this way, the WFJ station gives an estimate of the mesoscale conditions over the study area. The five stations included in the study are a part of two different measurement networks: the Swiss Meteorological Network (SMN) and the Intercantonal Measurement and Information System (IMIS). Sensors in the SMN feature ventilated temperature sensors, while the sensors in the IMIS network feature standard, solar-shaded temperature sensors. For wind sensors, IMIS stations sport propeller-type anemometers, while the SMN stations have 2D sonic anemometers.

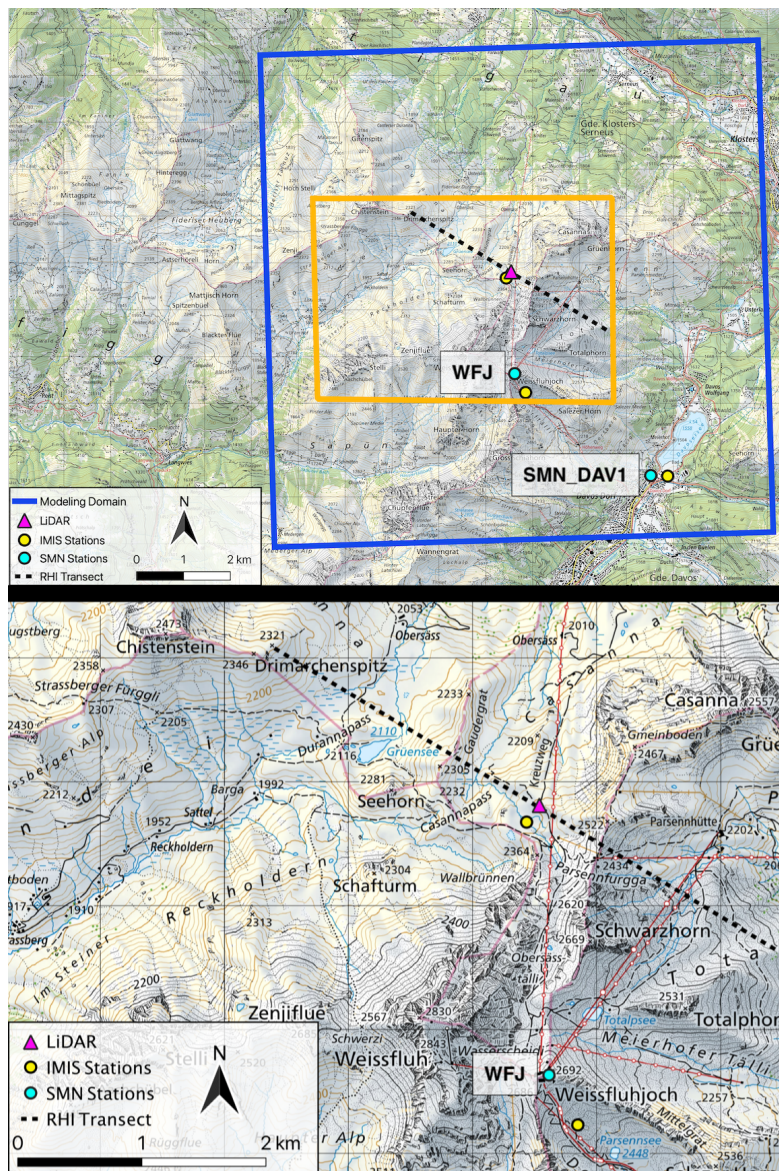


Figure 3.1: Map of the study domain. The upper panel shows the region around Weissfluhgipfel in the eastern Swiss Alps. The cyan dots indicate the location of the Swiss Met Net (SMN) weather stations, which feature ventilated temperature sensors. The yellow dots correspond to stations from the Intercantonal Measurement and Information System (IMIS). The WFJ and SMN_DAV1 SMN stations shown in Figures 3.3 and 3.4 are labeled. 50 m HICAR simulations were performed over the area contained within the blue square. The orange rectangle indicates the region shown in detail in the lower panel. This area focuses on the region around the wind LiDAR deployment, with the wind LiDAR shown as a pink triangle, and the orientation of the RHI scans presented in section 3.3 given by the dashed black line. Of note are the Gaudergrat and Parsennfurrga, which the RHI transect crosses to the left and the right of the LiDAR, respectively.

Wind LiDAR Scans

To validate the representation of wind speeds and flow features in HICAR, a Halo Photonics Streamline Doppler LiDAR was deployed. The ridge of Gaudergrat lies roughly the same elevation to the west of the location, while the pass Parsennfurgga rises over the LiDAR to the east. RHI scans were conducted every half hour to sample the flow structures over both terrain features, starting over the Gaudergrat and ending at Parsennfurgga. The LiDAR was deployed from April 22nd to May 10th, with atmospheric conditions supporting good scan returns from May 1st to May 5th.

RHE Scans

In addition to conventional RHI scans, we also introduce a new scan type, Reynolds-Haugeneder Elevation (RHE) scans. These scans are essentially PPI scans, with varying elevation angles designed to minimize the distance between the laser and the underlying terrain. In this way, the ridge crest flow is best sampled for all points around the LiDAR. RHE scans are created by taking a high-resolution DEM of the LiDAR area, and shooting rays outward from the position of the LiDAR at each of the azimuthal scan angles 3.2. These rays increase in elevation angle, from 0° upwards until they no longer intersect the surrounding DEM. This elevation angle is then saved as the elevation angle for the current azimuthal angle, and the next azimuthal angle is considered. RHE scans avoid large overshoots of the terrain which occur in PPI scans, and which are not helpful when validating near-surface flow features.

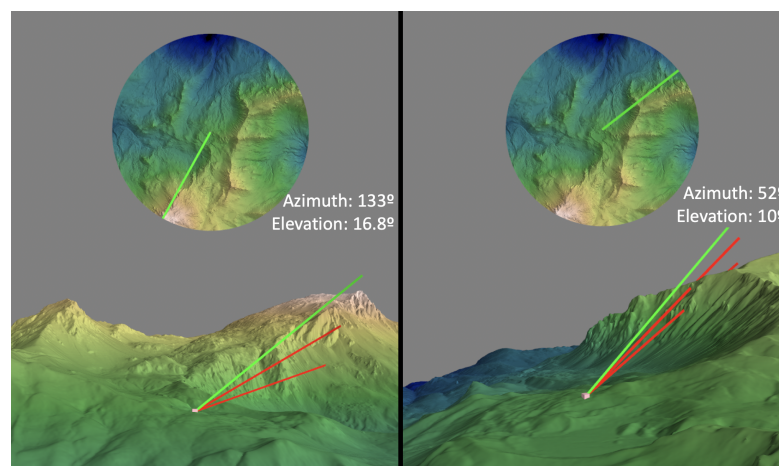


Figure 3.2: Schematic of how RHE scan angles are determined. The upper, circular graphics show the domain from above, with north facing upward. The green line cutting across the circle corresponds to the scan line from the wind LiDAR. In the bottom of the two panels, the view of the LiDAR in the terrain is shown, with the process of iteratively increasing the elevation angle until it clears the terrain. The azimuth of each scan, and the resultant scan elevation determined, is shown.

3.2.2 Model Changes

The measurements in section 3.2.1 were conducted to validate a novel atmospheric model, HICAR (D. Reynolds et al., 2023). This model lacks a traditional Navier-Stokes-based dynamical core, and instead substitutes a diagnostic solution for the 3D wind field. This saves significant computational time, but the predicted flow structures have not yet been validated against observations. In addition to the near-surface flow parameterizations existing in HICAR, a parameterization of thermal flows has also been introduced since the publication of (D. Reynolds et al., 2023). The following sections detail model changes relevant to this thermal-flows parameterization. The terrain parameters required in the following sections, including those for terrain-shading of radiation and the ridge distances for the slope flow parameterization, can be calculated using a python script contained in the HICAR distribution.

Thermal Flow Parameterization

One potential application of HICAR is modeling the seasonal snowpack. In snow-covered environments, katabatic winds, and the interplay between katabatic and valley winds in the spring play an important role in the surface wind field (Haugeneder et al., 2024). To address this, a thermal flow parameterization has been added to HICAR following the formulation in (Grisogono et al., 2015) based on the popular Prandtl model of thermal winds (Prandtl, 1942). This model extends an existing parameterization of thermal winds, that of Oerlemans and Grisogono, 2002, which was tested over an alpine glacier and showed reasonable agreement with station observations up to a height of 13m. The updated formulation in Grisogono et al., 2015 allows for a vertically varying thermal eddy diffusivity and for the inclusion of additional terms representing enhanced mixing due to induced near-surface temperature gradients during anabatic winds. A full derivation of their method is included in the above publication. One mechanism of note is that the strength of the thermal flow correction is largely dependent on the temperature anomaly between the surface and the air aloft, in this case 200 m above the surface. Another important feature of this enhanced parameterization is that it produces stronger thermal flows over shallower slopes than steeper ones. The physical reason for this is the adiabatic heating that occurs to an air mass as it descends to lower altitudes. This heating rate is balanced by cooling due to negative sensible heat fluxes. As a slope becomes steeper, an air mass descends more elevation, and thus experiences greater adiabatic heating, while covering less distance along the terrain where cooling of the air parcel may occur. For slopes of lower angle, the air parcel traverses a greater distance along the terrain to cover the same vertical drop, resulting in a greater net cooling of the air mass, a larger density difference to the surrounding air, and thus stronger katabatic winds. Modeling studies using LES simulations and observational campaigns have noted that slopes of intermediate angle should experience stronger katabatic flows when compared to steep slopes or very flat slopes (Zardi & Whiteman, 2013; Zhong & Whiteman, 2008). An LES study of upslope flows over slopes of various angles showed a similar dependency of maximum wind speed on slope angle, perhaps due to the same mechanism acting in reverse (Schumann, 1990).

The thermal wind parameterization introduces a dependency of the winds on physics processes which are updated more frequently than model input data is ingested. In version 1.1 of HICAR, a new wind field was only solved for each input time step. To more tightly couple the model dynamics with the physics, an update to HICAR's wind solver has been added, allowing for more frequent solutions to the wind field. In the current study, this has been set so that a new wind field is solved for every ten minutes of simulation time, allowing for the modeled surface winds to respond to rapidly changing surface energy fluxes around sunrise and sunset.

Physics Parameterizations

The new thermal flow parameterization in HICAR depends in part upon the surface sensible heat flux calculated by a land surface model. Daytime sensible heat fluxes are driven primarily by incoming radiation at the grid cell. To this point, the RRTMG radiation transfer scheme (Thompson et al., 2016) is used in HICAR to compute both direct and diffuse shortwave radiation, as well as incident longwave radiation (Thompson et al., 2016). These radiation fields are then modified to account for sloping terrain surfaces and occluded sky view from surrounding terrain (Mott et al., 2023). The computation of these terrain parameters, namely horizon line and sky view fraction, is normally computationally expensive, especially for high-resolution domains with many grid points. We use the HORAYZON python library developed by Steger et al., 2022 to efficiently calculate these terrain parameters for our domain.

These terrain-modified radiation inputs are then passed to the land surface model (LSM). NoahMP has been added to both the ICAR and HICAR models, widening the choice of land surface process representations. NoahMP has also been modified in HICAR to allow for the incident direct and diffuse shortwave radiation amounts calculated by RRTMG to be used directly, instead of a fixed partitioning of 70% direct and 30% diffuse hard-coded into NoahMP. These modifications allow for NoahMP to give improved estimates of sensible heat flux in complex terrain. NoahMP contains its own formulation for calculating surface exchange coefficients, and is not coupled to the surface exchange coefficients calculated by the surface layer scheme. To improve the representation of surface-atmosphere energy exchange, in particular during stable conditions, we add the revised MM5 surface layer (Jiménez et al., 2012) scheme's calculation of exchange coefficients to NoahMP. To make this change to NoahMP consistent with the rest of the model physics, the revised MM5 surface layer scheme itself has been added to the model, and coupled to the Yonsei University (YSU) PBL scheme (Hong et al., 2006).

Lastly, the ISHMAEL microphysics scheme (Jensen et al., 2017) has also been added to HICAR, with the necessary steps to couple it to the RRTMG radiation scheme. This novel microphysics scheme is part of the growing class of adaptive habit (AHAB) microphysics schemes capable of evolving solid hydrometeor shape through time. This ability is crucial for resolving particle fall speeds and, thus, mass and energy exchange rates between hydrometeors and the atmosphere. For these reasons, the ISHMAEL scheme is also expected to offer an improvement in cold-cloud microphysics relative to the Morrison microphysics scheme (Woods et al., 2007). Taken

together, the ISHMAEL scheme may improve patterns of snowfall deposition in complex terrain and the mass-energy exchange between hydrometeors and the atmosphere. To evaluate the impact of this novel microphysics scheme, we perform HICAR simulations with both the Morrison and ISHMAEL schemes in Section 3.3.

3.2.3 Modeling Setup

To evaluate the HICAR model, it was run over a period covering the observational campaign described above. Following the methodology of D. Reynolds et al., 2023 and Gerber et al., 2018, elevation data from ASTER Global Digital Elevation Model V002 and Corine land use data were used (Agency, 2006; Spacesystems & Team, 2019), with atmospheric forcing data coming from the COSMO1E model (www.cosmo-model.org). One caveat to the setup of this study which differs from the setup used in D. Reynolds et al., 2023 is the lack of vertical velocity data from COSMO1 during our simulation period. To generate the diagnostic wind field HICAR requires some initial estimate of the 3D wind field. It then computes a final wind field by eliminating divergence in the wind field while minimizing the difference between the initial and final wind fields. Without an input of vertical velocity from COSMO1, an initial vertical velocity field of 0 is passed to the diagnostic wind solver. The underlying assumption here is that one solution for the vertical velocity field which eliminates divergence would be the vertical velocity field used by COSMO1. If there is no bias in the initial guess (using a wind field of 0) then the solution which minimizes changes to the initial 3d wind field should favor a solution close to the original COSMO1 vertical velocity.

Starting with forcing data from the 1.1 km horizontal resolution COSMO1E model, nested HICAR simulations were performed at horizontal resolutions of 1km, 250 m, 100 m, and 50 m. The blue square shows the final domain used for the 50 m simulations in Figure 3.1. Static data and forcing variables used from COSMO1E follow the methodology outlined in D. Reynolds et al., 2023. 1km simulation HICAR runs were run from October 1st 2021 to May 10th 2022, in order to spin up the seasonal snowpack present during the observational campaign. The higher resolution simulations performed for the period of the campaign were then initialized with the snow cover of their parent domain. The high-resolution 50 m simulations were run from April 25th to May 10th. HICAR uses the NoahMP land surface scheme to parameterize land-surface processes (Niu et al., 2011), the YSU PBL scheme, and the RRTMG radiation scheme. Starting at the 250 m resolution simulation, the parameterization of terrain-induced sheltering introduced in D. Reynolds et al., 2023 is used. This scheme uses a 3D version of the S_x parameter (Winstral & Marks, 2002) to reduce wind speeds in the lee of prominent terrain features. The effects of this parameterization on the near-surface flow field are investigated in Section 3.3.3. Lastly, the PBL scheme is turned on for all simulations, even down to a horizontal resolution of 50 m. PBL schemes are commonly turned off for atmospheric modeling setups in the gray zone (Chow et al., 2019), or a scale-aware scheme is used (Shin & Hong, 2015). These steps are done because the atmospheric model is assumed to resolve some of the turbulent eddies at these scales, and so parameterized mixing in the form of a PBL scheme should

Table 3.1: Differences between model setups tested

Run	Microphysics Scheme	Thermal Winds (°C)
HICAR_ISH_Therm	ISHMAEL	Yes
HICAR_ISH	ISHMAEL	No
HICAR_Mor_Therm	Morrison	Yes

not "double-count" this turbulence. Because HICAR does not consider momentum in its solution of a wind field, it is not known how much turbulent motion the model does resolve. As will be discussed in Section 3.3.4, HICAR does not appear to resolve turbulent motion driven by vertical wind shear and buoyancy. For this reason, the YSU PBL scheme remains active for model runs at all resolutions. To test the impact of different model settings on simulations of air temperature and winds, three different model setups were performed: one run using the Morrison microphysics scheme (Morrison et al., 2009) and the thermal wind parameterization, HICAR_Mor_Therm, a run using the ISHMAEL microphysics scheme and the thermal wind parameterization, HICAR_ISH_Therm, and lastly a run with the ISHMAEL microphysics scheme and no thermal wind parameterization, HICAR_ISH. These different modeling strategies are only compared in Table 3.2 and Figure 3.10. At all other points in the paper, the HICAR_ISH_Therm run is used and referred to simply as "HICAR".

3.3 Model Evaluation

3.3.1 Point Comparisons

Comparisons of 2 m air temperature, wind speed, and wind direction as measured at the AWSs SMN_DAV1 and WFJ and as modeled by HICAR are shown in figure 3.3 from April 28nd to May 10th. As seen in figure 3.1, SMN_DAV1 is located on the valley bottom, while WFJ is located roughly 1000 m above near a mountain peak. The three IMIS stations do not have ventilated temperature sensors, so only periods with wind speeds greater than 1.5 m/s are used in computing these statistics, assuming that this allows for some passive ventilation (Erell et al., 2005). These conditions of higher wind speeds tend to occur during the day, especially at the lower elevation stations that experience valley winds. Thus, when comparing against the IMIS stations, our comparison is biased toward mid day periods.

From the statistics of air temperature presented in Table 3.2 it is clear that the performance of HICAR depends on the microphysics scheme used. The Morrison microphysics scheme produces the highest positive mean bias error (MBE) of any of the model runs, with a MBE of 0.8°C across all AWSs in the modeling domain, and an MBE of 1.34°C at the ventilated SMN stations. At SMN stations, the ISHMAEL runs all show slight cold biases. These results suggest that the Morrison microphysics scheme results in slightly too warm of temperatures with our modeling setup. The cold biases of the ISHMAEL schemes may be attributable to the strong surface-atmosphere decoupling shown in figure 3.3 which leads to very cold temperatures

Chapter 3. Intermediate Complexity Atmospheric Modeling: Is it Right?

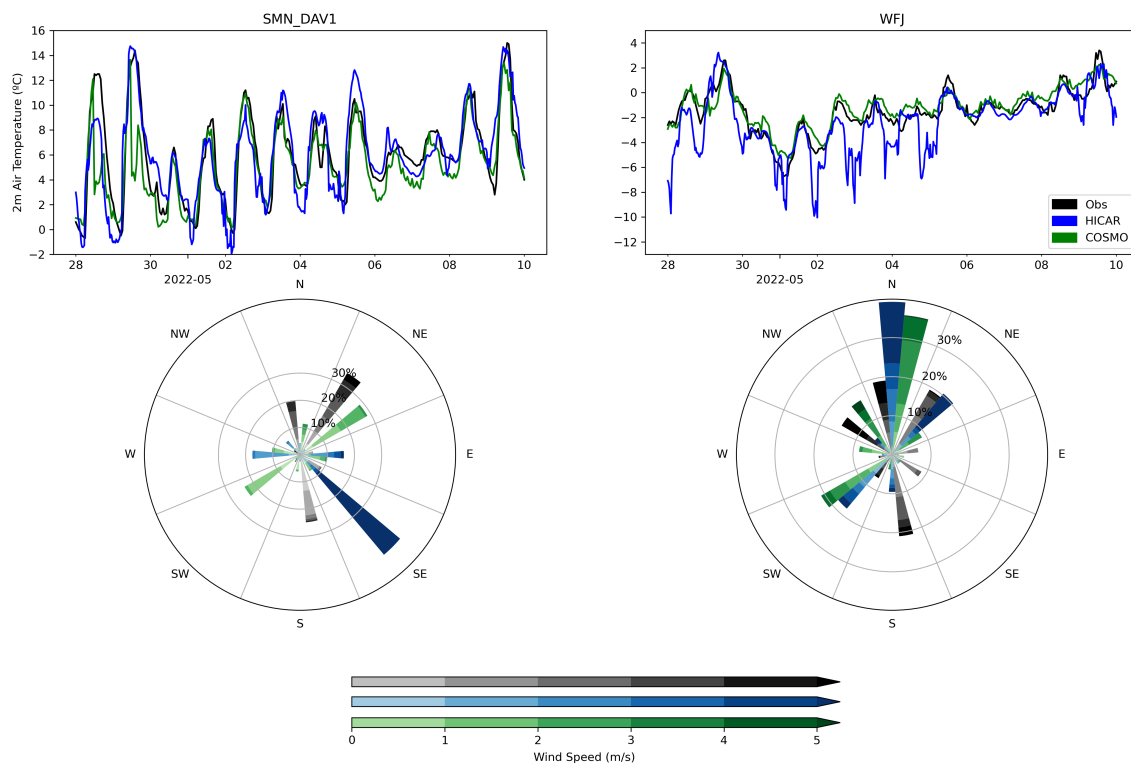


Figure 3.3: Comparisons of observations, the HICAR model, and the COSMO 1.1km resolution model used to force the HICAR model. The upper plots show 2 m air temperature in °C from the two SMN stations. The lower plots show wind roses at the two sites calculated from observations of wind at 10 m height above ground. The data are grouped according to cardinal direction such that each data source can be compared with the others. The weight of the color indicates the wind speed, and the distance along the radial axis indicates the frequency of occurrence. As a reanalysis product, we stress that COSMO output data here has assimilated the SMN data in a post-processing step.

over snow on calm, clear nights. We thus expect that solving for these low biases would change the results such that the HICAR run with the Morrison microphysics scheme would no longer have the lowest MBE. The best results in RMSE are obtained once the thermal wind parameterization is switched on with the ISHMAEL microphysics scheme, yielding an RMSE of 1.97°C across all stations. This score is an improvement over the RMSE of the COSMO1 data (1.99°C), and the same run improves the MBE as well (-0.91°C for HICAR, -1.24°C for COSMO1), demonstrating HICAR’s added value as a downscaling scheme. For this reason, the rest of the analysis uses only the HICAR simulation with the ISHMAEL microphysics scheme and thermal winds.

Of note is the difference in performance when using all stations or simply the two SMN stations. As noted above, statistics including the IMIS stations are biased toward daytime measurements. At the high elevation station (WFJ) where a snow cover is present, HICAR displays excessive

night time cooling during clear nights. Thus, biasing the period of observations towards daytime measurements benefits HICAR in this metric. Still, we include both sets of statistics, as using all stations increases the number of observations available for comparison. Additionally, the COSMO data has been assimilated to the SMN stations but not the IMIS stations, so this second group of AWSs is necessary.

When comparing the wind patterns at the valley site, the observations show strong winds coming from the up-valley direction (NE), and winds distributed roughly evenly along the up- and down-slope directions (N and S). The 1km COSMO data simulates winds channeled along the valley axis (NE, SW), with overall lower wind speeds than the observations. HICAR shifts the distribution of the COSMO winds toward the up- and down-slope directions, unfortunately effectively removing any signal of channeled valley winds in the process. However, the wind speeds predicted by HICAR are higher than those of COSMO, and more inline with the observations. These findings suggest that the thermal wind parameterization, as implemented, results in excessive deflection of the input winds in the slope direction. At the WFJ site, winds are predominately affected by synoptic conditions, and thus little thermal flow signal is seen. Overall, the HICAR wind directions remain close to the wind directions predicted by COSMO. As observed at the valley site, however, wind speeds from HICAR are increased when compared to COSMO, better matching observations.

The differences in 2 m air temperature at the WFJ site are worth further discussion because of the dependency on radiative forcing that they highlight. In Figure 3.4 we observe that before sunset on April 30th, HICAR simulated cloudier conditions than observed. This is shown by the higher incoming longwave (LW) radiation and less outgoing shortwave (SW) radiation compared to observations. As a result, HICAR had higher temperatures than observations during this period (Figure 3.3). The opposite situation can be observed during the next night on May 2nd. HICAR simulates much colder temperatures than observed due to underestimating cloud cover. These results show a strong dependency of 2 m air temperature on the radiative forcing terms calculated by the RRTMG radiation scheme. It is possible that this strong dependency is compounded by underestimating turbulent fluxes during clear nights when stable conditions persist over the snow cover. This would result in excessive cooling of the near-surface layer. Previous studies using snow models have observed similar excessive nocturnal cooling of the snowpack, and suggest limiting the lower bound of the exchange coefficient under such stable conditions (Lafaysse et al., 2017; Martin & Lejeune, 1998; Mott et al., 2023). In a future study, we will explore the representation of snow-atmosphere interactions in more sophisticated snowpack models to improve this potential shortcoming.

Table 3.2: Statistics of the 2 m air temperature estimates of various model runs as compared to observations. The X_{SMN} columns are values computed against the SMN stations, where ventilated temperature sensors are used. The IMIS stations are included as well in the X_{IMIS} and X_{All} columns to allow for more points of comparison. For the IMIS stations, times where wind speeds are less than 1.5 m/s are not considered in the analysis under the assumption that moderate wind speeds are enough to passively ventilate the sensors. The best score in each category is bolded.

Run	RMSE _{SMN} (°C)	MBE _{SMN} (°C)	RMSE _{IMIS} (°C)	MBE _{IMIS} (°C)	RMSE _{All} (°C)	MBE _{All} (°C)
COSMO	1.46	-0.22	2.38	-1.91	1.99	-1.24
HICAR_ISH_Therm	1.84	-0.39	2.05	-1.26	1.97	-0.91
HICAR_ISH	1.98	-0.60	2.20	-1.41	2.22	-1.09
HICAR_Mor_Therm	2.67	1.34	2.28	0.44	2.44	0.80

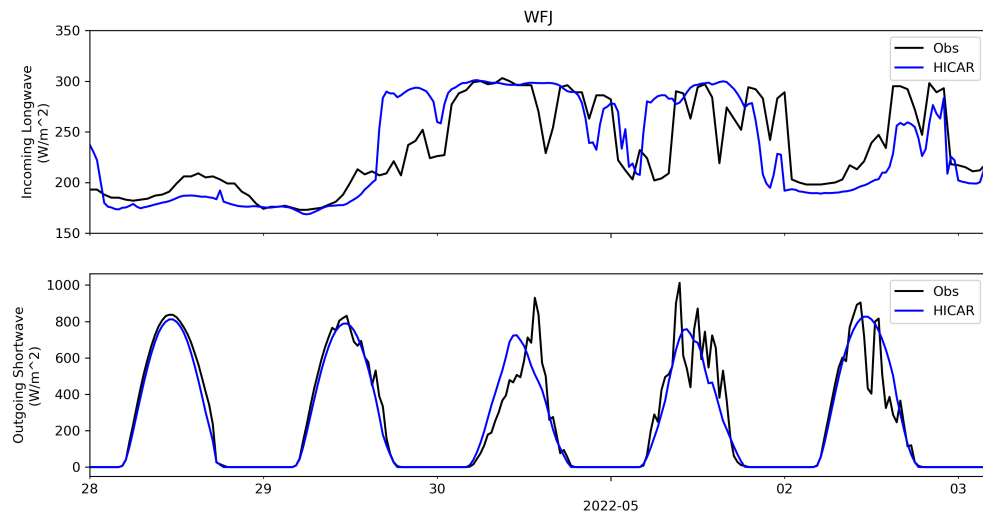


Figure 3.4: Observations of incoming longwave and outgoing shortwave at the WFJ SMN station compared to results from the HICAR model over a 5 day period. The choice of these variables was limited to the observations available at the WFJ station. The first two days have little cloud cover, as evident by the amount of incoming longwave, followed a period of intermittent cloudiness over the final 3 days. In the lower panel, the solid blue line indicates outgoing shortwave radiation as forecasted by HICAR, while the dashed blue line indicates outgoing shortwave radiation calculated using a constant surface albedo (α) of 0.8.

3.3.2 Ridge Crest Wind Patterns

To investigate HICAR's representation of spatial patterns of winds over exposed ridge crests, we employ the RHE scans introduced in Section 3.2.1. Figure 3.5 gives an example of an RHE scan. The bottom right panel shows the difference between scan elevation and terrain elevation. The upper right panel shows modeled wind vectors from HICAR overlaid on the terrain. Black arrows show the flow field in the first model level, while gray arrows show the flow field in the second model level. It is already apparent that the thermal wind parameterization is highly localized to the first model level, and this point will be discussed later in section 3.3.5. When comparing the terrain map in the upper right panel with the scan elevation difference in the bottom right, we see that the scan elevation is closest to the terrain over local terrain maxima. This approach maximizes our sampling of areas where terrain-induced speedup may be observed. The wind LiDAR scan shown in the bottom left panel indicates high radial velocities towards the LiDAR over Weissfluhgipfel in the bottom left corner of the panel. The general near-surface wind direction over the peak, as simulated by HICAR, runs mostly perpendicular to the axis of the RHI scans, indicated by the dashed black line. Radial velocities simulated by the HICAR model are shown in the upper left panel. These radial velocities are calculated from the 3D HICAR wind field by projecting the wind vector at each point along the scan vector from the wind LiDAR. The HICAR model simulates the high wind speeds over

Weissfluhgipfel observed in the LiDAR data but overestimates the local reduction in wind speeds observed just south of the wind LiDAR location in the midslopes of Weissfluhgipfel. Using the modeled streamlines shown in the upper right panel, we can interpret this region of low radial velocities as being due to flow deflection around the ridge of Weissfluhgipfel. The scan elevation plot indicates that this region of the scan was slightly above the surface, so the synthetic RHE scan generated from the HICAR data is rather sampling the simulated flow field above the surface. The deflection simulated results in wind directions perpendicular to the LiDAR location, thus yielding near-0 radial velocities. Although the model overestimates this reduction, its ability to simulate the presence of such a fine-scale feature could still be considered a success of the model. Moving to the east of the Figure, wind speeds along the ridge crest containing Parsennfurgga can be examined. Here, we see good agreement between observed and modeled radial velocities, including predictions of radial velocity direction around the south-eastern axis of the RHI scan where the sign of radial velocity changes. Figure 3.10 shows a flow field as simulated by HICAR just a few days prior over Parsennfurgga. In the top panel, channelling of the synoptic scale winds through Parsennfurgga, and the associated speed up, are resolved by the model. Over the summit of Schwarzhorn (the peak in the lower right of the figure), we do note that HICAR under predicts wind speeds, although the LiDAR data also suggest a local minimum in radial velocities over the peak compared to mid-slope wind speeds. Lastly, Figure 3.5 indicates that the synoptic-scale flow near the surface was oriented more westerly than HICAR predicts. This is evidenced by the line along which the sign of the radial velocity changes. Judging from the LiDAR data, it is observed to be slightly more horizontal than the line of sign reversal seen in the HICAR data, which roughly follows the axis of the RHI scan. This difference is likely due to the COSMO1 forcing data, which greatly confines the synoptic scale winds of the HICAR simulation. The dependency of the HICAR model on accurate forcing data results in an inability to correct for inaccurate input wind direction, although the difference between model and observations appears to only be on the order of $\approx 15^\circ$. Taken together, we see that the HICAR model greatly relies on the input data used, but can add significant fine-scale detail to the simulated wind field, including regions of flow speed up, reduction, channeling, and deflection.

3.3.3 Leaside Structures

As outlined in D. Reynolds et al., 2023, HICAR features a parameterization for lee-side separation when the bulk Richardson number near the surface is below a critical threshold. The positioning of the wind LiDAR was chosen to scan into the leaside of a mountain ridge to validate this flow parameterization. Figure 3.6 shows the results of an RHI scan from the wind LiDAR for a time in the early morning of May 2nd. The scan shows flow moving from the east to the west over the Parsennfurgga. In these RHI figures, the perspective is that of a viewer standing north of the LiDAR and looking toward the south in Figure 3.1. As the flow encounters the ridge crest on the left, it seems to separate the lower-level airflow from the upper-level flow, creating an eddy-like structure on the lee side where we observe a reversal in the flow direction. This disturbance propagates downwind, with the flow reversal extending farther downwind

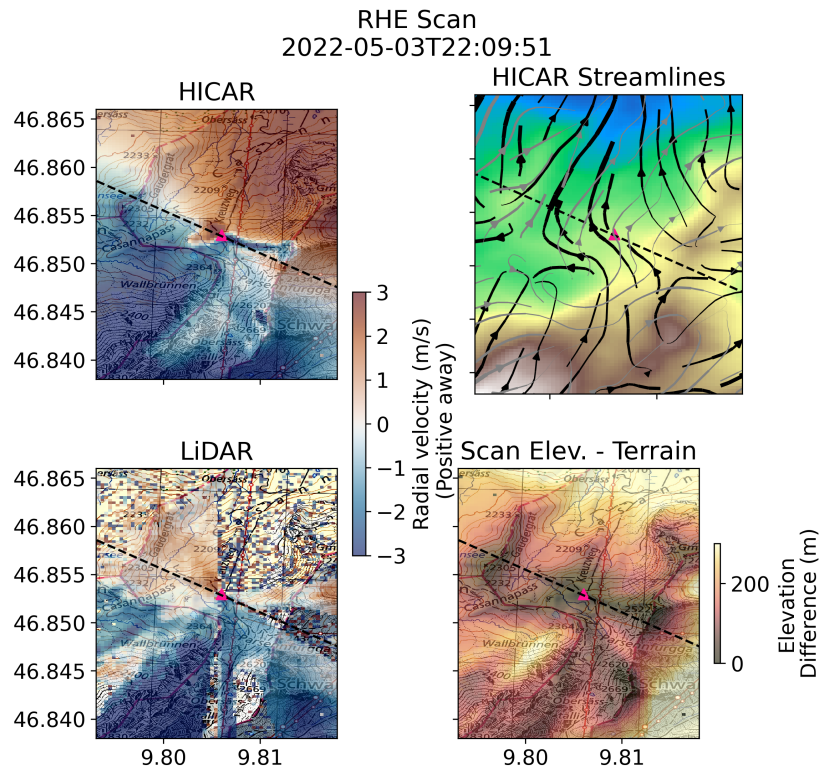


Figure 3.5: Demonstration of a Reynolds-Haugeneder Elevation (RHE) scan. The bottom right panel shows the difference in scan elevation relative to terrain elevation, with darker areas indicating scan locations closer to the surface. Radial velocities relative to the LiDAR location (pink triangle) are shown in the left panels, with the bottom panel showing data from the LiDAR scan and the upper panel output from the HICAR model. The dashed black line shows the orientation of the RHE scans discussed in later sections. The upper right panel shows modeled flow lines in the first model level in black, and flow lines in the second model level in gray.

than the location of the wind LiDAR. Weak wind speeds not exceeding $\approx 1\text{ m/s}$ are observed in this flow separation region. The results from HICAR accurately predict the occurrence of this eddy-like structure. The wind speeds within this region are also in approximate agreement with the observations from the LiDAR. The lateral extent of the eddy-like structure is different in the HICAR model as compared to observations. In HICAR, the parameterization for eddy extent relies on a user parameter for maximum extent and the bulk Richardson number in the lee side (D. Reynolds et al., 2023). Figure 3.6 indicates that the maximum extent of the lee side parameterization, which was set at 600 m in these simulations, may be limiting the growth of longer regions of flow recirculation. This highlights the promise of the existing parameterization for capturing non-local flow dynamics, but also the need for focused testing of the parameterization assumptions and functional relationships between terrain descriptors

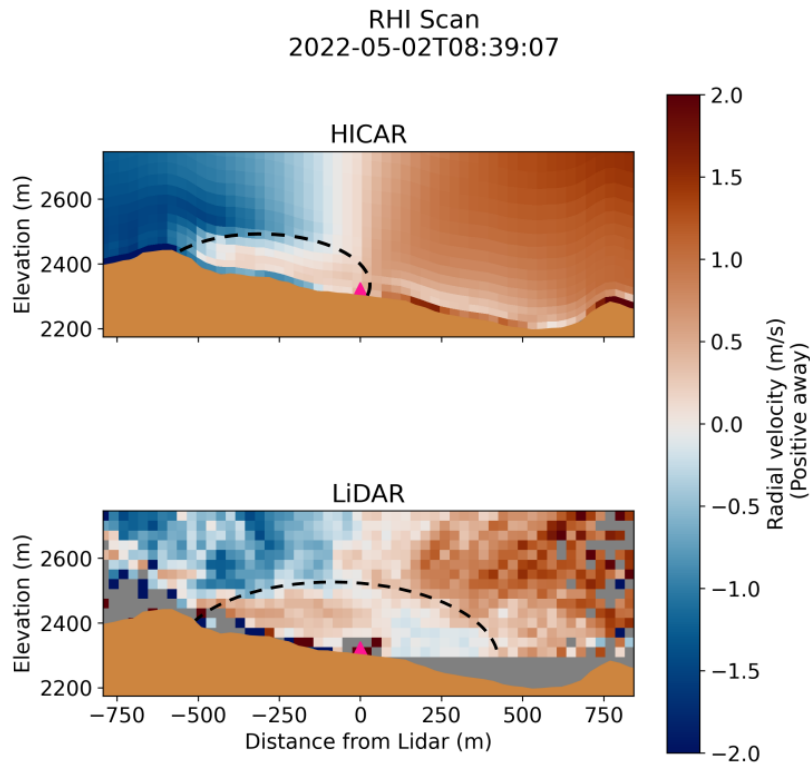


Figure 3.6: Radial velocities computed from the HICAR model relative to the position of the wind LiDAR (pink triangle), compared to observations of radial velocity from the LiDAR itself. Flow from the left to the right (east to west) over Parsennfurrga is seen to induce an area of recirculation behind the ridge. The approximate region of recirculation is marked with the dashed black line in both panels.

and flow modification.

3.3.4 Turbulent Flow Features

An important distinction of the HICAR model is its lack of a mass and momentum-based solution to the wind field. This is one of the core advantages of the model in terms of computational speed, but also results in an expected under-performance for turbulent flows. Figure 3.7 illustrates such a scenario. The wind LiDAR observed easterly flow over the Gaudergrat around midday on May 4th, generating regions of alternating flow direction within the first 500 m above the surface. HICAR, however, simulates only one radial flow reversal as a function of height. This is likely produced by the leeside parameterization (Section 3.3.3), as both areas of flow reversal occur in the lees of Parsennfurrga and Gaudergrat. Additionally, radial velocities of greater magnitude exist closer to the surface, due to either 1) the thermal flow parameterization, or 2) a rotation of the wind direction as a function of height. Since using

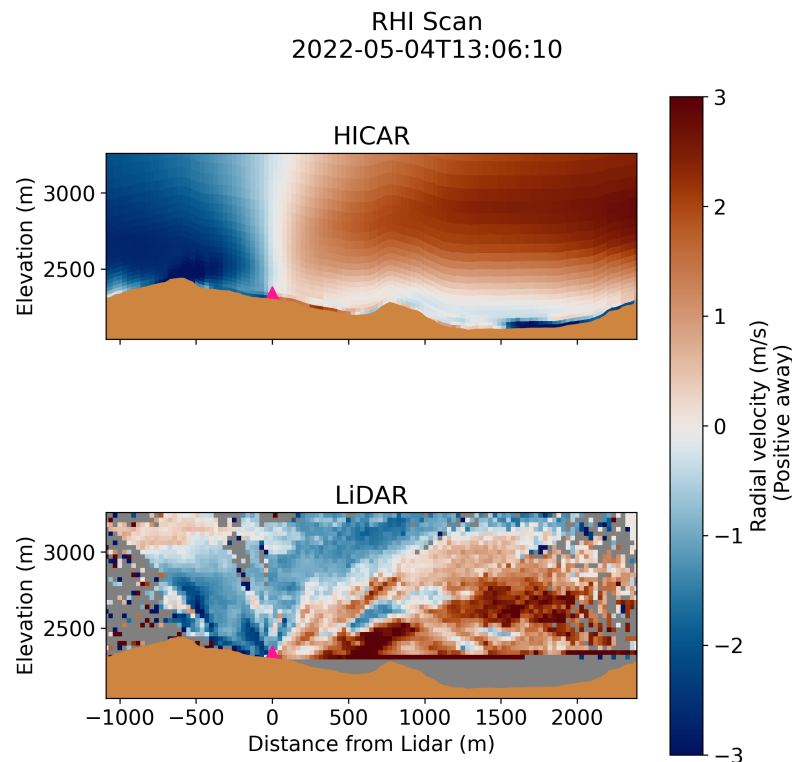


Figure 3.7: Radial velocities computed from the HICAR model relative to the position of the wind LiDAR (pink triangle), compared to observations of radial velocity from the LiDAR itself. Flow from the left to the right (east to west) over Gaudergratt creates turbulent structures which extend roughly 500 m aloft. The HICAR model simulates flow reversal relative to the wind LiDAR near the surface, but fails to capture any turbulent motions as observed.

a single wind LiDAR restricts us to comparisons of radial velocity, apparent flow reversal or increases in radial velocity in the RHI figures may be due to subtle rotations of the wind vectors towards or away from the LiDAR (best illustrated by consulting 3.5). Taken together, we can see that HICAR simulates unstable near-surface conditions, as evident by the activation of the leeside flow parameterization, and strong vertical shear near the surface. In reality, these combined factors should produce the turbulent near-surface flow observed by the wind LiDAR, but HICAR lacks any ability to consider vertical shear or buoyancy-driven turbulence in its flow modifications. This instance demonstrates HICAR's inability to simulate turbulent flow under all atmospheric conditions.

3.3.5 Thermal Flows

The model changes to HICAR, as detailed in Section 3.2.2, all seek to improve the model's representation of the surface energy balance. Implementing a terrain-shading radiation

Chapter 3. Intermediate Complexity Atmospheric Modeling: Is it Right?

Shortwave Radiation and Sensible Heat Flux

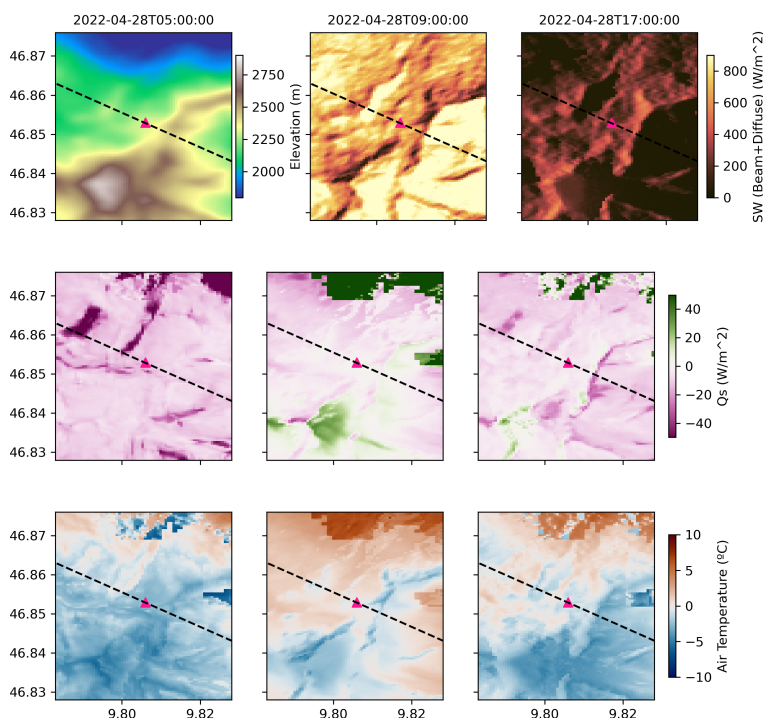


Figure 3.8: Downwelling shortwave radiation, sensible heat fluxes, and 2 m air temperature as modeled by HICAR from the pre-dawn hours on April 28th until 17:00 UTC. The upper left panel shows the orography over the region of interest. No plot of shortwave is shown for 5:00 UTC, as the sun was still below the horizon. The location of the wind LiDAR and orientation of the RHI transect are shown by the pink triangle and dashed black line, respectively.

parameterization and the direct coupling of RRTMG’s direct and diffuse shortwave radiation fields with the NoahMP land surface model are the main improvements contributing to this change in simulating surface energy fluxes. In the following discussion, positive sensible heat fluxes (Q_s) corresponds to an upward heat flux, and negative Q_s to a downward heat flux. The results of the model changes detailed earlier is indirectly on display in Figure 3.3, where the 2 m air temperature shows a clear diurnal signal and the effects of cloud cover. Figure 3.8 shows the heterogeneity in total modeled downwelling shortwave radiation throughout a day, centered on the deployed wind LiDAR (Figure 3.1). The differences in modeled shortwave radiation between the two daytime periods show the effects on radiative input induced by the complex terrain surrounding our site.

This heterogeneity is also reflected in the maps of sensible heat flux. For the map at 9:00 UTC,

high-elevation areas receiving more solar radiation generally experience a positive sensible heat flux as the snow cover over the domain heats up to 0°C. This is because the 2 m air temperature at these higher elevation areas is still below freezing at 9:00 UTC, resulting in a positive sensible heat flux. The sharp transition in sensible heat fluxes in the upper region of the figure is due to a transition from snow-covered, low-vegetation land surface types to forested model grid cells. NoahMP allows low-vegetation land surface types such as brush to become partly buried under snow, changing the surface albedo and exchange coefficients over such grid cells in comparison to forested grid cells. At 17:00 UTC, the pattern in sensible heat fluxes at high elevation areas is roughly reversed as the solar elevation angle swings across the sky, and the terrain shading parameterization captures the resultant effects on slope-scale shortwave irradiance. The high-elevation areas also experience more negative sensible heat fluxes at 17:00 UTC, as the overlaying air temperature is now above 0°C at the end of the clear, sunny day. For the map at the pre-dawn hour of 5:00 UTC, the pattern of sensible heat flux is seen to vary primarily with air temperature, with exposed areas tending to have sensible heat fluxes of greater magnitude due to stronger wind speeds driving greater surface energy exchange. These results for Figure 3.8 demonstrate the model's ability to simulate heterogeneous patterns of surface energy fluxes.

Section 3.3.1 demonstrated the model's ability to simulate downwelling radiative terms of the surface energy balance accurately. These terms are the driving forces behind the simulated 2 m air temperatures presented in Figure 3.3 and Table 3.2, which showed agreement with observations. We thus conclude that patterns of sensible heat fluxes shown in Figure 3.8 are reasonable, and now focus on the parameterization of thermally driven slope flows, which depend on these sensible heat fluxes.

The parameterization of slope flows follows the methodology outlined in Section 3.2.2. Figure 3.9 displays an RHI scan done in the early morning of May 3rd when little cloud cover was present and the snow-covered surface was able to cool due to longwave radiation. The LiDAR observations from this time show a thin layer of downslope flow moving toward the LiDAR from Parsennfurgga, and a reduction in wind speeds downwind from the LiDAR when compared to flow aloft. Lastly, flow away from the LiDAR is observed just over the crest of Gaudergrat. These observations suggest the presence of low-level slope flows down from Parsennfurgga, which entrain overlaying flow, slowing down the westerly flow aloft. Results from the HICAR model during this time show similar phenomena, with slope flows dominating the near-surface flow structure during this time. The primary difference between observations and HICAR is the difference in the vertical extent of the slope flows. Such strong vertical shear should induce turbulence, mixing up this near-surface layer. This would both lower the near-surface wind speeds, and distribute their influence vertically. HICAR's approach to solving for the 3D wind field does not currently consider this process, and thus the strong vertical shear remains. One potential solution would be to modify the parameterization proposed by Grisogono et al., 2015 to smooth the correction to the wind field when shear is present. A broader picture is made available by Figure 3.10, illustrating the effect that this parameterization has on surface flows. The top panel shows wind speeds and direction at the 10 m height for a simulation

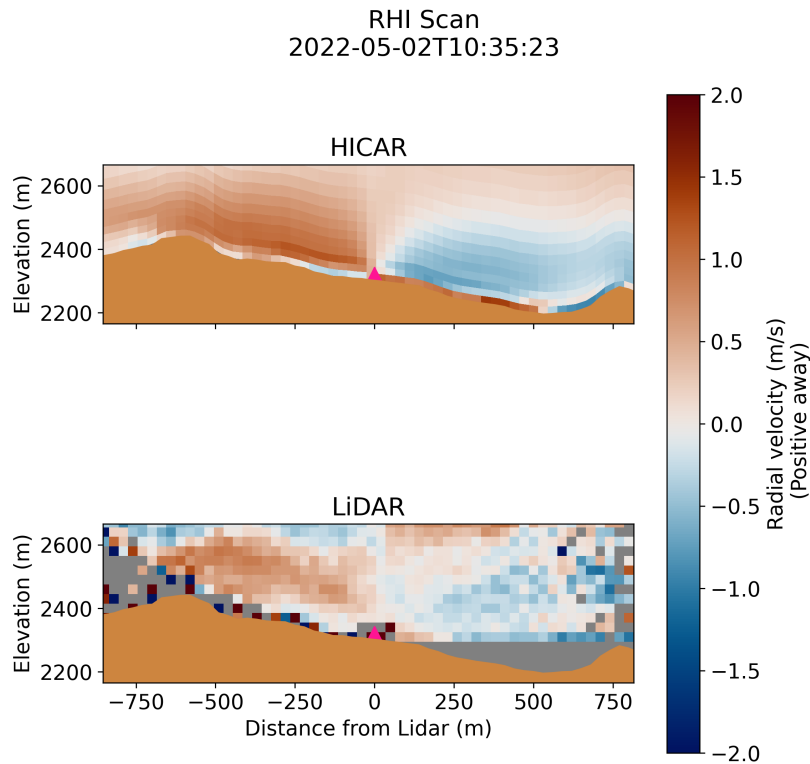


Figure 3.9: Radial velocities computed from the HICAR model relative to the position of the wind LiDAR (pink triangle), compared to observations of radial velocity from the LiDAR itself. Flow from the right to the left (west to east) is undercut by downslope flows running down from Parsennfurga and entraining air aloft.

run without the slope flow parameterization, while the bottom panel shows the same model output from a simulation run with the slope flow parameterization. The two primary effects of the parameterization appear to be both an increase in wind speeds along the downslope direction as well as a rotation of the mid-slope wind vectors to point more downslope. As a result, this effectively inhibits up-valley flow from spilling over the sub-ridge in the middle of Figure 3.10. During daytime hours over this late-season snow cover, air parcels from lower elevations tend to be heated due to their starting position over snow-free ground. The presence of balancing, katabatic flows produced by the snow cover is crucial to block the impingement of these warmer flows. Thus, the sort of lower-elevation flow-blocking displayed in figure 3.10 is expected to be a necessary component of simulating late-season snow covers. As seen in figure 3.3, the surface winds also reach higher speeds with the use of the thermal wind parameterization. The wind roses of the earlier figure suggest that the speed up shown in figure 3.10 may be excessive.

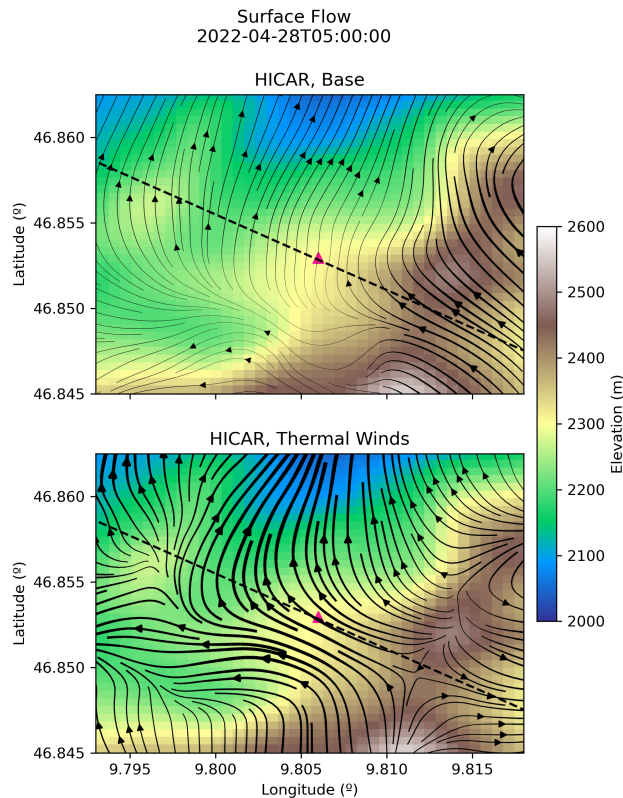


Figure 3.10: A comparison of modeled flow lines at 10 m height above ground for a 50 m resolution HICAR simulation without the thermal wind parameterization (top panel) and one with the parameterization (bottom panel). Thickness of the flow lines corresponds to wind speed, with thicker lines indicating higher wind speeds. For a time in the early morning hours over snow cover, the use of the thermal wind parameterization is shown to give stronger downslope flows.

3.4 Conclusions

This study assessed the efficacy of a new intermediate complexity atmospheric model designed for use at hectometer scales in alpine terrain. Three nested simulations were presented, stepping down to a simulation with a target resolution of 50 m run for 14 days. Each individual simulation takes an afternoon to run on a high-performance computing cluster, and consumes roughly 100 node-hours for the 210x213x40 simulation domain. This highly efficient setup allows for comparison of different physics options as done in this study. Such a comparison may be especially useful when used in combination with traditional, compressible atmospheric models.

Using sensors of incoming and outgoing radiation, air temperature, and wind speed, we have evaluated the model at valley bottom and mountain top sites in the late spring. During this time, ephemeral snowpack at high elevations significantly affects the exchange of energy

Chapter 3. Intermediate Complexity Atmospheric Modeling: Is it Right?

between the surface and the atmosphere. The results overall demonstrate the clear added value of the HICAR model in its ability to improve forecasts of variables crucial to land-surface modeling. The findings of this study have particular relevancy to seasonal snowpack modeling, where forecasts of snowpack depend heavily on the surface energy balance, driven by downwelling radiation and air temperature, and accumulation processes influenced by winds and precipitation (Mott et al., 2023). Using measurements at several sites, we have found that using an adaptive-habit microphysics scheme improves the representation of 2 m air temperature while allowing for reasonable predictions of surface input radiation as affected by cloud cover. Additionally, the use of the thermal wind parameterization of Grisogono et al., 2015 improved simulated 2 m air temperature by allowing for improved near-surface ventilation during periods of surface radiative cooling. The mean bias error between one 50 m resolution HICAR simulation and 5 temperature sensors over a roughly 2-week period was found to be 0.18°C, compared to a mean bias error of -1.24°C for the driving model.

A spatial evaluation of the wind fields simulated by HICAR was conducted using data from a wind LiDAR deployed in complex, snow-covered terrain. A new type of LiDAR scan pattern, RHE scans, was also introduced and detailed, allowing maximum sampling of near-surface winds in complex terrain. The LiDAR device measured eddy-like structures in the leeside of terrain features and low-level thermally driven slope flows over the course of its 16-day deployment. Simulations with the HICAR model display similar features, demonstrating that the model can represent the presence and timing of such flow features. These interactions between terrain and flow are the primary drivers of flow field variability at these scales, and represent large modifications to the forcing wind field supplied by the 1.1km COSMO data. Turbulent flow features were also observed by the wind LiDAR which HICAR can not represent. This is due to the lack of any consideration of momentum in the model's solution of a 3D wind field.

Despite advantages for simulating 2 m air temperature when using the thermal wind parameterization, its use produced strong vertical gradients in wind speed. In reality, such strong vertical shear should produce mechanical mixing which allows for a transfer of momentum to higher altitudes. HICAR does not consider momentum, however, and so this shear remains in the wind field. Comparison of HICAR's wind field at a valley station also showed that the thermal wind parameterization shifted the dominate flow regime from a mix of valley and slope flows to favoring almost exclusively slope flows. Both points indicate that the thermal flow correction is likely overestimated in the model, and requires some correction. An effect of vertical shear dampening could be approximated by modifying the thermal wind parameterization to apply a smoother correction.

Lastly, a large negative model bias in 2 m air temperature was observed over snow during clear nights. Due to the timing of this bias, and its presence in simulations both with and without the thermal wind parameterization we suspect that it is caused by overly inefficient exchange between the snow and atmosphere under stable conditions. As noted earlier, the snow modeling community has identified that current exchange parameterizations often

produce excessively stable conditions over snow and result in excessive cooling of the snow surface (Martin & Lejeune, 1998; Schlögl et al., 2017). These shortcomings may be overcome by coupling HICAR to a more physically rigorous snowpack model, which will be explored in a future study. Coupling HICAR with land surface models may prove to be mutually beneficial, as these models would themselves benefit from high resolution atmospheric forcing data. Such a demonstration of a two-way coupled HICAR-snowpack model would prove the use of the model for applications where dynamic downscaling has long been attractive but remained technically prohibitive.

Code and Data Availability HICAR can be used for non-profit purposes under the GPLv3 license (<http://www.gnu.org/licenses/gpl-3.0.html>, last access: 1 February 2023). Code for the model is available at <https://github.com/HICAR-Model/HICAR>. The exact release (v1.2) used in this publication is available at <https://doi.org/10.5281/zenodo.10679307>. Data from the IMIS stations are available at <https://measurement-data.slf.ch/>, data from the SMN stations are available at <https://opendata.swiss/en/dataset/automatische-meteorologische-bodenmessstationen>, and data from the Wind LiDAR observations are available at 10.16904/en-vidat.481. Output from the COSMO1 model was obtained through MeteoSwiss. The basemap layer used in Figure 3.1 comes from Swiss Topo. Similarly, topographic data for generating the RHE schematic and designing the scans was obtained from Swiss Topo swissALTI3d (<https://www.swisstopo.admin.ch/de/hoehenmodell-swissalti3d>).

Acknowledgements The authors thank the funding source of this project, the Swiss National Science Foundation grant #188554. The computational resources needed to perform the simulations were provided by the Swiss National Supercomputing Center (CSCS) through projects s1148 and sm78. The authors would like to thank Mahdi Jafari and Moritz Oberrauch for assisting in the retrieval of the wind LiDAR during challenging, late-season conditions. Fanny Kristianti and Franziska Gerber were also key in providing help and understanding of the Halo Photonics system. Developers of open source python toolboxes, particularly xarray and xesmf, have also played a crucial role in this study by enabling efficient analysis and manipulation of large datasets.

4 Seasonal Snow-Atmosphere Modeling: Let's do it

This chapter corresponds to the version of the article submitted to the journal *The Cryosphere* by the authors:

Dylan Reynolds, Louis Quéno, Mahdi Jafari, Justine Berg, Michael Haugeneder, Michael Lehning, and Rebecca Mott

Abstract

Mountain snowpack forecasting relies on accurate mass and energy input information to the snowpack. For this reason, coupled snow-atmosphere models, which downscale input fields to the snow model using atmospheric physics, have been developed. These coupled models are often limited in the spatial and temporal extent of their use by computational constraints. In addressing this challenge, we introduce HICARsnow, an intermediate-complexity coupled snow-atmosphere model. HICARsnow couples two physics-based models of intermediate complexity to enable basin-scale snow and atmospheric modeling at seasonal time scales. To showcase the efficacy and capability of HICARsnow, we present results from its application to a high-elevation basin in the Swiss Alps. The simulated snow depth is compared throughout the snow season to aerial LiDAR data. The model shows reasonable agreement with observations from peak accumulation through late-season melt-out, representing areas of high snow accumulation due to redistribution processes, as well as melt patterns caused by interactions between radiation and topography. HICARsnow is also found to resolve preferential deposition, with model output suggesting that parameterizations of the process using surface wind fields only may be inappropriate under certain atmospheric conditions. The two-way coupled model also improves surface air temperatures over late-season snow, demonstrating added value for the atmospheric model as well. Differences between observations and model

output during the accumulation season indicate a poor representation of redistribution processes away from exposed ridges and steep terrain, and a low-bias in albedo at high elevations during the ablation season. Overall, HICARsnow shows great promise for applications in operational snow forecasting and studying the representation of snow accumulation and ablation processes.

4.1 Introduction

Patterns in mountainous snowpack are beautifully complex, with sharp cornices contrasted by smooth wind slabs and fresh snow deposits. The process affecting these shapes are equally complicated, comprised mostly of redistribution by wind and preferential deposition for the aforementioned features (Mott et al., 2018). Wind redistribution acts close to exposed ridges and peaks, where winds have sharp discontinuities in wind speed. This sets up net accumulation and ablation by saltation or suspension. Snowfall itself is modified at the ridge scale via preferential deposition, where some areas of a cross-ridge transect receive more snow than others (Lehning et al., 2008; Zängl, 2008). Preferential deposition has been the subject of focused research into what mechanisms lead to such deposition patterns. Initial observational studies found that information about surface winds, either from station data or model simulations, correlated with areas of differential deposition. Lehning et al., 2008 noted the mechanism of updrafts decreasing the net fall speed of snow particles, while downdrafts would do the opposite. This should lead to less deposition in the region of updrafts relative to downdrafts, and their study proposed a parameterization of preferential deposition relating vertical wind speeds to precipitation. Similarly, Dacic et al., 2010; Helbig et al., 2024 found that higher horizontal wind speeds, as well as vertical wind speeds, correlated to regions of differential snow deposition over an alpine glacier. Both of these studies explain preferential deposition as a process dependent on interactions between snow and the near-surface flow field. Mott et al., 2014 challenged this simplified view of the process, observing that interactions between falling snow and cloud microphysics, mainly via the seeder-feeder mechanism, also played a role in preferential deposition. The earlier modeling study of Zängl, 2008 found a similar mechanism to lead to increased deposition on leeward slopes for solid hydrometeors. Importantly, this process is expected to occur at elevations more than 100m above the terrain surface. Mott et al., 2014 also observed that horizontal advection of particles above ridges in the downwind direction played a dominant role in the process of preferential deposition. A modeling study from Gerber et al., 2019 corroborated these observations, noting that differences in modeled snowfall along a cross-ridge transect were existent at elevations above 100m above the terrain surface, suggesting an influence from cloud-microphysical processes. The authors of this study also considered that mean advection aloft may contribute to this signal, where a peak in precipitation is shifted downwind from over the peak in elevation. Due to difficulties in separating these two processes when examining final precipitation amounts, Gerber et al., 2019 considered both processes to contribute to the preferential deposition signal simulated at the 100m above ground level. Notably, the

differences in snowfall at this height explained two-thirds of the surface snowfall differences. Additional modeling by Z. Wang and Huang, 2017 and Comola et al., 2019 supports the conclusion that horizontal advection aloft contributes to preferential deposition. Viewed together, the basic description of preferential deposition arising from particle-flow interactions remains correct. At the same time, the notion that it mainly occurs close to the surface, and is thus a direct result of the surface flow field, is uncertain. The results of Comola et al., 2019 in particular demonstrated that parameterizations of preferential deposition based on surface measurements are valid only under advection-dominated particle motion.

Atmospheric models are often employed to better consider the processes affecting snow depth patterns in the mountains, as done by Gerber et al., 2019. These atmospheric models have also been coupled with snow models in a two-way setup (Sharma et al., 2023; Vionnet et al., 2014; Voordendag, Goger, Prinz, et al., 2023). Two-way coupling of atmospheric models with snow models offers benefits to both models. In this configuration, a better representation of the surface snowpack can lead to better estimates of mass and energy exchanges between the surface and the atmosphere, which then feeds back to the snow model. This has been found to directly improve estimates of near-surface air temperature and blowing snow sublimation rates (Groot Zwaaftink et al., 2013a; Schlögl et al., 2018). The influence of precipitation on seasonal snowpack during the accumulation season has already been discussed, while during the ablation season radiation is the primarily driver of changes to the snowpack (Helbig et al., 2010; Jonas et al., 2020; Mazzotti, Essery, Webster, et al., 2020). Unfortunately, these two processes are computed by the most expensive parts of modern atmospheric models, the radiation and microphysics schemes. Even more troubling, the heterogeneity of mountain snowpack is only resolved at horizontal resolutions approaching the hectometer scale and below (Deems et al., 2006), and this snowpack heterogeneity is precisely what matters for snow hydrological questions (Luce et al., 1998; J. D. Lundquist & Dettinger, 2005). This heterogeneity results from the accumulation processes discussed above, namely preferential deposition and redistribution, as well as fine-scale radiative processes such as shading from cloud cover or terrain. This means that coupled snow-atmosphere models should be run at the hectometer resolution in order to capture hydrologically relevant differences in the snowpack. And, that the two processes which require the most computation time should not be degraded to reduce computational demand.

These conditions have been followed by the earlier studies using coupled snow-atmosphere models in mountainous terrain mentioned above, and as a result these studies have been constrained to simulation periods on the scale of days. This is due to the computational expense of running atmospheric models at such high horizontal resolutions. One exception to this is the usage of snow-atmosphere models over ice sheets, as done by Sharma et al., 2023 with the CRYOWRF model. In this environment the snowpack is found to vary over larger length scales than in mountainous terrain. This is partly due to the lack of terrain obstacles disturbing the wind field, and a homogeneous distribution of snow depth aside from small-scale bedforms (Filhol & Sturm, 2015; Picard et al., 2019). This reduced heterogeneity of snow depth thus permits larger modeling resolutions. Caveat aside, studying the cumulative

impacts of dynamic downscaling on mountain snowpack over an entire snow season requires efficient atmospheric models of intermediate complexity.

The snow modeling community has been adopting this strategy, with numerous studies employing a diagnostic wind solver to generate a wind field for simulating wind-driven redistribution (Groot Zwaaftink et al., 2013a; Quéno et al., 2023; D. S. Reynolds et al., 2021; Vionnet et al., 2021). This efficient approach to generating a 3D wind field can also be implemented within an atmospheric model, as was done in D. Reynolds et al., 2023 when developing the HICAR model. This creates a computationally efficient atmospheric model capable of providing high-resolution precipitation and radiation data, in addition to a surface wind field required by most intermediate-complexity wind-redistribution schemes. The approach was tested in Berg et al., 2024, in prep, with HICAR downscaling COSMO1 data (www.cosmo-model.org) to force the FSM2trans snow model (Quéno et al., 2023). COSMO1 is a non-hydrostatic atmospheric model which was used to produce operational weather forecasts over Switzerland. Using dynamically downscaled data was found to result in more heterogeneous snowpack than using dynamically downscaled winds alone, better matching the distribution of observed snow depth.

These results motivated the development of a two-way coupled snow-atmosphere model using HICAR and FSM2trans, which will be the focus of this study. Section 2 will discuss how these two models are coupled together and which data they share. Section 3 will present results from the two-way coupled model, focusing on accumulation patterns in complex terrain, the representation of preferential deposition in the model, and lastly the melt patterns. All of these results will be compared to observations of snow depth from aerial LiDAR scans. Finally, these results will be summarized in the last section, with recommendations for future applications and model improvements.

4.2 Methods

4.2.1 Model Coupling

To simulate the seasonal snowpack and processes of snow redistribution in a computationally efficient manner HICAR employs the FSM2trans model (Quéno et al., 2023), which consists of the base Factorial Snow Model 2 oshd variant (FSM2oshd) (Essery, 2015; Mazzotti, Essery, Moeser, & Jonas, 2020; Mott et al., 2023) with additional modules for calculating snow redistribution. This snow model can account for snow accumulation and melt processes as well as redistribution of the snowpack through wind-driven and gravitational transport. HICAR and FSM2trans are coupled in a two-way system, where a static library of FSM2trans routines are integrated into HICAR as the snow module. At each call to the land surface model (LSM) in HICAR, the forcing data required to drive FSM2, including 10 m wind speed, 2 m air temperature and relative humidity, incoming shortwave and longwave radiation components, and precipitation, are supplied by HICAR. In return, FSM2 computes changes to the internal

snowpack properties, as well as the sensible heat flux, latent heat flux, and snow surface temperature, which are subsequently utilized by the chain of surface-atmosphere exchange within HICAR. To highlight these model changes and the coupled system's potential for modeling seasonal snow, we refer to the two-way coupled model as HICARsnow in the rest of the study.

Previous validation of HICAR highlighted the need for a more accurate snow model than the one featured in the NoahMP LSM. However, the rest of NoahMP features more rigorous bare-ground and non-snow-covered vegetation dynamics than what is available for non-snow-covered cells in FSM2. To take the best from both LSMs, we run NoahMP at each LSM time step as well. We turn off the internal NoahMP precipitation partitioning when FSM2 is activated, and supply NoahMP with only liquid precipitation from HICAR. When snow falls on a particular grid cell, or if there is already snow on a grid cell, then the results from running FSM2 are used to update that grid cell during a given call to the LSM routines in HICAR. If a cell is snow covered, then FSM2trans simulates its soil physics, while the soil beneath bare cells is handled by NoahMP.

4.2.2 Parallelization of Snow Redistribution

While the original FSM2 snow model only considers local effects of the atmosphere on the snowpack at each grid cell, FSM2trans simulates redistribution, requiring a transfer of information between grid cells. To facilitate this within the parallelization of HICAR, it was necessary to rewrite the redistribution routines used.

Wind-driven redistribution of snow is calculated using the SnowTran-3D scheme (G. E. Liston et al., 2007) in FSM2trans. In this scheme, the saltation flux for the local grid cell are first calculated considering the local wind speed, direction, and the surface properties of the snowpack. We note that this saltation scheme has been known to underestimate saltation fluxes (Doorschot & Lehning, 2002; Melo et al., 2023), but it has given reasonable snow deposition patterns in prior studies employing intermediate-complexity snow transport schemes.

The local saltation flux is then considered by summing the local contribution and the flux at the upwind cell. This step requires the use of non-local information, namely from some upwind grid cell. In the non-parallel SnowTran-3D implementation, the operation is simply performed over the whole model domain at once, moving along each cardinal direction. The domain boundary conditions serve as the upwind flux at the boundary grid cells. However, HICAR parallelizes the domain into a number of discrete images. In the parallel implementation, boundary grid cells on a given image take on the domain boundary condition for the first iteration, and an initial guess for local saltation fluxes is obtained. The saltation flux at the boundary grid cells of a particular image are then exchanged with boundary grid cells on neighboring images in a standard halo exchange. These updated boundary values are then used to re-run the saltation flux calculation on the local images.

The exchange of boundary estimates of saltation fluxes and re-calculation of local fluxes is

then repeated. This approach has been tested with varying numbers of iterations, and an iteration count of 3 was determined to be adequate for computing steady-state fluxes. The methodology is inspired by the approach used in Mower et al., 2023. Once steady-state fluxes are found, net snow transport and changes to the snowpack properties can be calculated. The same approach is used for calculating transport via suspended snow.

For gravitational redistribution, FSM2trans uses a scheme based on Snowslide (Bernhardt & Schulz, 2010). In this scheme, all grid cells are examined in a given call to the gravitational redistribution module, comparing the local snow depth to a "snow holding depth" which varies for each grid cell according to slope. Grid cells with snow above their snow-holding depth shed their snow to down-slope grid cells. These down-slope grid cells are then examined for the same condition, with the process repeated until no grid cell has a snow depth greater than its local snow-holding depth. Quéno et al., 2023 added the additional condition that snow holding depth is reduced when a grid cell was passed snow. In this way, the reduction approximates the effect of static or dynamic frictional coefficients when avalanching snow slides. To parallelize this module, Snowslide is run on each image, and any snow found to be sliding "out of" the image is transferred to the neighboring image. This sequence is repeated an arbitrary number of times to ensure that avalanches are able to run out their full path. Because Snowslide requires a relatively high number of exchanges, and because the exact timing of avalanche release in such a simplified model is not important, the gravitational module is only called once every simulation hour in HICARsnow.

4.2.3 Observational Datasets

This study relies on repeated areal LiDAR surveys of snow depth to validate the snow depth distribution simulated by the HICAR model. In spring of 2017, three areal LiDAR flights were performed over eastern Switzerland, covering the rugged upper Dischma catchment. The scans include a date near the peak accumulation of snow before the onset of wide spread melt (March 20th), a date 11 days later after warm temperatures and clear skies induced melting of the snowpack (March 31st), and a date in the middle of May, where most snow at lower elevations has melted away. For this May flight, late-season storms have also enriched the snowpack at higher elevations. The area enclosed by these repeat LiDAR flights is shown in figure 4.1 by the black lines. Part of the upper Dischma catchment is glaciated, making the extraction of snow depth at these locations difficult. This is because movements of the underlying glacier result in shifts of the snow surface, which would be recorded as changes in snow depth by the LiDAR scan. To avoid comparing the model with observations at these locations, glaciated areas have been masked from the LiDAR data and model results using glacier outlines from the Randal Glacier Inventory 6 (RGI Consortium, 2017).

A previous study using HICAR found that the model exaggerated nighttime cooling of the snow surface, and thus 2m air temperature, in the spring (D. Reynolds et al., 2024, in prep). To compare the ability of previous model versions with HICARsnow, 2m air temperature data

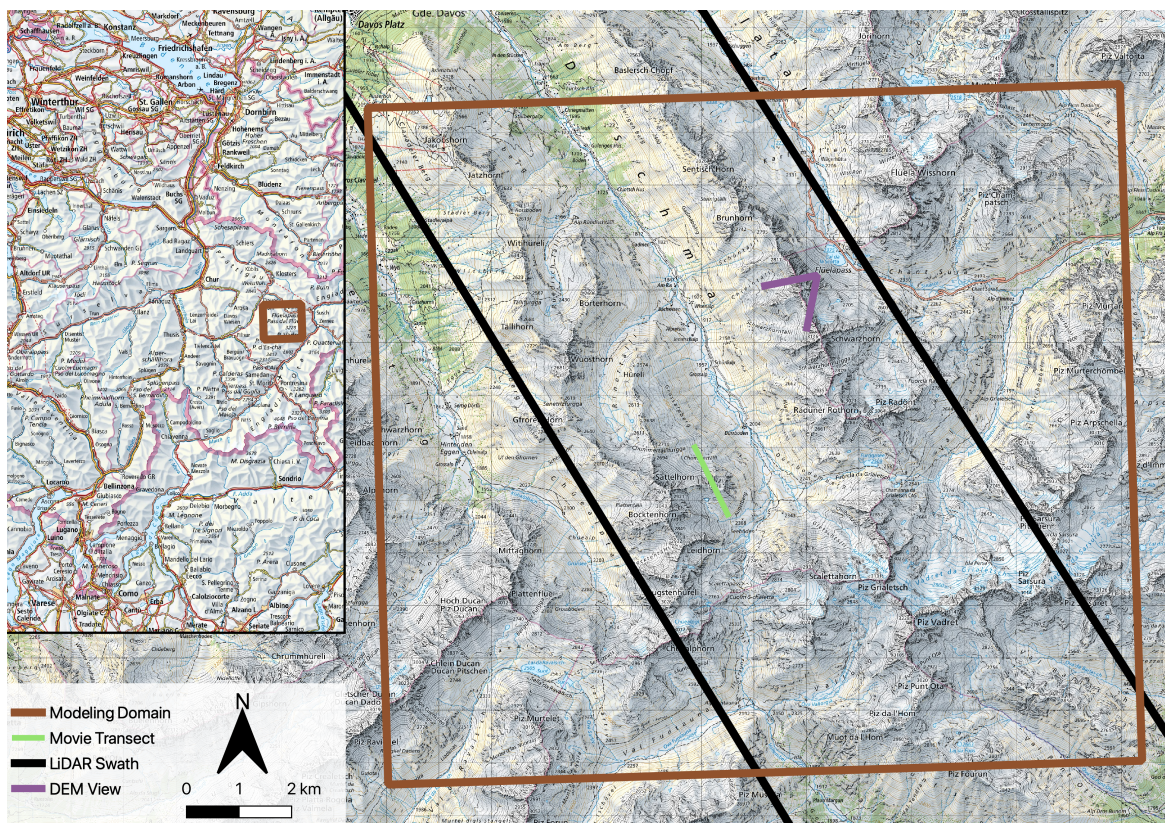


Figure 4.1: Overview of the Upper Dischma Valley outside of Davos, Switzerland. The smaller map in the upper left corner shows the location of the zoomed-in plot within the broader Eastern Swiss Alps. The brown box indicates the modeling domain for the 50m horizontal resolution HICARsnow simulations. The black swath indicates the approximate spatial coverage of the LiDAR data introduced in Section 4.2.3 The green line indicates the location of the transect figures (Figs 4.6, 4.7). Lastly, the purple angle shows the viewing angle for figure 4.8, which compares a 50m and 2m DEM of the region.

from a ventilated temperature sensor used in this prior study is again used here and discussed in section 4.3.2. For a full description of the experimental setup used in this earlier study and the conditions present at this time, we refer the reader to the publication.

4.2.4 Model Setup

To test HICARsnow’s representation of snow accumulation patterns and snow ablation, the model is run from October 1st 2016 through May 17th, 2017 over the upper Dischma catchment outside of Davos, Switzerland (Figure 4.1). The simulations are performed at a 50m horizontal resolution, and are one-way nested within larger 250m and 1000m resolution simulations. Topographic data for constructing the Digital Elevation Models (DEMs) is available from the ASTER Global DEM V002 (Spacesystems & Team, 2019), and land surface data from the Corine dataset is used (Agency, 2006). These static data are then used as input to a domain-generation

script distributed with HICAR, which can produce the remaining necessary topographic data. Output from the COSMO1 model was used for meteorological forcing data, including temperature, pressure, water vapor mixing ratio, and the 3D wind field. This data is used to force the outer 1km domain, after which output from the 1km domain simulation is used to force the 250m simulation, and finally 50m. This setup follows that used by previous studies employing HICAR (D. Reynolds et al., 2023; D. Reynolds et al., 2024, in prep). For the HICAR model, we use version 2.0(TODO: HERE) which features the changes to surface processes detailed in D. Reynolds et al., 2024, in prep. For the FSM2trans model we use the same model parameters used in Berg et al., 2024, in prep. Of note, FSM2trans can be configured with an arbitrary number of snowpack layers. For this study, we configured the model with 6 snow layers, following the methodology of Quéno et al., 2023. One model simulation was performed over the whole time range with the Morrison microphysics scheme (Morrison et al., 2005). A shorter simulation was performed with the ISHMAEL microphysics scheme (Jensen et al., 2017) from October 1st through November 7th 2016 to capture a particular snowfall event. This shorter run was performed due to the nearly doubled model run times when using the ISHMAEL scheme. The ISHMAEL microphysics scheme tracks three forms of ice hydrometeors, or ice "habits", and evolves their density and shape through time to allow for accurate predictions of fall speeds (Harrington et al., 2013a). The scheme belongs to the broader class of Adaptive-habit (AHAB) microphysics schemes (J.-P. Chen & Lamb, 1994), which have not yet been employed in the study of preferential deposition. A discussion of the deposition patterns predicted by the two schemes is given in section 4.3.1.

Lastly, in addition to running the two-coupled HICARsnow model, standalone runs using FSM2trans and various forcing data were performed. Two runs with the FSM2trans model were conducted: one run with statistically downscaled COSMO1 data according to Mott et al., 2023 and only the wind field from HICARsnow, and a second run with all of the forcing data provided by HICARsnow except for precipitation. In this case, precipitation again comes from statistically downscaled COSMO1 data. These two runs are included to demonstrate both the overall impact of dynamic downscaling aside from redistribution, and the effect of dynamically downscaling precipitation alone.

4.3 Results and Discussion

4.3.1 Snow accumulation Processes

Results from running HICARsnow with the Morrison microphysics scheme are shown in figure 4.2, comparing modeled and observed snow depth around peak accumulation. Across the domain, modeled snow depth amounts generally agree with observations, with the valley bottom containing snow depths less than 0.5 m, while higher elevation regions have snow depths near 2 m. Finer scale patterns are also observed in the vicinity of ridges and steep slopes, and these patterns are discussed later in section 4.3.1. Importantly, differences in snow depths exist between the HICARsnow run, and a simulation using FSM2trans with all of the

HICAR forcing data except for precipitation. In this FSM2trans run, we see that there is reduced heterogeneity of snow depth a few hundred meters away from the ridge line compared with the HICARsnow simulation and the LiDAR data. 4.3 shows that HICAR snow better matches observed snow depth values away from the ridge along a transect bisecting this ridge. Moving to the right towards the ridge, snow depth values steadily increase, and this increase persists after crossing the ridge before reducing towards the snow depths from the FSM2trans run. This likely arises from the inclusion of preferential deposition in HICARsnow's precipitation data, and is discussed further in section 4.3.1. From the upper row of figure 4.2 we notice a bias in HICARsnow towards higher snow depths, particularly on the north-eastern facing slopes near the valley bottom. This trend is confirmed when binning snow depths according to aspect and elevation, as done in figure 4.4. Here we note excessively high snow depths along the north-east, east, as well as south-to-west facing slopes. Since this date is near peak accumulation, and little snow melt has occurred until now, we assume that these snow depth patterns are driven by accumulation processes, and not melt processes. The higher snow depths in HICAR at lower elevations may be explained by errors in large-scale precipitation patterns, such as an incorrect rain-snow line earlier in the season, or an overall wet bias in precipitation, as suggested in figure 4.5. We also note more evidence of re-distribution processes, such as avalanching or wind-redistribution, at lower elevations in the LiDAR data than model output. Indeed, HICARsnow mostly represents redistribution processes only in the vicinity of ridges. Section 4.3.1 will discuss the influence of model resolution on this process representation. In the case of SnowTran-3D, wind-redistribution is affected by both forcing data from HICAR and the process representation itself, making it difficult to separate the two as sources of error. At the least, representing redistribution processes at more locations is a clear area of improvement for FSM2trans, as noted by the original study (Quéno et al., 2023).

Chapter 4. Seasonal Snow-Atmosphere Modeling: Let's do it

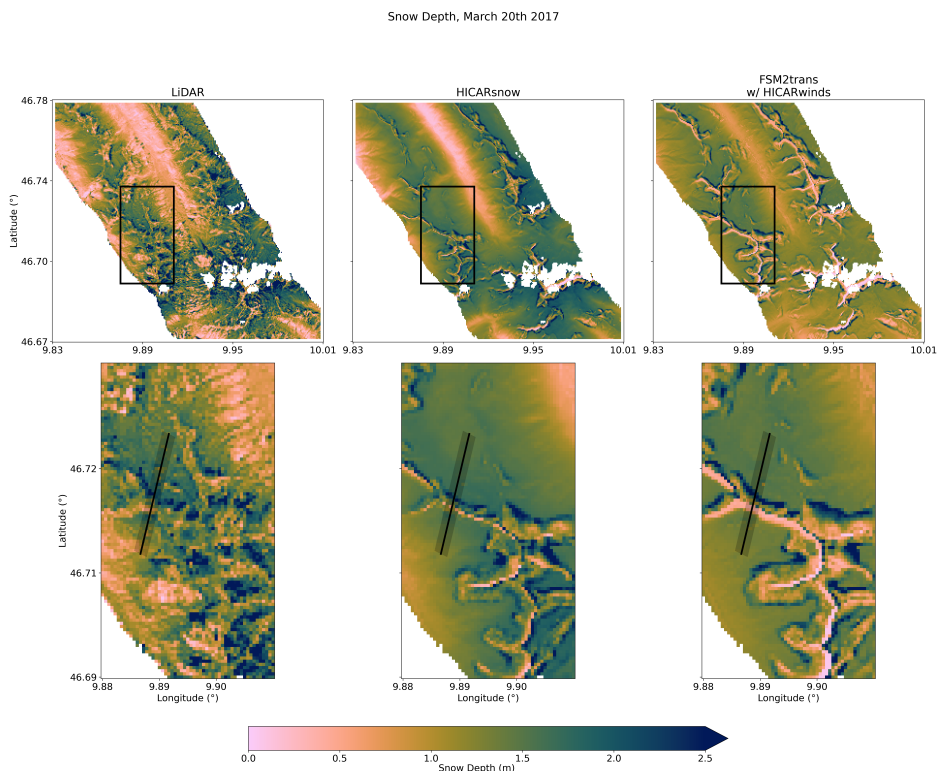


Figure 4.2: Basin-wide comparison of observed snow depth from aerial LiDAR, simulated snow depth from HICARsnow, and simulated snow depth from FSM2trans with all of its forcing data coming from HICAR, except for precipitation. The date is on March 20th, 2017 around peak accumulation of snow. In the lower row, the snow depth around a ridge is shown in detail. The black boxes in the upper row show the location of the detailed view. The model simulations are masked to match the LiDAR flights, where glaciated regions or border cells are removed from the maps.

Figure 4.5 shows the effects of dynamical downscaling on snow depth distributions around peak accumulation. As a baseline, one run is shown where FSM2trans is forced with statistically downscaled output from the COSMO1 model, except for wind input, which comes from HICAR. This was chosen as the baseline to not include effects of redistribution in the comparison. The green line then shows the result from including HICAR forcing data for all other variables, except for precipitation. We note a slight shift to the left, indicating lower snow depths. This may be due a lack of snowfall, as the HICAR temperature field is now used to partition precipitation into rain or snow, or it may be due to more mid-season melt. The greatest shift can be seen when using dynamically downscaled precipitation from HICAR. Here, the distribution is both broader, and has a wider range of values. This result highlights the added value of dynamically downscaling precipitation, where improved gradients in precipitation result in a broader distribution. Interestingly, the 250m HICARsnow simulation, run without redistribution processes, shows a similar improvement in snow depth heterogeneity over this domain. Again, we attribute this to the more heterogeneous precipitation patterns resolved

by HICAR relative to the statistically downscaled precipitation input, even at the 250m scale. Additionally, the HICARsnow simulation at 250m does have a narrower distribution, reflecting the lack of redistribution processes in the simulation.

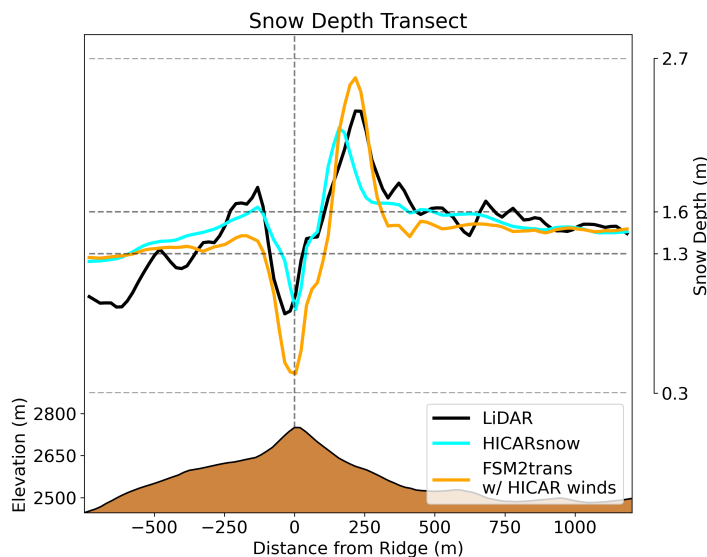


Figure 4.3: Transect of snow depth values, averaged along the transect shown in the cutout of figure 4.2. The direction of the transect is south to north, moving from left to right.

Snowfall processes

During the accumulation season, snowfall processes shape the pattern of snow depth on the ground, either via orographic precipitation or preferential deposition. These two processes are most dominant on smooth, flat terrain in the vicinity of ridges. At these locations, a lack of discontinuities in wind speed driven by terrain features will not lead to net transport via redistribution, flat terrain will not avalanche, and the proximity to ridges confers a signal of preferential deposition. In figure 4.2 we can see such a region in the lower panels, comparing the two sides of the dominant ridge. In the LiDAR data we observe deeper snow deposits on the right side of the ridge compared to the left. This general trend is observed in the HICARsnow results as well, but not in the simulation using FSM2trans without dynamically downscaled precipitation.

To better visualize the process of preferential deposition as simulated by the model, two movies of the process have been made and included in the supplement to this study (placed in the Data Availability Statement for this thesis). Snapshots from two significant moments in the movies are included as figures 4.6 and 4.7 here. Figure 4.6 shows the accumulation of snowfall across a ridge during a particular snowfall event on November 6th, 2016. From this event, we observe a clear difference in snow deposition on the windward side versus the

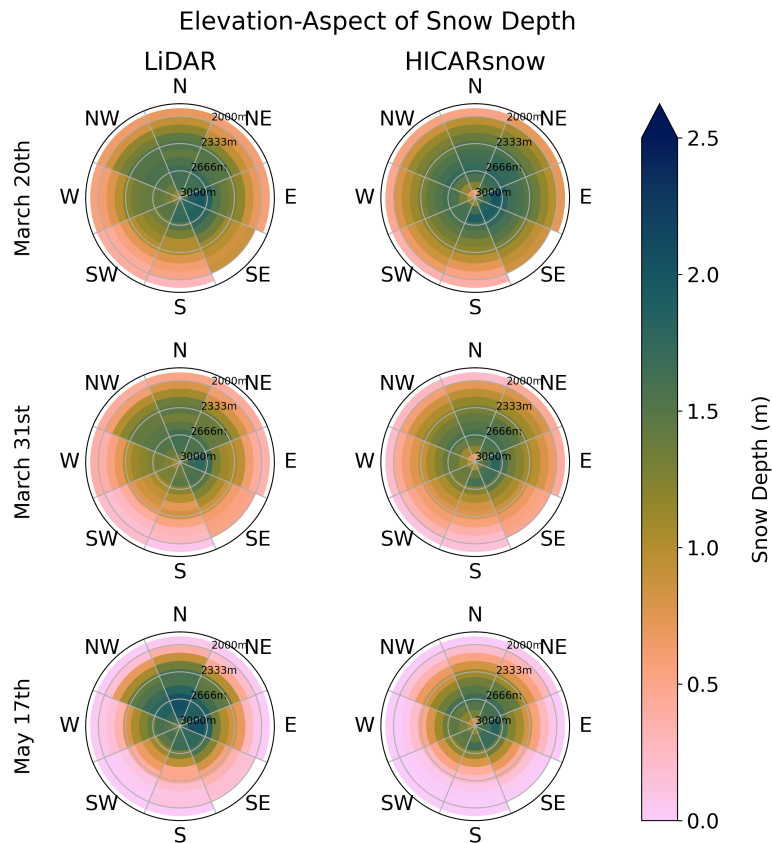


Figure 4.4: Aspect-elevation plots of observed and simulated snow depth above an elevation of 2000m. The data used correspond to the same masked region shown in figure 4.2.

leeward side of the ridge. Stronger winds aloft suggest that the dominant process leading to preferential deposition, in this case, is the advection of snow particles downstream by winds aloft, resulting in a shift of the peak precipitation distribution (Z. Wang & Huang, 2017). Interestingly, the snowfall simulated by the two microphysics schemes is roughly similar, with slightly higher snowfall amounts downwind of the ridge in the ISHMAEL simulation than the Morrison simulation. This difference in snowfall amounts is reflected by the higher concentration of snow particles downwind of the ridge in the ISHMAEL simulation. To better grasp why these differences occur, and how the pattern of preferential deposition develops in the first place, a view of the microphysical parameters during this event is presented in figure 4.7.

Here, the complex processes of microphysical interactions, net advection aloft, and near-surface particle-flow interactions are all on display. The ISHMAEL microphysics scheme can track three ice types, planar, columnar, and aggregate ice, and evolve them separately. Aggregates of ice particles were not present during this event, so they are not shown. The

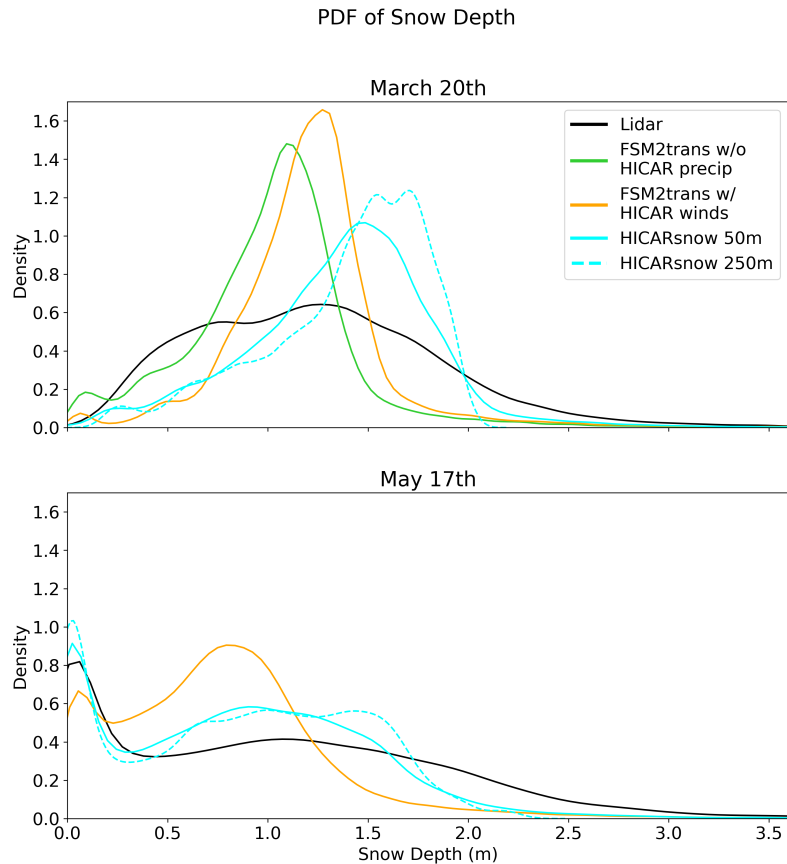


Figure 4.5: Probability Density Functions (PDFs) of observed and simulated snow depth at the times of two LiDAR flights. The orange line shows the results of an FSM2trans run where all of the forcing data comes from statistically downscaled COSMO1 output, except for the winds, which come from HICAR. The green line shows the results of an FSM2trans run where all of the forcing data comes from HICARsnow, except for precipitation, which comes from COSMO1.

Morrison microphysics scheme sorts ice hydrometeors into particular species assumed to have given relationships between particle concentration, mass, and fall speeds. Only snow ice was present in a large concentration for this event. For the initial state shown in figure 4.7, mean advection aloft is shown to act primarily on planar ice, ice1. The bulge in the distribution of ice1 is shifted downwind in the region of strong horizontal winds. Lower in the atmosphere on the leeward side, the distribution of ice1 has a positive trend, suggesting riming of ice1 as it falls towards the surface. The increase in ice1 fall speeds and positive trend in particle density on the leeward side confirm this. Interestingly, the region of increased fall speeds corresponds to the region of columnar ice, ice2. Ice2 is observed to have much lower particle fall speeds, and thus net fall speeds, than ice1, with a distribution concentrated around the leeward side of the hill. This suggests that the feeder cloud in the seeder-feeder process is shifted downwind

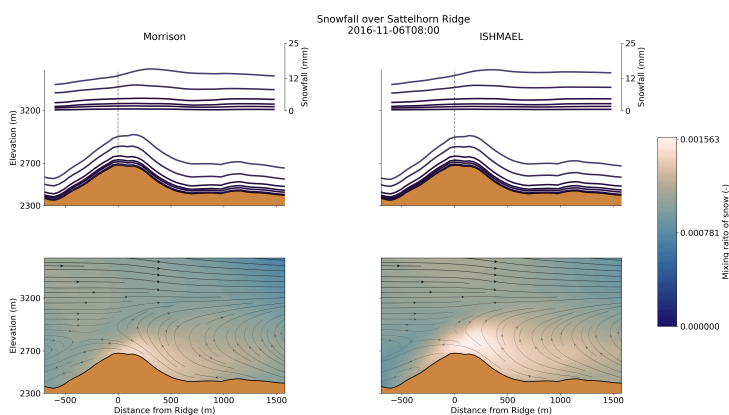


Figure 4.6: Demonstration of preferential deposition during a storm on November 6th, 2016. The location of the transect is shown in figure 4.1, running from the east (left) to the west (right). A vertical dashed line in the upper plot indicates the highest elevation point along the transect. The upper panels show the hourly increase in snowfall (lines in the air) and the hourly increase in snow water equivalent (lines above the terrain) since the beginning of the storm. The lower panels show wind vectors projected along this transect, and the concentration of snow particles in the air. Results using the Morrison microphysics scheme are shown on the left, and the ISHMAEL microphysics scheme is on the right.

of the ridge crest. The cause of this shift is likely a combination of the winds roughly 200 m above the ridge crest, as well as the updrafts present on the leeward side. In this way, we see that cloud-microphysical enhancement via the seeder-feeder mechanism as described by Mott et al., 2014 is also affected by the near-surface flow field. A shifted concentration of snow hydrometeors is also observed for the simulation using the Morrison microphysics scheme, with a bulged distribution of hydrometeors aloft. However, the distribution of particle fall speeds is very homogeneous, indicating that the differences in net fall speed shown by the dashed black contours are mostly due to heterogeneities in the vertical velocity field.

The dynamics of this event are best appreciated by referring to the video in the supplement (placed in the Data Availability Statement for this thesis). Over 30 minutes, the feeder cloud in the lee breaks down, and the local water vapor concentration decreases. As a result, fall speeds of both ice species decrease, and their concentrations decline. This leads to a fall-out of the remaining hydrometeors on the leeward side, signaling the end of this intense period of snowfall. Again, the Morrison microphysics scheme fails to capture these dynamic changes in particle fall speed. It maintains a fairly constant particle fall speed throughout the snowfall event, which has a value similar to the mean fall speed that ISHMAEL predicts for ice1 and ice2 species. The net particle speeds are similar between the Morrison and ISHMAEL simulations, reflecting the importance of the 3D flow field itself in determining sedimentation rates. This similarity likely explains why the deposition patterns shown in figure 4.6 diverge very little. In all, this event was chosen because it highlights the dynamics that can be simulated with HICAR and shows that the Morrison microphysics scheme produces results consistent with a

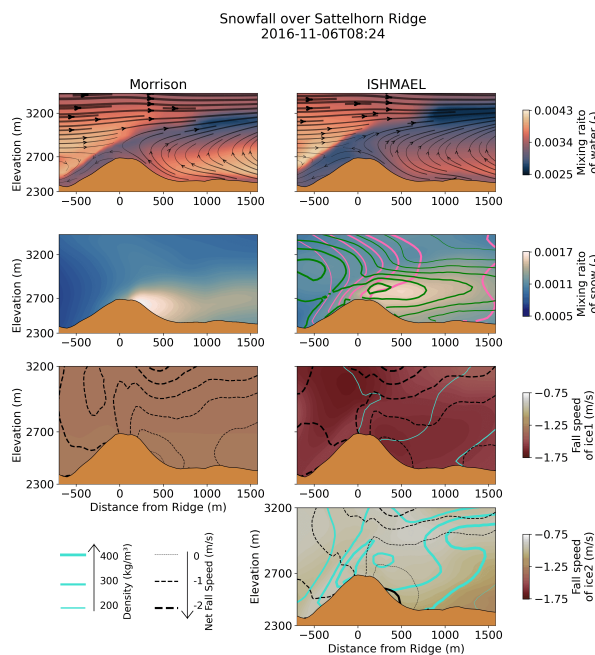


Figure 4.7: The same transect as shown in figure 4.6, but comparing the representation of snowfall in the ISHMAEL and Morrison microphysics schemes. In the upper panels, the wind vectors are overlaid on the water vapor mixing ratio. In the middle panel, the mixing ratio of snow hydrometeors is shown in the background. For the ISHMAEL simulation, the concentrations of ice1 (planar ice; pink) and ice2 (columnar ice; green) are overlaid as contour lines. Thicker lines correspond to higher concentrations. In the lower plots, the ice particles' fall speed are shown as the background shaded color. The hydrometeors' net vertical velocity (vertical air motion - fall speed) is shown with the dashed black lines, where thicker lines indicate faster fall speeds toward the surface. For the ISHMAEL panels, the density of the ice particles is shown by the cyan lines, where thicker lines indicate higher densities. For the ISHMAEL plots, one is shown for the ice1 species, and a second for the ice2 species.

more detailed, adaptive-habit scheme. Importantly, differences in snowfall patterns between the two schemes do exist, particularly over longer time scales and at spatial resolutions larger than the 50m resolution simulations shown here (Jensen et al., 2018). Still, at these spatial scales, the ISHMAEL scheme simulates more complex microphysical interactions, which give rise to solid precipitation patterns in complex terrain. This comparison also demonstrates the utility of adaptive-habit microphysics schemes for studying preferential deposition and in particular showing the influence of different types of hydrometeors.

Of note, downdrafts are present on the windward side of the ridge during this event, while updrafts are present on the leeward side. Figure 4.7 suggests that this is due to eddy-like structures occurring in both valleys which run across the axis of the valley and counter to the mesoscale wind direction. Interestingly, this result contradicts existing parameterizations of preferential deposition based on surface variables (Dadic et al., 2010; Helbig et al., 2024). These

previous study identified regions of near-surface updrafts and downdrafts, and correlated them with areas of decreased or increased snow deposition. In this way, it describes the portion of preferential deposition arising purely from interactions between the near-surface flow and the advection of snow particles. The later studies of Mott et al., 2014 and Gerber et al., 2019 found these particle-flow interactions to be a contributing factor to preferential deposition, but concluded that the interaction between the 3D flow field, snow particles, and cloud microphysics contributed more to preferential deposition of snow.

Synthesizing the results of these studies, we can see that preferential deposition cannot be fully described without knowledge of local cloud microphysical processes and the 3D flow field. This implies that approaches that only utilize 2D near-surface surface fields to parameterize preferential deposition will not capture the dominant effects of a) 3D advection aloft and b) microphysical evolution of snow particles. Earlier models which representing preferential deposition by the advection and diffusion of particles alone will simulate the transport of snow particles (Lehning et al., 2008), but not microphysical processes which may alter their eventual fallout. In the worst case, where local updrafts enhance hydrometeor growth or production, leading to increased fallout, approaches to parameterizing preferential deposition using surface variables will give incorrect results. Since preferential deposition is the dominant process by which precipitation patterns are altered at the hectometer scale, we conclude that dynamic downscaling is necessary to resolve precipitation patterns in complex terrain.

The results of this section demonstrate the complexity of near-surface precipitation processes and the need for dynamic downscaling to capture it. Statistical downscaling is unlikely to capture these precipitation processes which lead to greater variability of snow depths, as shown in figure 4.5. This section has also shown that preferential deposition can occur through interactions between near-surface flow features and microphysical processes. This challenges a dichotomy often invoked when describing preferential deposition (Vionnet et al., 2017), where the two processes shape snowfall distributions independent of each other. Our results suggest that preferential deposition cannot be generally split into two processes, microphysical interactions and near-surface particle-flow interactions, based purely on height above terrain (Gerber et al., 2019).

Redistribution processes

In the direct vicinity of ridges and steep terrain, redistribution processes of wind-redistribution and avalanching play a dominant role in shaping the distribution of snow. Importantly, wind-redistribution often feeds the process of avalanching, loading slopes with snow until the weight of the overlying snow triggers redistribution to lower elevations. In this way, it is difficult to completely disentangle the processes from each other when considering snow depth maps. This is apparent when viewing the cut-out displayed in figure 4.2. Along the ridge line, deep deposits of snow depth are seen to the north of the ridge in the LiDAR data. These deposits may result from wind-loading, avalanching, or a combination of the two. Thus, we will not try to differentiate between the two processes except where obvious and instead focus

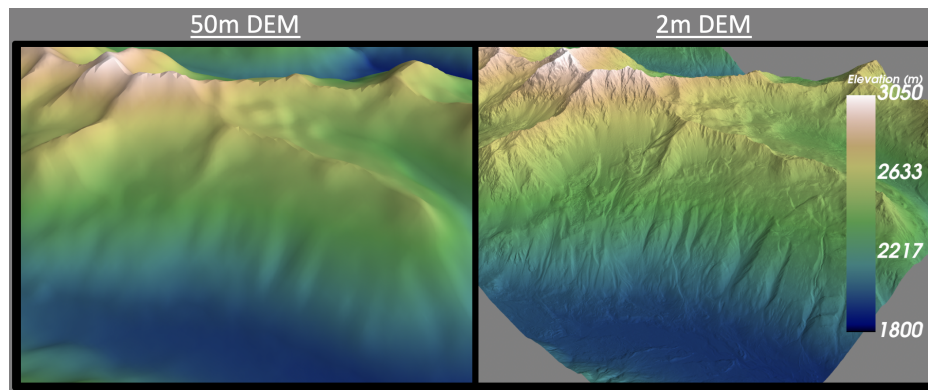


Figure 4.8: Part of the model domain represented using either a 50m or 2m DEM. The view of the camera is indicated in figure 4.1 by the purple angle.

on the strong heterogeneities present in snow depth around steep or exposed terrain.

Overall, HICARsnow shows good agreement with LiDAR data when representing the heterogeneity of snow depth around the ridges. In particular, the approximate areas of deep deposits are captured well (fig. 4.2). This results in a weighting of aspect-dependent snow depths at higher elevations (Fig. 4.4). These observations reflect the findings of Quéno et al., 2023 for FSM2trans in general. Of interest to this study is what patterns of wind-redistribution may say about the wind fields generated by HICAR. One feature of note in the snow depth maps is the lack of wind-redistribution away from prominent terrain features. Figure 4.2 displays this, where the secondary ridge found in the upper center of the cut-out features much more heterogeneity in snow depth in the LiDAR data than in the model output. Again, it is difficult to conclude if this results from insufficient wind transport, or avalanching. A similar pattern is seen in the upper right corner of the cutout, where steep, vegetated gullies in the terrain lead to much greater observed snow depth heterogeneity than modeled. This feature is a clue to why redistribution around secondary ridges is also underrepresented. Both of these terrain features occur over short distances, meaning that they may be poorly represented even in a 50m resolution DEM. Natural disturbances unrelated to the topography (rocks, bushes) should also contribute to increased surface roughness and alter patterns of snow redistribution. The PDF in figure 4.5 shows what effect increased model resolution has on the overall distribution of snow depth, supporting the conclusion that higher model resolutions, or parameterizations which account for sub-grid roughness, may be necessary to resolve snow redistribution in these areas. Figure 4.8 shows the difference between representing the domain at a 50m resolution vs. a 2m resolution. This viscerally demonstrates how sub-grid scale topographic features likely alter the wind field at finer scales (Mott & Lehning, 2010), resulting in different patterns of snow depth even when up-scaling to the 50m resolution.

Wind scour of snow is, however, likely overestimated directly at ridges. Figure 4.2 shows almost 0m of snow depth at some ridge crests throughout the domain, and overall lower snow depth at ridges compared with LiDAR observations. Importantly, many of these areas

of low snow depth are found without corresponding down-slope deposits of snow, ruling out the process of avalanching as a cause of these low snow areas. This excessive scour may be driven by erroneously high wind speeds from HICAR, although a prior study did find reasonable agreement between HICAR's wind speeds and observations at ridge-crests in complex terrain (D. Reynolds et al., 2024, in prep). Thus, the excessive scour at ridges is likely a combination of high wind speeds and errors an overly simplified relationship between wind speeds and transport in SnowTran-3D. Lastly, we note that some deep snow deposits present in the LiDAR data exist further from the ridge line than simulated by HICARsnow. These deposits are likely avalanches that have longer run out paths in reality than simulated. Quéno et al., 2023 did address this with a modification to the Snowslide parameterization as discussed in section 4.2.2, but it may be difficult to accurately represent this process with a simple avalanching model. The issue of model resolution again comes up, where a higher-resolution DEM may represent these slopes at a higher angle, resulting in further run out of the avalanche deposits. Computing wind-redistribution with a snow-physics model capable of resolving the surface microstructure would also make for an interesting comparison to FSM2Trans. Such a snow-physics model is expected to better estimate the threshold friction velocity, which depends upon the surface microstructure of the snow. Coupling HICAR with such models may also be advantageous, since blowing snow model run times are relatively small compared to atmospheric models (Sharma et al., 2023). Overall, the successes and shortcomings of representing snow redistribution with FSM2trans are in agreement with those of Quéno et al., 2023. We refer the reader to this publication for a more detailed investigation of the redistribution processes simulated by FSM2trans.

4.3.2 Ablation Processes

Later in the snow season, air temperature and incident solar radiation begin to shape the spatial patterns of snow depth inherited from the accumulation season. The LiDAR data for March 31st in figure 4.4 shows how lower elevations have already begun to experience melt out by this date in the season. Due to the short temporal difference between these two march flights, and the lack of any precipitation event, the two flights are compared in below to examine HICARsnow's representation of melt patterns. Despite being named the "ablation season", late-season snowfall events can and do occur, as happened between the March 31st and May 17th LiDAR flight. For this reason, the later two flights are not compared for the sake of examining melt patterns. Instead, this flight can be used to test the model's representation of snow depth patterns under a complex situation of melt-out and springtime mixed precipitation events. The PDF of snow depth for May 17th shows good agreement between model output and observations for very small snow depths 4.5. These snow depths occur at lower elevations and on southerly slopes at this point in the season, showing that HICARsnow can capture the snow line well compared to observations. This is reflected in figure 4.4, where the snow line is found to be within 100m of observations across all aspects. The distribution of snow depths shown in the PDF is close to observations for higher snow depths, but lacks snow depths greater than 160cm when compared to observations. Figure

4.4 shows that these snow depths occur at higher elevations, and are absent in the model output. The following paragraph discusses an observed melt bias at higher elevations, which we believe explains this difference in snow depths at higher elevations so late in the season. A prior study comparing HICAR output to observed 2m air temperature also found a slight warm bias when using the Morrison microphysics scheme compared to the ISHMAEL microphysics scheme. A low bias in high-elevation albedo, combined with a slight warm bias, could explain this excessive melt. Thus, future studies using HICARsnow may want to explore using the ISHMAEL microphysics scheme for simulations during the ablation season. The late-season dry bias at high elevations could also be due to a lack of precipitation, but we have previously noted a slight wet bias in the model results around peak accumulation, and the highest elevations in the domain all experienced solid precipitation events up until May 17th. Thus, we conclude that a bias in the amount of precipitation or phase of precipitation is an unlikely explanation for the dry bias at high elevations on May 17th. Lastly, the 250m resolution HICARsnow simulation shows remarkable similarity to the 50m HICARsnow simulation. This reflects the fact that melt processes largely control the snow depth distribution at this point in the season. Since terrain-dependent radiation parameters such as shading and sky-view fraction are still included at the 250m simulations, most of this variability in melt patterns is captured even at the 250m resolution.

To visualize the magnitude and spatial distribution of melt processes simulated by HICARsnow, we compare the difference in snow depth from March 20th to March 31st to the observed difference. During this period of March, sunny conditions lead to widespread melt, as observed in the LiDAR data (fig. 4.9). In particular, snow depth changes occurred mostly at elevations below 2400m, while snow depth patterns above this elevation remained relatively unchanged 4.4. The maps of change in snow depth also show that southern-facing aspects experienced more melt than northern facing aspects, with this general pattern observed in the model output as well. In particular, smaller scale terrain features, such as the gullies present in the upper right corner of the cutout in figure 4.9, show the same pattern of melt as the LiDAR flight. This highlights HICARsnow's ability to simulate slope-scale differences in radiation, thanks in part to the use of terrain-shading factors calculated using the HORAYZON model (Steger et al., 2022).

While HICARsnow captures the overall pattern and slope-scale differences in snow depth change, the model tends to overestimate melt on south facing slopes, especially at middle elevations. One potential explanation for this is lower albedos predicted by the FSM2oshd model. The albedo scheme used here is a prognostic one, which differs from the scheme used for the operational snow forecast over Switzerland (Cluzet et al., 2024; Mott et al., 2023). The operational scheme was specifically developed to increase snow albedos at higher elevations. This option was not used for the current study, because it was assumed that changing the rest of the model forcing data would invalidate the methodology used to tune the operational albedo parameterization. Nonetheless, the identification of too low albedos at high elevations in previous studies supports the hypothesis here that melt on southern aspects is exaggerated due to errors in the snow albedo. Observations from the LiDAR flights also show a larger decrease

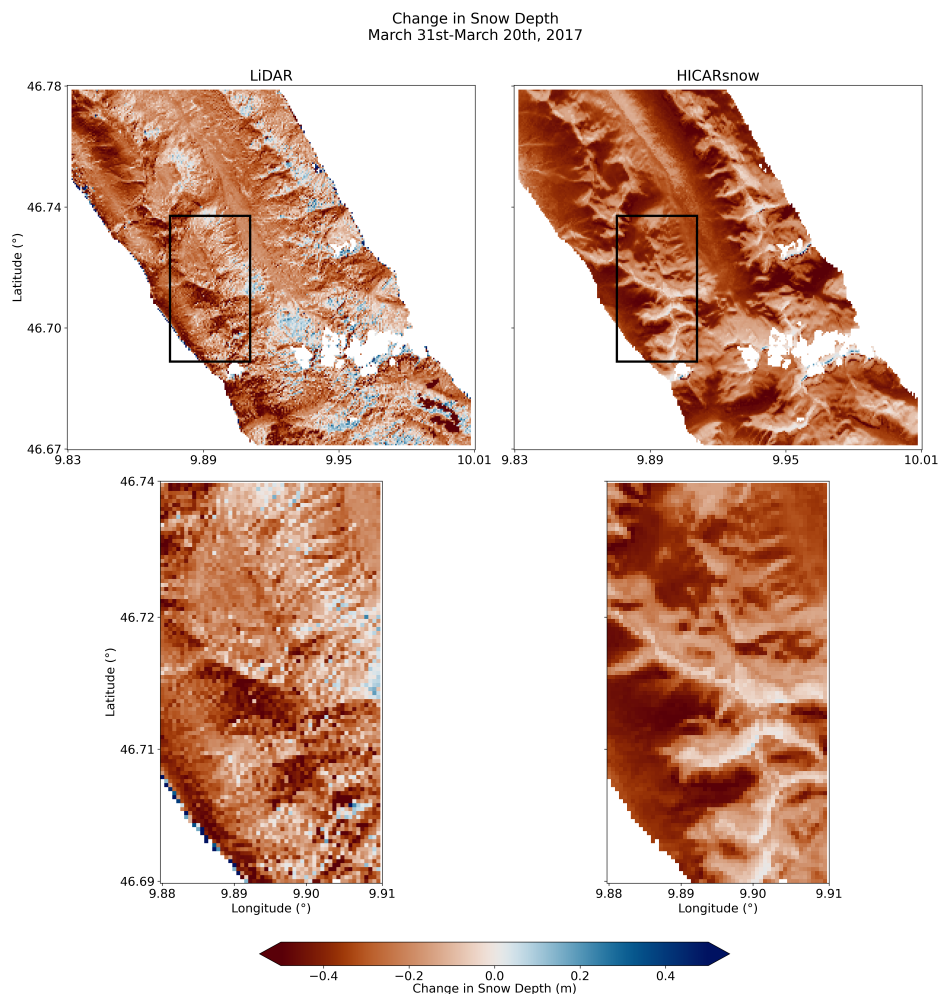


Figure 4.9: Maps of snow difference patterns between the two LiDAR flights at the end of March, comparing LiDAR and HICARsnow. Red colors indicate a loss of snow depth from March 20th to March 31st.

in snow depth on south facing slopes relative to northern facing slopes. Solar radiation is an obvious explanation for this difference. Still, the snow difference maps in figure 4.9 show that redistribution of snow onto north-facing aspects has also enriched snow depths in these locations. Thus, when comparing the same aspects from the HICARsnow simulation, we can conclude that excessively low snow depths on high-elevation, north facing slopes on March 31st result from a lack of redistribution onto these slopes.

4.3.3 Snow-Atmosphere Interactions

Near Surface Air Temperatures

During the ablation season, temperature, wind, and radiative input dominate the energy input to temperate mountain snow cover. An earlier study comparing HICAR simulations over

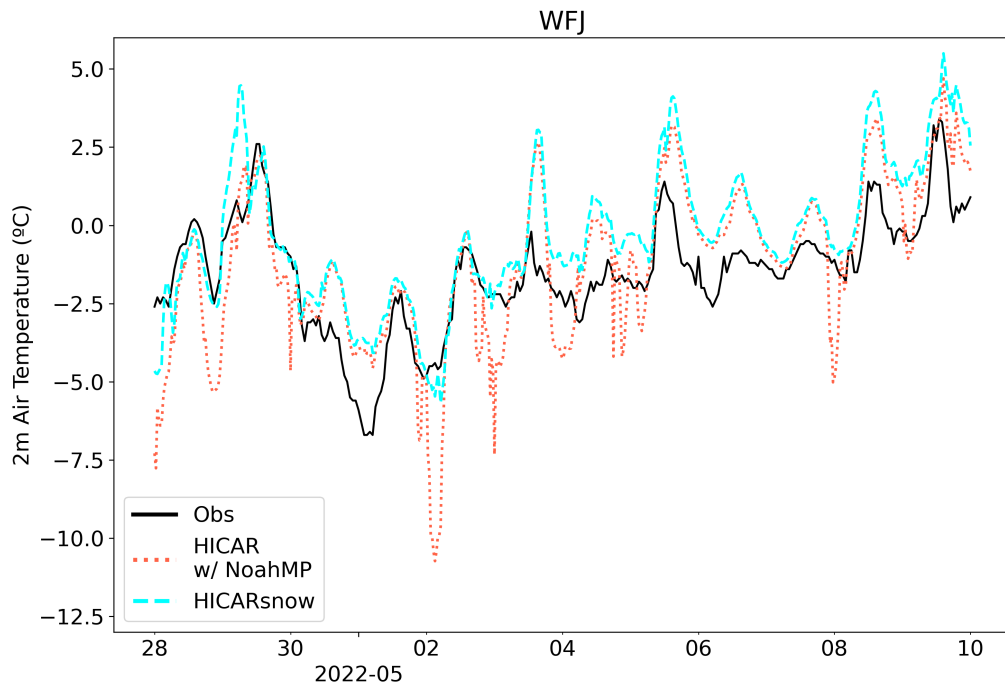


Figure 4.10: Comparison of 2m air temperature from HICAR simulations with observations over a snow covered area in late April 2022. The cyan line shows the results from a simulation with HICARsnow, while the salmon line shows the results from a simulation where HICAR uses the snow model from NoahMP. This figure is a partial reproduction of Figure 3.3 from D. Reynolds et al., 2024, in prep.

spring snow cover found that the model had a large negative 2m air temperature bias during calm, clear nights (D. Reynolds et al., 2024, in prep). This error was interpreted to be due to strong radiative cooling of the snowpack. During these calm, stable conditions, excessively low exchange thermal coefficients are calculated by the NoahMP LSM in HICAR, and thus an uncoupling of the snowpack temperature from the atmosphere develops. This process has been documented and remedied in other snow modeling studies (Lafaysse et al., 2017; Mott et al., 2023), and the mechanism of excessively low predicted exchange coefficients has been observed experimentally (Martin & Lejeune, 1998). Thus, one expectation of coupling HICAR with FSM2 is improving surface air temperatures during such conditions. To test this, we compare the previous results of D. Reynolds et al., 2024, in prep with a run using HICARsnow for their same modeling setup in figure 4.10. The strong departure from observed temperatures during the night is gone when using the HICARsnow model, and there is little change in daytime temperature peaks. This result suggests that HICARsnow can represent diurnal temperature changes during the ablation season, and demonstrates the importance of simulating snow processes for atmospheric models.

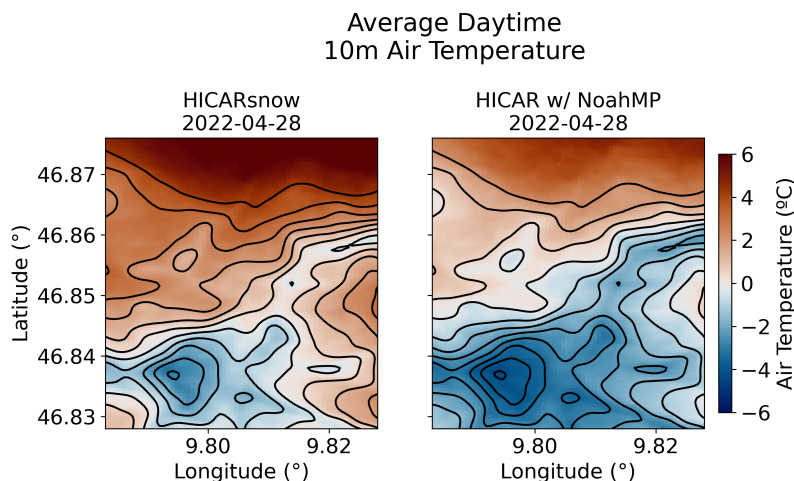


Figure 4.11: Comparison of mean daytime air temperature in the first atmospheric model level for a simulation with HICARsnow, and simulation where HICAR uses the snow model from NoahMP. This covers the same domain and dates as D. Reynolds et al., 2024, in prep. Black contour lines are shown to represent the topography.

A knock-on effect of this excessive nocturnal cooling is found in figure 4.11. Here, air temperatures in the first model level of HICAR (10m above surface) are shown for just a couple hours after sunrise. We note that the air temperature over snow at higher elevations is comparable between the HICARsnow simulation and the simulation where HICAR uses the snow model from NoahMP, albeit with slightly warmer air temperatures in HICARsnow. At lower elevations, however, there are distinct differences between the two simulations, with the HICAR + NoahMP run producing colder temperatures down slope. This effect is likely due to the excessive cooling of the snowpack at night producing colder air temperatures across a larger area. Thus, the excessive radiative cooling at night results in lower air temperatures which persist after sunrise, likely producing less melt in the HICAR + NoahMP simulation.

Blowing Snow Sublimation

Lastly, we can consider the effects of coupling the blowing snow module of FSM2trans, SnowTran-3D, with the HICAR model. Blowing snow, especially via suspension, brings snow crystals into increased contact with the atmosphere where it is possible for them to directly sublimate. If the atmosphere is dry, more sublimation of snow crystals occurs. As sublimation of blowing snow occurs, the surrounding air becomes moist, reducing the efficiency of blowing snow sublimation. This effect has been shown to lead to reduced blowing snow sublimation at the basin scale in alpine catchments (Groot Zwaafink et al., 2013a) and has been documented to completely change surface energy exchange (Sigmund et al., 2022). While studies employing SnowTran-3D have noted basin-wide sublimation rates of 4% of solid precipitation (Bernhardt

et al., 2012; Sexstone et al., 2018; Strasser et al., 2008), the study by Groot Zwaafink et al., 2013a found a value of only 0.1% when blowing snow sublimation was coupled to the atmosphere. To test this effect on SnowTran-3D, we similarly computed sublimation rates as a percentage of total snowfall over the entire modeling domain shown in figure 4.1. As a result, we find blowing snow to result in just 0.35% mass loss relative to snowfall. In contrast, using just the winds from HICAR to force FSM2trans and the rest of the forcing data coming from statistical downscaling of COSMO1, a rate of 1.2% was found.

These values only reflect domain-wide averages though, and do not speak to the effect that blowing snow sublimation has at individual pixels. Figure 4.2 shows a considerable difference in snow depths near the ridge crest when comparing HICARsnow versus FSM2 with HICAR winds. In particular, snow depths on the southern facing aspect are lower. When comparing the seasonal rates of blowing snow sublimation as a percentage of snowfall at the ridgeline, we see a clear difference between the two simulations (fig. 4.12). HICARsnow simulates maximum values around 4% at the ridge crest, while the FSM2trans simulation reports values up to 12%. While we do not expect this process alone to not account for all of the difference in snow depth at this ridge, it clearly contributes to the low snow depth values observed in the FSM2trans simulation. This effect demonstrates a clear added value of coupling FSM2trans to HICARsnow, as both models benefit from this improved process representation.

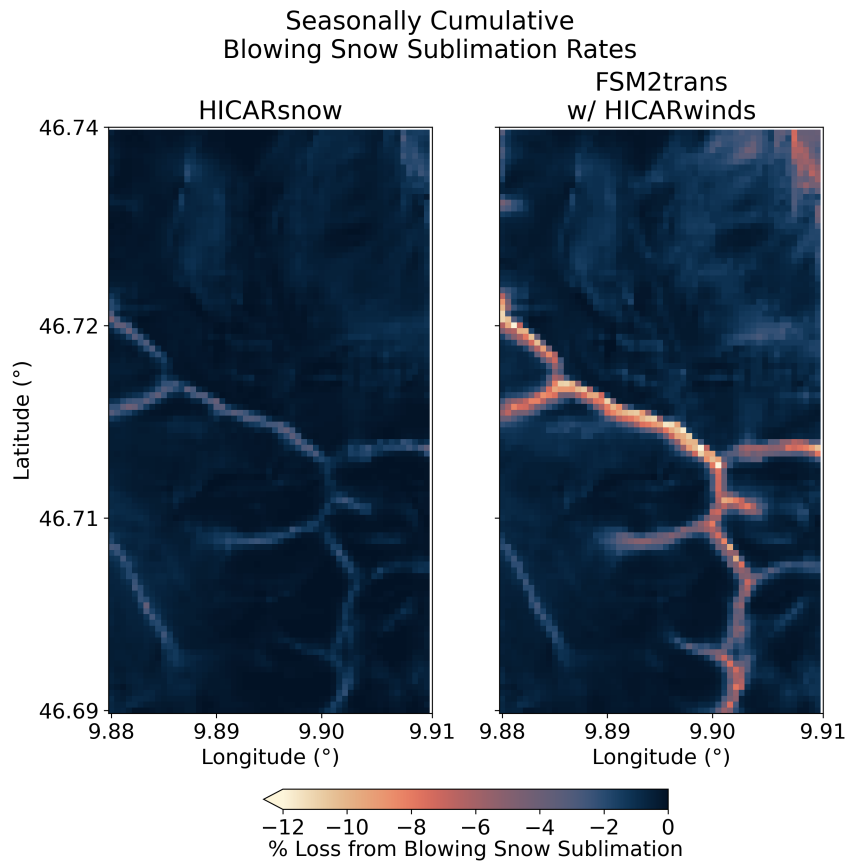


Figure 4.12: Blowing snow sublimation at the ridgeline shown in figure 4.2 as a percentage of local snowfall. Values are cumulative over the entire modeling period, October 1st - May 17th. The FSM2trans run uses only wind data from HICAR, and otherwise uses statistically downscaled COSMO1 output as forcing data.

4.4 Conclusions

In this study we have presented results from the first application of a coupled snow-atmosphere model for resolving seasonal snowpack at the hectometer scale. This was achieved by utilizing intermediate complexity snow and atmospheric models which made trade-offs in the representation of some processes in favor of increased run time. To couple the two models together, a static library approach was used, where routines from the FSM2trans snow model are called. Output from FSM2trans is used at snow-covered pixels and replaces the NoahMP LSM at these grid cells. Parallelisation of the snow redistribution schemes used in FSM2trans was required, allowing for efficient calculation of snow transport via saltation, suspension, and gravitational redistribution.

Simulated snow depth compares well with snow depth observations from an aerial LiDAR throughout the snow season. Near peak accumulation, spatial patterns in modeled snow depth vary throughout the domain according to aspect, elevation, and proximity to ridgelines,

matching the trend in observations. We attribute this in part to the models ability to represent preferential deposition at the ridge scale, and a particular snowfall event was investigated to disentangle processes that lead to the observed snow distribution. As a result, the basin-wide distribution of simulated snow depth better matches observations than FSM2trans forced without dynamically downscaled precipitation. The coupling of FSM2trans with HICAR shows clear benefits to both models, with FSM2trans improving estimates of near-surface air temperature over snow, especially during clear, calm nights. The ability for blowing snow-sublimation to feedback to the atmospheric model also results in less sublimation overall. This results in an estimate for blowing snow sublimation rates in HICARsnow of 0.35% of annual snowfall. FSM2trans forced with winds from HICAR, but statistically downscaled humidity, estimated this rate to be 1.2%, while another study which considered feedbacks of blowing snow sublimation on humidity reported 0.1% for a similar catchment Groot Zwaaftink et al., 2013a.

This study also represents the first time that adaptive habit (AHAB) microphysics schemes have been employed to study preferential deposition. We believe this development to be crucial to further understanding the phenomena, since AHAB schemes promise more physics-based predictions of particle fall speeds. Using this approach, we have demonstrated that the seeder-feeder mechanism involved in preferential deposition can also be impacted by near surface flow regimes. This finding is significant, since existing descriptions of preferential deposition typically bifurcate the process into microphysical processes and near-surface flow (Gerber et al., 2019; Vionnet et al., 2017). Instead, we find that near-surface flow features directly contribute to microphysical processes, indicating that attempts to quantify the relative contribution of each may disregard this unity. However, the conditions during this process would suggest a decrease in precipitation when using parameterizations of preferential deposition based solely on surface-winds. Ultimately, there is a large difference in computational demand between these two approaches to describing preferential deposition, and the use of simpler surface-wind parameterizations may still be useful for some applications under certain atmospheric conditions. In the direct proximity of ridges, snow redistribution is also well represented, with the approximate locations of deposits of snow similar in both LiDAR data and HICARsnow output. These features serve to improve the spatial distribution of snow depths at the basin scale.

Redistribution processes occur mostly at exposed ridges in the model, while observations show evidence of redistribution at secondary ridges and mid-elevation slopes as well. The exact cause of this discrepancy is unclear, but the 50m horizontal model resolution likely plays a role in the ability of the model to represent sub-grid processes generating snow depth variability at these locations (Quéno et al., 2023). Snow melt on southern-facing aspects is also found to be exaggerated by HICARsnow. Prior studies using the FSM2oshd model have found modeled early season melt to be heavily dependent on the snow albedo at these elevations (Cluzet et al., 2024), suggesting that improvements to modeled albedo may yield better maps of early season melt.

In all, this study demonstrates the efficacy of a novel snow-atmosphere model for resolving seasonal patterns of snow depth. The horizontal resolution used for the model simulation controls which processes are capable of being represented, and to what degree of accuracy. This said, coarser resolution (250m) runs with the HICARsnow model yielded distributions of snow depth of similar accuracy to finer resolution (50m) runs with FSM2trans and statistically downscaled data. This suggests that while hectometer-scale HICARsnow runs remain too computationally expensive for operational snow forecasting at the range scale, some trade off of scale and process representation may be found which rivals higher-resolution approaches. If sufficient computational resources are available though, coupled snow-atmosphere models show significant promise for representing seasonal patterns in snow depth at the hectometer scale.

Code and Data Availability The animations of preferential deposition mentioned in the text are available at the DOI: 10.16904/envidat.482. HICARsnow can be used for non-profit purposes under the GPLv3 license (<http://www.gnu.org/licenses/gpl-3.0.html>, last access: 1 February 2023). The GitHub repository of HICARsnow can be found at: <https://github.com/HICAR-Model/HICAR/tree/HICARsnow> with the exact version used for this study found here: 10.5281/zenodo.10679464. LiDAR data will be made available upon request, and is to be published in full in a later publication. Data from the SMN station are available at <https://opendata.swiss/en/dataset/automatische-meteorologische-bodenmessstationen>. The basemap layer used in Figure 4.1 comes from Swiss Topo. Similarly, topographic data for generating the DEM resolution comparison was obtained from Swiss Topo swissALTI3d (<https://www.swisstopo.admin.ch/de/hoehenmodell-swissalti3d>)

Acknowledgements The authors thank the funding source of this project, the Swiss National Science Foundation grant #188554. The computational resources needed to perform the simulations were provided by the Swiss National Supercomputing Center (CSCS) through project sm78. The authors would like to thank Franziska Gerber for advice on coupled snow-atmosphere modeling setups, as well as additional developers of the FSM2oshd model including Tobias Jonas, Jan Magnusson, Clare Webster, Giulia Mazzotti, Johanna Malle, and Bertrand Cluzet. Developers of open source python toolboxes, particularly xarray and xesmf, have also played a crucial role in this study by enabling efficient analysis and manipulation of large datasets.

5 Conclusions

This thesis has presented the first application of coupled snow-atmosphere modeling at seasonal time scales. Along the way, the potential of diagnostic wind solvers in combination with terrain descriptors has been shown to yield wind fields in complex terrain which simulate similar features to more complex, Navier-Stokes based solvers. Such wind solvers have particular use at high resolutions, where influences on wind fields such as mesoscale pressure gradients and Coriolis forces can be neglected or are represented by a coarser resolution parent solver. At these high resolutions, the computational cost of running Navier-Stokes based solvers also becomes prohibitive for studies of seasonal duration. The shortcuts to the model dynamics of HICAR lead to faster run times compared with conventional NWP models for a variety of reasons.

First, we note in Chapter 2 that surface wind speeds from the diagnostic solver are lower than those from the WRF model. Studies employing WRF at the hectometer scale in complex terrain have found the model to overestimate wind speeds (Gerber et al., 2018; Goger et al., 2022), suggesting that these lower wind speeds are reasonable. As a result of lower wind speeds, the chosen advection scheme is stable for longer time steps, directly scaling the model run time. The simplification to the model dynamics also means that numerical integration of the Navier-Stokes equations, and of the equation for pressure, can be neglected in favor of the solution of an optimization problem. By removing these equations from the dynamical core, any instabilities arising from horizontal pressure gradients in vertically stretched coordinate systems are also avoided, permitting longer run times. As a demonstration of this, the simulations presented in Chapter 4 using HICARsnow had average time steps around 1 second, while Gerber et al., 2018, who performed WRF simulations over the same domain, found that time steps of 1/27 second were necessary to achieve numerical stability. This reported time step is also for smoothed topography, while HICAR requires no such topographic smoothing, resulting in a more accurate representation of terrain. This point has significant implications for coupled snow-atmosphere modeling. During the ablation season, radiation and temperature provide energy inputs to the snowpack, driving melt. Both variables have some elevation dependency, with colder temperatures found at higher elevations, and radiative

Chapter 5. Conclusions

transfer attenuated by the atmosphere. A mountain top represented at an elevation of 2800 m will experience a different input of energy than the same mountain when represented at an elevation of 3000 m.

Finally, the simplified model dynamics allow for a larger vertical grid spacing, reducing the number of computational elements needed for a given simulation. This point requires the additional qualification that a coarsening of the vertical grid will result in a poorer representation of near-surface processes, where vertical gradients are often greater than higher up in the atmosphere. Given the performance of HICAR in the studies presented here, we conclude that the vertical coarsening currently implemented makes a balanced trade-off between computational demand and process representation. All of these benefits which follow from the simplified model dynamics, in combination with optimization of the code and targeting a high level of optimization on a native compiler, result in the model speed up reported here.

Despite these simplifications, HICAR is still shown to give good predictions of near-surface variables relevant to forcing land surface models. Precipitation patterns in complex terrain are shown to be within the spread of estimates produced by operational forecasting offices (section 2.4.2). Near-surface flow features observed using a wind LiDAR, particularly when driven by terrain-flow interactions, can also be simulated by the model. A new form of Doppler wind LiDAR scans, RHE scans, was also proposed to best sample ridge-crest speed up in complex terrain. Surface radiative inputs and 2m air temperatures were also validated against station measurements over springtime snow cover at a horizontal model resolution of 50 m. Model bias and RMSE for 2m air temperature was found to outperform estimates from a 1 km operational NWP model, even when stations to which the NWP model was assimilated were included. 2m air temperature was found to exhibit a large negative bias over snow during calm, clear nights, but this bias was rectified when coupling HICAR with the FSM2trans snow model (section 4.3.3).

Coupling HICAR to the FSM2trans snow model was shown to improve estimates of snow depth distribution relative to the FSM2trans model forced with statistical downscaling, or when forced with statistical downscaling and HICAR winds alone. This improvement confirms the original hypothesis of this study, namely that dynamic downscaling can produce more accurate forcing data for land surface modeling than statistical techniques. Interestingly, dynamic downscaling was found to produce distributions of snow depth at a 250 m resolution which are comparable to distributions obtained using mixed statistical and dynamic downscaling at a 50 m resolution. This was attributed to the representation of snowfall at the hectometer scale such as preferential deposition, which increase snow depth heterogeneity. This heterogeneity introduced by snowfall processes was shown to improve distributions of snow depth for both 50 m and 250 m dynamically downscaled simulations when compared to a 50 m statistically downscaled simulation.

HICARsnow achieves this in part by representing preferential deposition, resolving interactions between the mean flow field, near-surface flow features, and microphysical processes.

HICARsnow implements the ISHMAEL microphysics scheme to track multiple ice species and consider how their interactions lead to the signal of preferential deposition. This first-of-its-kind application of AHAB microphysics schemes to the study of preferential deposition reveals how microphysical processes such as seeder-feeder clouds interact with near-surface flow features and generate enhanced leeside precipitation. This result motivates further study of preferential deposition with AHAB schemes to understand how their performance relative to two-moment microphysics schemes is affected by particular atmospheric conditions.

This thesis has demonstrated that intermediate complexity atmospheric modeling is possible at the hectometer scale, and that it can represent precipitation patterns which remain a challenge for statistical downscaling techniques. The atmospheric model HICAR has potential to improve forecasts of snow in complex terrain, as shown in Chapter 4. Regional scale climate studies, where downscaling techniques are needed to bring decades of coarse-resolution GCM simulations to the kilometer or hectometer scale, are another area where the model could prove useful. We temper the conclusions of this thesis with limitations of the approach in the following section, ending with an outlook toward future research opportunities founded on the work presented here.

6 Limitations and Outlook

The design philosophy behind the HICAR model inherently leads to shortcomings relative to other atmospheric models. This is done in the pursuit of faster model run times, but does come at the cost of physical accuracy. The model mostly makes changes to the model dynamics, which reduce the number of physical processes considered when calculating a 3D wind field. As discussed in section 3.3.4, one of the main processes ignored is turbulence. The usage of a diagnostic wind solver uses a fundamentally different approach to calculating the wind field when compared with a solver based on the Navier-Stokes equations. Without considering these equations, effects on the wind field due to local variations in air pressure, density, and turbulent exchange will not be included. Comparisons against the WRF atmospheric model and observations from a wind LiDAR show that HICAR can simulate surface wind speeds and the presence of eddies when they form in the leeside of terrain features (section 2.4.1 and 3.3.3). However, turbulent structures arising from vertical wind shear or buoyancy differences away from the surface are neither considered by the model nor present when comparing against observations (section 3.3.4). Additionally, when turbulent structures in the lee of terrain are simulated, the extent is often incorrect, and the structures themselves exhibit little change over time scales smaller than the interval between forcing updates. This is due to the linear interpolation of HICAR's wind field through time between calls to the wind solver. This restricts the model from studies concerned with resolving turbulent exchanges for particular events. Of interest, the work of (Haugeneder et al., 2024) does show that the energy balance of seasonal snow is greatly affected by ephemeral eddies during the melt season when patchy snow is present. However, these processes occur at resolutions less than 10s of meters, meaning it would need to be parameterized at the sub-grid scale for RANs- or LES-based models as well. Indeed, a prior study using the LES-WRF setup showed that the simulation still overpredicts turbulent kinetic energy relative to an eddy covariance tower, in some cases up to an order of magnitude (Goger et al., 2022). So, while HICAR may not include these processes at all, reasonable process-representation in models which do consider the sources and sinks of turbulent energy is also not guaranteed.

These model limitations are accepted under the cause of reduced model run time, ultimately

with the goal of operational applications for the model. This raises another limitation of the model: the remaining efficiencies needed to achieve operational readiness. At a bare minimum, operational weather forecasting requires that a unit of simulation time be faster than the same unit of real time. Operational readiness is as much a function of computational resources as it is of model performance. Still, for the HICARsnow model presented in Chapter 4, one day of model simulation at 50 m resolution can require up to 54 minutes of simulation time when running on 360 CPUs, and up to 14 minutes at 250 m with the same number of CPUs. The lateral extent of this 50 m domain is only 175 km², compared to the 41,000 km² domain used for the operational snow hydrological forecast performed for Switzerland. This represents roughly 235x more computational elements than the target domain over the Upper Dischma catchment used in Chapter 4. If one fixes the number of computational resources and allows for a forecast which runs as fast as real time, a roughly 10x speed up of the model would still be required. Possible avenues for achieving this speed up are discussed in the final paragraph.

The success of HICAR in explicitly simulating preferential deposition with an adaptive habit microphysics scheme motivates further research into this method. Comola et al., 2019 previously found that particle properties affect the pattern of preferential deposition under various atmospheric conditions. In Chapter 4, we have only investigated preferential deposition for one storm. One potential next step is to examine the ability of AHAB schemes to resolve various patterns of preferential deposition under varying atmospheric conditions. Another possibility would be to understand at what spatial scales, if any, AHAB schemes offer diminishing improvements over two-moment schemes. Earlier studies have shown that AHAB schemes predict different precipitation patterns at the range scale compared to non-AHAB schemes, but the results from Chapter 4 suggest that differences at the ridge scale may be less significant. Still, this study examined just one snowfall event at the ridge scale, and further investigation of precipitation downscaling using AHAB schemes is needed. Understanding how these schemes differ from two-moment microphysics schemes would allow for a considered trade off between process representation and model run time. Lastly, AHAB schemes like ISHMAEL offer information about the structure of falling snow which may have added benefits to snowpack modeling. For example, both ISHMAEL and CRYOWRF use a best-number (Mitchell, 1996) approach to calculating particle fall speeds. CRYOWRF assumes spherical ice particles, while ISHMAEL calculates the best-number considering any form of oblate ice. Clearly, this information from ISHMAEL could benefit the blowing snow scheme in CRYOWRF. Additionally, processes occurring in the snowpack that alter the snow microstructure require some initial state of the snow crystals. Information on snow crystal shape could thus benefit predictions of the density of both new snow and snow layers, as well as the optical properties of the snowpack related to grain size and type. This may improve upon estimates of surface shortwave albedo and threshold friction velocity for snow transport, both of which were identified in Chapter 4 as potential shortcomings of the FSM2trans model. Coupling HICAR to one of these snow-physics models is thus a tempting avenue for future research.

Chapter 4 also identified differences between observed snow depth from an aerial LiDAR

survey and HICAR snow output, particularly in the presence of small-scale terrain features. This may occur if a ridge is sharper at higher resolutions, resulting in a sharper discontinuity in the wind field and thus more net wind transport of snow. Similarly, a bare grid cell next to one covered in small boulders may experience net scouring of snow without roughness elements to generate areas of stagnation. In contrast, the boulder-covered grid cell would experience scour and deposition, resulting in a net flux of snow closer to 0. One could imagine extracting data from a very high-resolution DEM, say at a resolution of 2m, and using this information about differences between resolved and unresolved terrain features to modify snow transport amounts.

Finally, as any programmer would promise, there remain areas of further optimization for the model. When considering operational snow forecasting over Switzerland, the extreme differences in terrain complexity between the Valais Alps and the Swiss Plateau demonstrate that one fixed grid resolution may not be economical. More grid elements will be needed to represent the shape of the Matterhorn than, say, Hönnggerberg. This approach of irregular gridding is being used in many modern NWP models (Skamarock et al., 2012; Wan et al., 2013) as well as one operational snow model (Marsh et al., 2020). Such an approach would allow for a reduction in the number of grid elements, reducing the overall run time. Next, all of the model code is currently written to run on CPUs. Over the past 10 years, however, NWP models have turned toward using GPUs to accelerate certain routines, especially physics parameterizations. The modularity of these parameterizations makes it simple to benefit from open-source code which re-writes existing parameterizations to run on GPUs. Porting the microphysics schemes and radiation modules of HICAR, which currently comprise roughly two-thirds of the model run time, may result in model speed up of 3x. Lastly, exploring alternative advection schemes with larger stability envelopes may allow for a further reduction of the model time step. Seen in this way, the current limitations of the model represent opportunities for advancing its performance even further.

The promise of dynamic downscaling for operational snow hydrologic modeling remains in the future, but the HICARsnow model demonstrates the potential that exists and points the way towards realising this goal.

Bibliography

- Agency, E. E. (2006). Corine land cover (clc) 2006 raster data, version 13 [<https://www.eea.europa.eu/data-and-maps/data/clc-2006-raster>].
- Anderson, E. A. (1976). *A point energy and mass balance model of a snow cover*. [Doctoral dissertation] [Ph.D.]. Stanford University.
- Arduini, G., Balsamo, G., Dutra, E., Day, J. J., Sandu, I., Boussetta, S., & Haiden, T. (2019). Impact of a multi-layer snow scheme on near-surface weather forecasts. *Journal of Advances in Modeling Earth Systems*, *11*(12), 4687–4710. <https://doi.org/https://doi.org/10.1029/2019MS001725>
- Barnett, T. P., Adam, J. C., & Lettenmaier, D. P. (2005). Potential impacts of a warming climate on water availability in snow-dominated regions. *Nature*, *438*(7066), 303–309. <https://doi.org/10.1038/nature04141>
- Benjamin, S. G., Weygandt, S. S., Brown, J. M., Hu, M., Alexander, C. R., Smirnova, T. G., Olson, J. B., James, E. P., Dowell, D. C., Grell, G. A., Lin, H., Peckham, S. E., Smith, T. L., Moninger, W. R., Kenyon, J. S., & Manikin, G. S. (2016). A north american hourly assimilation and model forecast cycle: the rapid refresh. *Monthly Weather Review*, *144*(4), 1669–1694. <https://doi.org/10.1175/MWR-D-15-0242.1>
- Berg, J., Reynolds, D., Quéno, L., Jonas, T., Lehning, M., & Mott, R. (2024, in prep). A seasonal snowpack model forced with dynamically downscaled forcing data resolves hydrologically relevant accumulation patterns.
- Bergeron, T. (1965). On the low-level redistribution of atmospheric water caused by orography. *Suppl. Proc. Int. Conf. Cloud Phys., Tokyo, 1965*, 96–100. <https://cir.nii.ac.jp/crid/1570009750214671104>
- Bernhardt, M., & Schulz, K. (2010). Snowslide: a simple routine for calculating gravitational snow transport. *Geophysical Research Letters*, *37*(11). <https://doi.org/https://doi.org/10.1029/2010GL043086>
- Bernhardt, M., Schulz, K., Liston, G., & Zängl, G. (2012). The influence of lateral snow redistribution processes on snow melt and sublimation in alpine regions. *Journal of Hydrology*, *424-425*, 196–206. <https://doi.org/https://doi.org/10.1016/j.jhydrol.2012.01.001>
- Boé, J., Terray, L., Habets, F., & Martin, E. (2007). Statistical and dynamical downscaling of the seine basin climate for hydro-meteorological studies. *International Journal of Climatology*, *27*(12), 1643–1655. <https://doi.org/https://doi.org/10.1002/joc.1602>

Bibliography

- Bonekamp, P. N. J., Collier, E., & Immerzeel, W. W. (2018). The impact of spatial resolution, land use, and spinup time on resolving spatial precipitation patterns in the himalayas. *Journal of Hydrometeorology*, 19(10), 1565–1581. <https://doi.org/10.1175/JHM-D-17-0212.1>
- Bozkurt, D., Rojas, M., Boisier, J. P., Rondanelli, R., Garreaud, R., & Gallardo, L. (2019). Dynamical downscaling over the complex terrain of southwest south america: present climate conditions and added value analysis. *Climate Dynamics*, 53(11), 6745–6767. <https://doi.org/10.1007/s00382-019-04959-y>
- Chen, F., & Dudhia, J. (2001). Coupling an advanced land surface–hydrology model with the penn state–ncar mm5 modeling system. part i: model implementation and sensitivity. *Monthly Weather Review*, 129(4), 569–585. [https://doi.org/https://doi.org/10.1175/1520-0493\(2001\)129<0569:CAALSH>2.0.CO;2](https://doi.org/https://doi.org/10.1175/1520-0493(2001)129<0569:CAALSH>2.0.CO;2)
- Chen, J.-P., & Lamb, D. (1994). The theoretical basis for the parameterization of ice crystal habits: growth by vapor deposition. *Journal of Atmospheric Sciences*, 51(9), 1206–1222. [https://doi.org/10.1175/1520-0469\(1994\)051<1206:TTBFTP>2.0.CO;2](https://doi.org/10.1175/1520-0469(1994)051<1206:TTBFTP>2.0.CO;2)
- Chow, F. K., Schär, C., Ban, N., Lundquist, K. A., Schlemmer, L., & Shi, X. (2019). Crossing multiple gray zones in the transition from mesoscale to microscale simulation over complex terrain. *Atmosphere*, 10(5). <https://doi.org/10.3390/atmos10050274>
- Cluzet, B., Magnusson, J., Quéno, L., Mazzotti, G., Mott, R., & Jonas, T. (2024). Using sentinel-1 wet snow maps to inform fully-distributed physically-based snowpack models. *EGU-sphere*, 2024, 1–24. <https://doi.org/10.5194/egusphere-2024-209>
- Collados-Lara, A.-J., Pardo-Igúzquiza, E., Pulido-Velazquez, D., & Jiménez-Sánchez, J. (2018). Precipitation fields in an alpine mediterranean catchment: inversion of precipitation gradient with elevation or undercatch of snowfall? *International Journal of Climatology*, 38(9), 3565–3578. <https://doi.org/10.1002/joc.5517>
- Collier, E., Mölg, T., Maussion, F., Scherer, D., Mayer, C., & Bush, A. B. G. (2013). High-resolution interactive modelling of the mountain glacier–atmosphere interface: an application over the karakoram. *The Cryosphere*, 7(3), 779–795. <https://doi.org/10.5194/tc-7-779-2013>
- Comola, F., Giometto, M. G., Salesky, S. T., Parlange, M. B., & Lehning, M. (2019). Preferential deposition of snow and dust over hills: governing processes and relevant scales. *Journal of Geophysical Research: Atmospheres*, 124(14), 7951–7974. <https://doi.org/10.1029/2018JD029614>
- Comola, F., Kok, J. F., Gaume, J., Paterna, E., & Lehning, M. (2017). Fragmentation of wind-blown snow crystals. *Geophysical Research Letters*, 44(9), 4195–4203. <https://doi.org/10.1002/2017gl073039>
- Costanza, R., d’Arge, R., de Groot, R., Farber, S., Grasso, M., Hannon, B., Limburg, K., Naeem, S., O’Neill, R. V., Paruelo, J., Raskin, R. G., Sutton, P., & van den Belt, M. (1997). The value of the world’s ecosystem services and natural capital. *Nature*, 387(6630), 253–260. <https://doi.org/10.1038/387253a0>
- Crameri, F. (2021, September). *Scientific colour maps* (Version 7.0.1) [The development of the Scientific colour maps is not funded any longer, but will continue as a pro bono

- project for the scientific community. - Fabio]. Zenodo. <https://doi.org/10.5281/zenodo.5501399>
- Dadic, R., Mott, R., Lehning, M., & Burlando, P. (2010). Parameterization for wind-induced preferential deposition of snow. *Hydrological Processes*, *24*(14), 1994–2006. <https://doi.org/https://doi.org/10.1002/hyp.7776>
- Daly, C., Neilson, R. P., & Phillips, D. L. (1994). A statistical-topographic model for mapping climatological precipitation over mountainous terrain. *Journal of Applied Meteorology and Climatology*, *33*(2), 140–158. [https://doi.org/10.1175/1520-0450\(1994\)033<0140:ASTMFM>2.0.CO;2](https://doi.org/10.1175/1520-0450(1994)033<0140:ASTMFM>2.0.CO;2)
- Deems, J. S., Fassnacht, S. R., & Elder, K. J. (2006). Fractal distribution of snow depth from lidar data. *Journal of Hydrometeorology*, *7*(2), 285–297. <https://doi.org/10.1175/JHM487.1>
- Deems, J. S., Painter, T. H., & Finnegan, D. C. (2013). Lidar measurement of snow depth: a review. *Journal of Glaciology*, *59*(215), 467–479. <https://doi.org/10.3189/2013JoG12J154>
- Doorschot, J. J. J., & Lehning, M. (2002). Equilibrium saltation: mass fluxes, aerodynamic entrainment, and dependence on grain properties. *Boundary-Layer Meteorology*, *104*(1), 111–130. <https://doi.org/10.1023/A:1015516420286>
- Dujardin, J., & Lehning, M. (2022). Wind-topo: downscaling near-surface wind fields to high-resolution topography in highly complex terrain with deep learning. *Quarterly Journal of the Royal Meteorological Society*, *148*(744), 1368–1388. <https://doi.org/10.1002/qj.4265>
- Egli, L., Jonas, T., Grünwald, T., Schirmer, M., & Burlando, P. (2012). Dynamics of snow ablation in a small alpine catchment observed by repeated terrestrial laser scans. *Hydrological Processes*, *26*(10), 1574–1585. <https://doi.org/https://doi.org/10.1002/hyp.8244>
- Ek, M. B., Mitchell, K. E., Lin, Y., Rogers, E., Grunmann, P., Koren, V., Gayno, G., & Tarpley, J. D. (2003). Implementation of noah land surface model advances in the national centers for environmental prediction operational mesoscale eta model. *Journal of Geophysical Research: Atmospheres*, *108*(D22). <https://doi.org/10.1029/2002JD003296>
- Erell, E., Leal, V., & Maldonado, E. (2005). Measurement of air temperature in the presence of a large radiant flux: an assessment of passively ventilated thermometer screens. *Boundary-Layer Meteorology*, *114*(1), 205–231.
- Essery, R. (2015). A factorial snowpack model (fsm 1.0). *Geoscientific Model Development*, *8*(12), 3867–3876. <https://doi.org/10.5194/gmd-8-3867-2015>
- Essery, R., Rutter, N., Pomeroy, J., Baxter, R., Stähli, M., Gustafsson, D., Barr, A., Bartlett, P., & Elder, K. (2009). Snowmip2: an evaluation of forest snow process simulations. *Bulletin of the American Meteorological Society*, *90*(8), 1120–1136. <https://doi.org/10.1175/2009BAMS2629.1>
- Farina, S., & Zardi, D. (2023). Understanding thermally driven slope winds: recent advances and open questions. *Boundary-Layer Meteorology*, *189*(1–3), 5–52. <https://doi.org/10.1007/s10546-023-00821-1>
- Filhol, S., & Sturm, M. (2015). Snow bedforms: a review, new data, and a formation model. *Journal of Geophysical Research: Earth Surface*, *120*(9), 1645–1669. <https://doi.org/https://doi.org/10.1002/2015JF003529>

Bibliography

- Finardi, S., Brusasca, G., Morselli, M. G., Trombetti, F., & Tampieri, F. (1993). Boundary-layer flow over analytical two-dimensional hills: a systematic comparison of different models with wind tunnel data. *Boundary-Layer Meteorology*, 63(3), 259–291. <https://doi.org/10.1007/BF00710462>
- Forthofer, J. (2007). Modeling wind in complex terrain for use in fire spread prediction [MSc thesis, Colorado State University, Fort Collins].
- Forthofer, J., Butler, B., & Wagenbrenner, N. (2014). A comparison of three approaches for simulating fine-scale surface winds in support of wildland fire management. part i. model formulation and comparison against measurements. *International Journal of Wildland Fire*, 23, 969–981. <https://doi.org/10.1071/WF12089>
- Frei, C. (2014). Interpolation of temperature in a mountainous region using nonlinear profiles and non-euclidean distances. *International Journal of Climatology*, 34(5), 1585–1605. <https://doi.org/https://doi.org/10.1002/joc.3786>
- Gal-Chen, T., & Somerville, R. C. (1975). On the use of a coordinate transformation for the solution of the navier-stokes equations. *Journal of Computational Physics*, 17(2), 209–228. [https://doi.org/10.1016/0021-9991\(75\)90037-6](https://doi.org/10.1016/0021-9991(75)90037-6)
- Gallée, H., Guyomarc'h, G., & Brun, E. (2001). Impact of snow drift on the antarctic ice sheet surface mass balance: possible sensitivity to snow-surface properties. *Boundary-Layer Meteorology*, 99(1), 1–19. <https://doi.org/10.1023/A:1018776422809>
- Gao, Y., Xiao, L., Chen, D., Chen, F., Xu, J., & Xu, Y. (2017). Quantification of the relative role of land-surface processes and large-scale forcing in dynamic downscaling over the tibetan plateau. *Climate Dynamics*, 45(5), 1705–1721. <https://doi.org/10.1007/s00382-016-3168-6>
- Gerber, F., Besic, N., Sharma, V., Mott, R., Daniels, M., Gabella, M., Berne, A., Germann, U., & Lehning, M. (2018). Spatial variability in snow precipitation and accumulation in cosmo-wrf simulations and radar estimations over complex terrain. *The Cryosphere*, 12(10), 3137–3160. <https://doi.org/10.5194/tc-12-3137-2018>
- Gerber, F., & Lehning, M. (2021). High resolution static data for wrf over switzerland. <https://doi.org/http://dx.doi.org/10.16904/envidat.233>
- Gerber, F., Mott, R., & Lehning, M. (2019). The importance of near-surface winter precipitation processes in complex alpine terrain. *Journal of Hydrometeorology*, 20(2), 177–196. <https://doi.org/10.1175/JHM-D-18-0055.1>
- Gerber, F., & Sharma, V. (2018). Running cosmo-wrf on very-high resolution over complex terrain. <https://doi.org/http://dx.doi.org/10.16904/envidat.35>
- Germann, U., Boscacci, M., Clementi, L., Gabella, M., Hering, A., Sartori, M., Sideris, I. V., & Calpini, B. (2022). Weather radar in complex orography. *Remote Sensing*, 14(3). <https://doi.org/10.3390/rs14030503>
- Giorgi, F., & Gutowski, W. J. (2015). Regional dynamical downscaling and the cordex initiative. *Annual Review of Environment and Resources*, 40(1), 467–490. <https://doi.org/10.1146/annurev-environ-102014-021217>
- Goger, B., Rotach, M. W., Gohm, A., Fuhrer, O., Stiperski, I., & Holtslag, A. A. M. (2018). The impact of three-dimensional effects on the simulation of turbulence kinetic energy in

- a major alpine valley. *Boundary-Layer Meteorology*, 168(1), 1–27. <https://doi.org/10.1007/s10546-018-0341-y>
- Goger, B., Stiperski, I., Nicholson, L., & Sauter, T. (2022). Large-eddy simulations of the atmospheric boundary layer over an alpine glacier: impact of synoptic flow direction and governing processes. *Quarterly Journal of the Royal Meteorological Society*, 148(744), 1319–1343. <https://doi.org/10.1002/qj.4263>
- Gómez-Navarro, J. J., Raible, C. C., & Dierer, S. (2015). Sensitivity of the wrf model to pbl parametrisations and nesting techniques: evaluation of wind storms over complex terrain. *Geoscientific Model Development*, 8(10), 3349–3363. <https://doi.org/10.5194/gmd-8-3349-2015>
- Goodin, W. R., McRae, G. J., & Seinfeld, J. H. (1980). An objective analysis technique for constructing three-dimensional urban-scale wind fields. *Journal of Applied Meteorology and Climatology*, 19(1), 98–108. [https://doi.org/10.1175/1520-0450\(1980\)019<0098:AOATFC>2.0.CO;2](https://doi.org/10.1175/1520-0450(1980)019<0098:AOATFC>2.0.CO;2)
- Gossart, A., Souverijns, N., Gorodetskaya, I. V., Lhermitte, S., Lenaerts, J. T. M., Schween, J. H., Mangold, A., Laffineur, Q., & van Lipzig, N. P. M. (2017). Blowing snow detection from ground-based ceilometers: application to east antarctica. *The Cryosphere*, 11(6), 2755–2772. <https://doi.org/10.5194/tc-11-2755-2017>
- Grisogono, B., Jurlina, T., Večenaj, Ž., & Güttler, I. (2015). Weakly nonlinear prandtl model for simple slope flows. *Quarterly Journal of the Royal Meteorological Society*, 141(688), 883–892. <https://doi.org/https://doi.org/10.1002/qj.2406>
- Groot Zwaaftink, C. D., Mott, R., & Lehning, M. (2013a). Seasonal simulation of drifting snow sublimation in alpine terrain. *Water Resources Research*, 49(3), 1581–1590. <https://doi.org/https://doi.org/10.1002/wrcr.20137>
- Groot Zwaaftink, C. D., Mott, R., & Lehning, M. (2013b). Seasonal simulation of drifting snow sublimation in Alpine terrain. *Water Resources Research*, 49(3), 1581–1590. <https://doi.org/10.1002/wrcr.20137>
- Grünewald, T., Schirmer, M., Mott, R., & Lehning, M. (2010). Spatial and temporal variability of snow depth and ablation rates in a small mountain catchment. *The Cryosphere*, 4(2), 215–225. <https://doi.org/10.5194/tc-4-215-2010>
- Grünewald, T., Stötter, J., Pomeroy, J. W., Dadic, R., Moreno Baños, I., Marturià, J., Spross, M., Hopkinson, C., Burlando, P., & Lehning, M. (2013). Statistical modelling of the snow depth distribution in open alpine terrain. *Hydrology and Earth System Sciences*, 17(8), 3005–3021. <https://doi.org/10.5194/hess-17-3005-2013>
- Grünewald, T., & Lehning, M. (2015). Are flat-field snow depth measurements representative? a comparison of selected index sites with areal snow depth measurements at the small catchment scale. *Hydrological Processes*, 29(7), 1717–1728. <https://doi.org/10.1002/hyp.10295>
- Gutiérrez, J. M., San-Martín, D., Brands, S., Manzanas, R., & Herrera, S. (2013). Reassessing statistical downscaling techniques for their robust application under climate change conditions. *Journal of Climate*, 26(1), 171–188. <https://doi.org/https://doi.org/10.1175/JCLI-D-11-00687.1>

Bibliography

- Gutmann, E., Barstad, I., Clark, M., Arnold, J., & Rasmussen, R. (2016). The intermediate complexity atmospheric research model (icar). *Journal of Hydrometeorology*, 17(3), 957–973. <https://doi.org/10.1175/JHM-D-15-0155.1>
- Gutmann, E. D., Rasmussen, R. M., Liu, C., Ikeda, K., Gochis, D. J., Clark, M. P., Dudhia, J., & Thompson, G. (2012). A comparison of statistical and dynamical downscaling of winter precipitation over complex terrain. *Journal of Climate*, 25(1), 262–281. <https://doi.org/https://doi.org/10.1175/2011JCLI4109.1>
- Harder, P., & Pomeroy, J. W. (2014). Hydrological model uncertainty due to precipitation-phase partitioning methods. *Hydrological Processes*, 28(14), 4311–4327. <https://doi.org/https://doi.org/10.1002/hyp.10214>
- Harrington, J. Y., Sulia, K., & Morrison, H. (2013a). A method for adaptive habit prediction in bulk microphysical models. part i: theoretical development. *J. Atmos. Sci.*, 70, 349–364.
- Haugeneder, M., Lehning, M., Stiperski, I., Reynolds, D., & Mott, R. (2024). Turbulence in the strongly heterogeneous near-surface boundary layer over patchy snow. *Boundary-Layer Meteorology*, 190(2). <https://doi.org/10.1007/s10546-023-00856-4>
- Helbig, N., L'we, H., Mayer, B., & Lehning, M. (2010). Explicit validation of a surface shortwave radiation balance model over snow-covered complex terrain. *Journal of Geophysical Research: Atmospheres*, 115(D18). <https://doi.org/https://doi.org/10.1029/2010JD013970>
- Helbig, N., Mott, R., Bühler, Y., Le Toumelin, L., & Lehning, M. (2024). Snowfall deposition in mountainous terrain: a statistical downscaling scheme from high-resolution model data on simulated topographies. *Frontiers in Earth Science*, 11. <https://doi.org/10.3389/feart.2023.1308269>
- Henn, B., Musselman, K. N., Lestak, L., Ralph, F. M., & Molotch, N. P. (2020). Extreme runoff generation from atmospheric river driven snowmelt during the 2017 oroville dam spillways incident [e2020GL088189 2020GL088189]. *Geophysical Research Letters*, 47(14), e2020GL088189. <https://doi.org/https://doi.org/10.1029/2020GL088189>
- Hock, R. (2003). Temperature index melt modelling in mountain areas [Mountain Hydrology and Water Resources]. *Journal of Hydrology*, 282(1), 104–115. [https://doi.org/https://doi.org/10.1016/S0022-1694\(03\)00257-9](https://doi.org/https://doi.org/10.1016/S0022-1694(03)00257-9)
- Homicz, G. F. (2002). Three-dimensional wind field modeling: a review. <https://doi.org/10.2172/801406>
- Hong, S.-Y., Noh, Y., & Dudhia, J. (2006). A new vertical diffusion package with an explicit treatment of entrainment processes. *Monthly Weather Review*, 134(9), 2318–2341. <https://doi.org/https://doi.org/10.1175/MWR3199.1>
- Hong, S.-Y., & Pan, H.-L. (1996). Nonlocal boundary layer vertical diffusion in a medium-range forecast model. *Monthly Weather Review*, 124(10), 2322–2339. [https://doi.org/https://doi.org/10.1175/1520-0493\(1996\)124<2322:NBLVDI>2.0.CO;2](https://doi.org/https://doi.org/10.1175/1520-0493(1996)124<2322:NBLVDI>2.0.CO;2)
- Horak, J., Hofer, M., Gutmann, E., Gohm, A., & Rotach, M. W. (2021). A process-based evaluation of the intermediate complexity atmospheric research model (icar) 1.0.1. *Geoscientific Model Development*, 14(3), 1657–1680. <https://doi.org/10.5194/gmd-14-1657-2021>

- Horak, J., Hofer, M., Maussion, F., Gutmann, E., Gohm, A., & Rotach, M. W. (2019). Assessing the added value of the intermediate complexity atmospheric research (icar) model for precipitation in complex topography. *Hydrology and Earth System Sciences*, 23(6), 2715–2734. <https://doi.org/10.5194/hess-23-2715-2019>
- Houze, R. A., & Medina, S. (2005). Turbulence as a mechanism for orographic precipitation enhancement. *Journal of the Atmospheric Sciences*, 62(10), 3599–3623. <https://doi.org/10.1175/JAS3555.1>
- Jensen, A. A., Harrington, J. Y., & Morrison, H. (2018). Impacts of ice particle shape and density evolution on the distribution of orographic precipitation. *Journal of the Atmospheric Sciences*, 75(9), 3095–3114. <https://doi.org/10.1175/JAS-D-17-0400.1>
- Jensen, A. A., Harrington, J. Y., Morrison, H., & Milbrandt, J. A. (2017). Predicting ice shape evolution in a bulk microphysics model. *Journal of the Atmospheric Sciences*, 74(6), 2081–2104. <https://doi.org/https://doi.org/10.1175/JAS-D-16-0350.1>
- Jiménez, P. A., Dudhia, J., González-Rouco, J. F., Navarro, J., Montávez, J. P., & García-Bustamante, E. (2012). A revised scheme for the wrf surface layer formulation. *Monthly Weather Review*, 140(3), 898–918. <https://doi.org/https://doi.org/10.1175/MWR-D-11-00056.1>
- Jonas, T., Webster, C., Mazzotti, G., & Malle, J. (2020). Hpeval: a canopy shortwave radiation transmission model using high-resolution hemispherical images. *Agricultural and Forest Meteorology*, 284, 107903. <https://doi.org/https://doi.org/10.1016/j.agrformet.2020.107903>
- Khadka, A., Wagon, P., Brun, F., Shrestha, D., Lejeune, Y., & Arnaud, Y. (2022). Evaluation of era5-land and harv2 reanalysis data at high elevation in the upper dudh koshi basin (everest region, nepal). *Journal of Applied Meteorology and Climatology*, 61(8), 931–954. <https://doi.org/10.1175/JAMC-D-21-0091.1>
- Krinner, G., Derksen, C., Essery, R., Flanner, M., Hagemann, S., Clark, M., Hall, A., Rott, H., Brutel-Vuilmet, C., Kim, H., Ménard, C. B., Mudryk, L., Thackeray, C., Wang, L., Arduini, G., Balsamo, G., Bartlett, P., Boike, J., Boone, A., . . . Zhu, D. (2018). Esm-snowmip: assessing snow models and quantifying snow-related climate feedbacks. *Geoscientific Model Development*, 11(12), 5027–5049. <https://doi.org/10.5194/gmd-11-5027-2018>
- Kruyt, B., Mott, R., Fiddes, J., Gerber, F., Sharma, V., & Reynolds, D. (2022). A downscaling intercomparison study: the representation of slope- and ridge-scale processes in models of different complexity. *Frontiers in Earth Science*, 10. <https://doi.org/10.3389/feart.2022.789332>
- Lafaysse, M., Cluzet, B., Dumont, M., Lejeune, Y., Vionnet, V., & Morin, S. (2017). A multiphysical ensemble system of numerical snow modelling. *The Cryosphere*, 11(3), 1173–1198. <https://doi.org/10.5194/tc-11-1173-2017>
- Lehning, M., Löwe, H., Ryser, M., & Raderschall, N. (2008). Inhomogeneous precipitation distribution and snow transport in steep terrain. *Water Resources Research*, 44(7). <https://doi.org/10.1029/2007WR006545>
- Lehning, M., Völsch, I., Gustafsson, D., Nguyen, T. A., Stähli, M., & Zappa, M. (2006a). Alpine3d: a detailed model of mountain surface processes and its application to snow hydrology.

Bibliography

- Hydrological Processes*, 20(10), 2111–2128. <https://doi.org/https://doi.org/10.1002/hyp.6204>
- Lehning, M., Völksch, I., Gustafsson, D., Nguyen, T. A., Stähli, M., & Zappa, M. (2006b). Alpine3d: a detailed model of mountain surface processes and its application to snow hydrology. *Hydrological Processes*, 20(10), 2111–2128. <https://doi.org/https://doi.org/10.1002/hyp.6204>
- Liston, G., & Sturm, M. (2004). The role of winter sublimation in the Arctic moisture budget. *Hydrology Research*, 35(4-5), 325–334. <https://doi.org/10.2166/nh.2004.0024>
- Liston, G. E., & Elder, K. (2006a). A distributed snow-evolution modeling system (snowmodel). *Journal of Hydrometeorology*, 7(6), 1259–1276. <https://doi.org/https://doi.org/10.1175/JHM548.1>
- Liston, G. E., & Elder, K. (2006b). A meteorological distribution system for high-resolution terrestrial modeling (micromet). *Journal of Hydrometeorology*, 7(2), 217–234. <https://doi.org/10.1175/JHM486.1>
- Liston, G. E., Haehnel, R. B., Sturm, M., Hiemstra, C. A., Berezovskaya, S., & Tabler, R. D. (2007). Simulating complex snow distributions in windy environments using snowtran-3d. *Journal of Glaciology*, 53(181), 241–256. <https://doi.org/10.3189/172756507782202865>
- Liu, C., Ikeda, K., Thompson, G., Rasmussen, R., & Dudhia, J. (2011). High-resolution simulations of wintertime precipitation in the colorado headwaters region: sensitivity to physics parameterizations. *Monthly Weather Review*, 139(11), 3533–3553. <https://doi.org/10.1175/MWR-D-11-00009.1>
- Luce, C. H., Tarboton, D. G., & Cooley, K. R. (1998). The influence of the spatial distribution of snow on basin-averaged snowmelt. *Hydrological Processes*, 12(10-11), 1671–1683. [https://doi.org/https://doi.org/10.1002/\(SICI\)1099-1085\(199808/09\)12:10/11<1671::AID-HYP688>3.0.CO;2-N](https://doi.org/https://doi.org/10.1002/(SICI)1099-1085(199808/09)12:10/11<1671::AID-HYP688>3.0.CO;2-N)
- Lundquist, J., Hughes, M., Gutmann, E., & Kapnick, S. (2019). Our skill in modeling mountain rain and snow is bypassing the skill of our observational networks. *Bulletin of the American Meteorological Society*, 100(12), 2473–2490. <https://doi.org/10.1175/BAMS-D-19-0001.1>
- Lundquist, J. D., & Dettinger, M. D. (2005). How snowpack heterogeneity affects diurnal streamflow timing. *Water Resources Research*, 41(5). <https://doi.org/https://doi.org/10.1029/2004WR003649>
- Lundquist, J. D., Minder, J. R., Neiman, P. J., & Sukovich, E. (2010). Relationships between barrier jet heights, orographic precipitation gradients, and streamflow in the northern sierra nevada. *Journal of Hydrometeorology*, 11(5), 1141–1156. <https://doi.org/10.1175/2010JHM1264.1>
- Lundquist, K. A., Chow, F. K., & Lundquist, J. K. (2012). An immersed boundary method enabling large-eddy simulations of flow over complex terrain in the wrf model. *Monthly Weather Review*, 140(12), 3936–3955. <https://doi.org/10.1175/MWR-D-11-00311.1>
- Magnusson, J., Eisner, S., Huang, S., Lussana, C., Mazzotti, G., Essery, R., Saloranta, T., & Beldring, S. (2019). Influence of spatial resolution on snow cover dynamics for a

- coastal and mountainous region at high latitudes (norway). *Water Resources Research*, 55(7), 5612–5630. <https://doi.org/https://doi.org/10.1029/2019WR024925>
- Magnusson, J., Gustafsson, D., Hüsler, F., & Jonas, T. (2014). Assimilation of point swe data into a distributed snow cover model comparing two contrasting methods. *Water Resources Research*, 50(10), 7816–7835. <https://doi.org/10.1002/2014WR015302>
- Magnusson, J., Wever, N., Essery, R., Helbig, N., Winstral, A., & Jonas, T. (2015). Evaluating snow models with varying process representations for hydrological applications. *Water Resources Research*, 51(4), 2707–2723. <https://doi.org/https://doi.org/10.1002/2014WR016498>
- Marks, D., Winstral, A., & Seyfried, M. (2002). Simulation of terrain and forest shelter effects on patterns of snow deposition, snowmelt and runoff over a semi-arid mountain catchment. *Hydrological Processes*, 16(18), 3605–3626. <https://doi.org/10.1002/hyp.1237>
- Marsh, C. B., Pomeroy, J. W., Spiteri, R. J., & Wheeler, H. S. (2020). A finite volume blowing snow model for use with variable resolution meshes [e2019WR025307 2019WR025307]. *Water Resources Research*, 56(2), e2019WR025307. <https://doi.org/https://doi.org/10.1029/2019WR025307>
- Marsh, C. B., Vionnet, V., & Pomeroy, J. W. (2023). Windmapper: an efficient wind down-scaling method for hydrological models [e2022WR032683 2022WR032683]. *Water Resources Research*, 59(3), e2022WR032683. <https://doi.org/https://doi.org/10.1029/2022WR032683>
- Martin, E., & Lejeune, Y. (1998). Turbulent fluxes above the snow surface. *Annals of Glaciology*, 26, 179–183. <https://doi.org/10.3189/1998AoG26-1-179-183>
- Matthews, T., Perry, L. B., Koch, I., Aryal, D., Khadka, A., Shrestha, D., Abernathy, K., Elmore, A. C., Seimon, A., Tait, A., Elvin, S., Tuladhar, S., Baidya, S. K., Potocki, M., Birkel, S. D., Kang, S., Sherpa, T. C., Gajurel, A., & Mayewski, P. A. (2020). Going to extremes: installing the world's highest weather stations on mount everest. *Bulletin of the American Meteorological Society*, 101(11), E1870–E1890. <https://doi.org/10.1175/BAMS-D-19-0198.1>
- Mazzotti, G., Essery, R., Moeser, C. D., & Jonas, T. (2020). Resolving small-scale forest snow patterns using an energy balance snow model with a one-layer canopy [e2019WR026129 2019WR026129]. *Water Resources Research*, 56(1), e2019WR026129. <https://doi.org/https://doi.org/10.1029/2019WR026129>
- Mazzotti, G., Essery, R., Webster, C., Malle, J., & Jonas, T. (2020). Process-level evaluation of a hyper-resolution forest snow model using distributed multisensor observations [e2020WR027572 2020WR027572]. *Water Resources Research*, 56(9), e2020WR027572. <https://doi.org/https://doi.org/10.1029/2020WR027572>
- McFarquhar, G. M., Zhang, H., Heymsfield, G., Halverson, J. B., Hood, R., Dudhia, J., & Marks, F. (2006). Factors affecting the evolution of hurricane erin (2001) and the distributions of hydrometeors: role of microphysical processes. *Journal of the Atmospheric Sciences*, 63(1), 127–150. <https://doi.org/10.1175/JAS3590.1>

Bibliography

- Melo, D. B., Sharma, V., Comola, F., Sigmund, A., & Lehning, M. (2022). Modeling snow saltation: the effect of grain size and interparticle cohesion [e2021JD035260 2021JD035260]. *Journal of Geophysical Research: Atmospheres*, *127*(1), e2021JD035260. <https://doi.org/https://doi.org/10.1029/2021JD035260>
- Melo, D. B., Sigmund, A., & Lehning, M. (2023). Understanding snow saltation parameterizations: lessons from theory, experiments and numerical simulations. *EGU sphere*, *2023*, 1–37. <https://doi.org/10.5194/egusphere-2023-488>
- Ménard, C. B., Essery, R., Barr, A., Bartlett, P., Derry, J., Dumont, M., Fierz, C., Kim, H., Kontu, A., Lejeune, Y., Marks, D., Niwano, M., Raleigh, M., Wang, L., & Wever, N. (2019). Meteorological and evaluation datasets for snow modelling at 10 reference sites: description of in situ and bias-corrected reanalysis data. *Earth System Science Data*, *11*(2), 865–880. <https://doi.org/10.5194/essd-11-865-2019>
- Menke, R., Vasiljević, N., Mann, J., & Lundquist, J. K. (2019). Characterization of flow recirculation zones at the perdigão site using multi-lidar measurements. *Atmospheric Chemistry and Physics*, *19*(4), 2713–2723. <https://doi.org/10.5194/acp-19-2713-2019>
- MeteoCH. (2013). Meteoswiss: daily precipitation (final analysis): rhiresd [www.meteoswiss.admin.ch/content/dam/meteoswiss/de/].
- Michel, A., Sharma, V., Lehning, M., & Huwald, H. (2021). Climate change scenarios at hourly time-step over switzerland from an enhanced temporal downscaling approach. *International Journal of Climatology*, *41*(6), 3503–3522. <https://doi.org/https://doi.org/10.1002/joc.7032>
- Mitchell, D. L. (1996). Use of mass- and area-dimensional power laws for determining precipitation particle terminal velocities. *Journal of Atmospheric Sciences*, *53*(12), 1710–1723. [https://doi.org/10.1175/1520-0469\(1996\)053<1710:UOMAAD>2.0.CO;2](https://doi.org/10.1175/1520-0469(1996)053<1710:UOMAAD>2.0.CO;2)
- Morrison, H., Curry, J. A., & Khvorostyanov, V. I. (2005). A new double-moment microphysics parameterization for application in cloud and climate models. part i: description. *Journal of the Atmospheric Sciences*, *62*(6), 1665–1677. <https://doi.org/10.1175/JAS3446.1>
- Morrison, H., Thompson, G., & Tatarskii, V. (2009). Impact of cloud microphysics on the development of trailing stratiform precipitation in a simulated squall line: comparison of one- and two-moment schemes. *Monthly Weather Review*, *137*(3), 991–1007. <https://doi.org/10.1175/2008MWR2556.1>
- Morrison, H., & Milbrandt, J. A. (2015). Parameterization of cloud microphysics based on the prediction of bulk ice particle properties. part i: scheme description and idealized tests. *Journal of the Atmospheric Sciences*, *72*(1), 287–311. <https://doi.org/10.1175/JAS-D-14-0065.1>
- Mott, R., Schirmer, M., Bavay, M., Grünewald, T., & Lehning, M. (2010a). Understanding snow-transport processes shaping the mountain snow-cover. *The Cryosphere*, *4*(4), 545–559. <https://doi.org/10.5194/tc-4-545-2010>
- Mott, R., Schirmer, M., Bavay, M., Grünewald, T., & Lehning, M. (2010b). Understanding snow-transport processes shaping the mountain snow-cover. *The Cryosphere*, *4*(4), 545–559. <https://doi.org/10.5194/tc-4-545-2010>

- Mott, R., Schirmer, M., & Lehning, M. (2011). Scaling properties of wind and snow depth distribution in an alpine catchment. *Journal of Geophysical Research: Atmospheres*, *116*(D6). <https://doi.org/https://doi.org/10.1029/2010JD014886>
- Mott, R., Scipión, D., Schneebeli, M., Dawes, N., Berne, A., & Lehning, M. (2014). Orographic effects on snow deposition patterns in mountainous terrain. *Journal of Geophysical Research: Atmospheres*, *119*(3), 1419–1439. <https://doi.org/10.1002/2013JD019880>
- Mott, R., Stiperski, I., & Nicholson, L. (2020). Spatio-temporal flow variations driving heat exchange processes at a mountain glacier. *The Cryosphere*, *14*(12), 4699–4718. <https://doi.org/10.5194/tc-14-4699-2020>
- Mott, R., & Lehning, M. (2010). Meteorological modeling of very high-resolution wind fields and snow deposition for mountains. *Journal of Hydrometeorology*, *11*(4), 934–949. <https://doi.org/10.1175/2010JHM1216.1>
- Mott, R., Vionnet, V., & Grünewald, T. (2018). The seasonal snow cover dynamics: review on wind-driven coupling processes. *Frontiers in Earth Science*, *6*. <https://doi.org/10.3389/feart.2018.00197>
- Mott, R., Winstral, A., Cluzet, B., Helbig, N., Magnusson, J., Mazzotti, G., Quéno, L., Schirmer, M., Webster, C., & Jonas, T. (2023). Operational snow-hydrological modeling for Switzerland. *Frontiers in Earth Science*, *11*. <https://doi.org/10.3389/feart.2023.1228158>
- Moussiopoulos, N., Flassak, T., & Knittel, G. (1988). A refined diagnostic wind model. *Environmental Software*, *3*(2), 85–94. [https://doi.org/10.1016/0266-9838\(88\)90015-9](https://doi.org/10.1016/0266-9838(88)90015-9)
- Mower, R., Gutmann, E. D., Lundquist, J., Liston, G. E., & Rasmussen, S. (2023). Parallel snow-model (v1.0): a parallel implementation of a distributed snow-evolution modeling system (snowmodel). *EGU Sphere*, *2023*, 1–27. <https://doi.org/10.5194/egusphere-2023-1612>
- Musselman, K. N., Pomeroy, J. W., Essery, R. L. H., & Leroux, N. (2015). Impact of windflow calculations on simulations of alpine snow accumulation, redistribution and ablation. *Hydrological Processes*, *29*(18), 3983–3999. <https://doi.org/https://doi.org/10.1002/hyp.10595>
- Nijssen, B., Bowling, L. C., Lettenmaier, D. P., Clark, D. B., El Maayar, M., Essery, R., Goers, S., Gusev, Y. M., Habets, F., van den Hurk, B., Jin, J., Kahan, D., Lohmann, D., Ma, X., Mahanama, S., Mocko, D., Nasonova, O., Niu, G.-Y., Samuelsson, P., ... Yang, Z.-L. (2003). Simulation of high latitude hydrological processes in the torne–kalix basin: pilps phase 2(e): 2: comparison of model results with observations [Project for Intercomparison of Land-surface Parameterization Schemes, Phase 2(e)]. *Global and Planetary Change*, *38*(1), 31–53. [https://doi.org/https://doi.org/10.1016/S0921-8181\(03\)00004-3](https://doi.org/https://doi.org/10.1016/S0921-8181(03)00004-3)
- Niu, G.-Y., Yang, Z.-L., Mitchell, K. E., Chen, F., Ek, M. B., Barlage, M., Kumar, A., Manning, K., Niyogi, D., Rosero, E., Tewari, M., & Xia, Y. (2011). The community noah land surface model with multiparameterization options (noah-mp): 1. model description and evaluation with local-scale measurements. *Journal of Geophysical Research: Atmospheres*, *116*(D12). <https://doi.org/https://doi.org/10.1029/2010JD015139>
- O'Brien, J. J. (1970). Alternative solutions to the classical vertical velocity problem. *Journal of Applied Meteorology and Climatology*, *9*(2), 197–203.

Bibliography

- Oerlemans, J., & Grisogono, B. (2002). Glacier winds and parameterisation of the related surface heat fluxes. *Tellus A: Dynamic Meteorology and Oceanography*, 54(5), 440–452. <https://doi.org/10.3402/tellusa.v54i5.12164>
- Ohmura, A. (2001). Physical basis for the temperature-based melt-index method. *Journal of Applied Meteorology*, 40(4), 753–761. [https://doi.org/10.1175/1520-0450\(2001\)040<0753:PBFTTB>2.0.CO;2](https://doi.org/10.1175/1520-0450(2001)040<0753:PBFTTB>2.0.CO;2)
- Painter, T. H., Berisford, D. F., Boardman, J. W., Bormann, K. J., Deems, J. S., Gehrke, F., Hedrick, A., Joyce, M., Laidlaw, R., Marks, D., Mattmann, C., McGurk, B., Ramirez, P., Richardson, M., Skiles, S. M., Seidel, F. C., & Winstral, A. (2016). The airborne snow observatory: fusion of scanning lidar, imaging spectrometer, and physically-based modeling for mapping snow water equivalent and snow albedo. *Remote Sensing of Environment*, 184, 139–152. <https://doi.org/https://doi.org/10.1016/j.rse.2016.06.018>
- Phillips, N. A. (1956). The general circulation of the atmosphere: a numerical experiment. *Quarterly Journal of the Royal Meteorological Society*, 82(352), 123–164. <https://doi.org/https://doi.org/10.1002/qj.49708235202>
- Picard, G., Arnaud, L., Caneill, R., Lefebvre, E., & Lamare, M. (2019). Observation of the process of snow accumulation on the antarctic plateau by time lapse laser scanning. *The Cryosphere*, 13(7), 1983–1999. <https://doi.org/10.5194/tc-13-1983-2019>
- Pomeroy, J., Brown, T., Fang, X., Shook, K., Pradhananga, D., Armstrong, R., Harder, P., Marsh, C., Costa, D., Krogh, S., Aubry-Wake, C., Annand, H., Lawford, P., He, Z., Kompanizare, M., & Lopez Moreno, J. (2022). The cold regions hydrological modelling platform for hydrological diagnosis and prediction based on process understanding. *Journal of Hydrology*, 615, 128711. <https://doi.org/https://doi.org/10.1016/j.jhydrol.2022.128711>
- Prandtl, L. (1942). *Führer durch die strömungslehre*. Vieweg und Sohn.
- Prein, A. F., Holland, G. J., Rasmussen, R. M., Done, J., Ikeda, K., Clark, M. P., & Liu, C. H. (2013). Importance of regional climate model grid spacing for the simulation of heavy precipitation in the colorado headwaters. *Journal of Climate*, 26(13), 4848–4857. <https://doi.org/10.1175/JCLI-D-12-00727.1>
- Prein, A. F., Langhans, W., Fosser, G., Ferrone, A., Ban, N., Goergen, K., Keller, M., Tölle, M., Gutjahr, O., Feser, F., Brisson, E., Kollet, S., Schmidli, J., van Lipzig, N. P. M., & Leung, R. (2015). A review on regional convection-permitting climate modeling: demonstrations, prospects, and challenges. *Reviews of Geophysics*, 53(2), 323–361. <https://doi.org/10.1002/2014RG000475>
- Quéno, L., Mott, R., Morin, P., Cluzet, B., Mazzotti, G., & Jonas, T. (2023). Snow redistribution in an intermediate-complexity snow hydrology modelling framework. *EGUsphere*, 2023, 1–32. <https://doi.org/10.5194/egusphere-2023-2071>
- Raderschall, N., Lehning, M., & Schär, C. (2008). Fine-scale modeling of the boundary layer wind field over steep topography. *Water Resources Research*, 44(9). <https://doi.org/10.1029/2007WR006544>
- Raleigh, M. S., Lundquist, J. D., & Clark, M. P. (2015). Exploring the impact of forcing error characteristics on physically based snow simulations within a global sensitivity

- analysis framework. *Hydrology and Earth System Sciences*, 19(7), 3153–3179. <https://doi.org/10.5194/hess-19-3153-2015>
- Rasmussen, R., Baker, B., Kochendorfer, J., Meyers, T., Landolt, S., Fischer, A. P., Black, J., Thériault, J. M., Kucera, P., Gochis, D., Smith, C., Nitu, R., Hall, M., Ikeda, K., & Gutmann, E. (2012). How well are we measuring snow: the noaa/faa/ncar winter precipitation test bed. *Bulletin of the American Meteorological Society*, 93(6), 811–829. <https://doi.org/10.1175/BAMS-D-11-00052.1>
- Rasmussen, S., Gutmann, E., Friesen, B., Rouson, D., Filippone, S., & Moulitsas, I. (2018). Development and performance comparison of mpi and fortran coarrays within an atmospheric research model.
- Ratto, C., Festa, R., Romeo, C., Frumento, O., & Galluzzi, M. (1994). Mass-consistent models for wind fields over complex terrain: the state of the art. *Environmental Software*, 9(4), 247–268. [https://doi.org/10.1016/0266-9838\(94\)90023-X](https://doi.org/10.1016/0266-9838(94)90023-X)
- Reynolds, D., Gutmann, E., Kruyt, B., Haugeneder, M., Jonas, T., Gerber, F., Lehning, M., & Mott, R. (2023). The high-resolution intermediate complexity atmospheric research (hicar v1.1) model enables fast dynamic downscaling to the hectometer scale. *Geoscientific Model Development*, 16(17), 5049–5068. <https://doi.org/10.5194/gmd-16-5049-2023>
- Reynolds, D., Haugeneder, M., Lehning, M., & Mott, R. (2024, in prep). Near-surface atmospheric forcing data in complex terrain: observations and improvement of an intermediate complexity atmospheric model.
- Reynolds, D. S., Pflug, J. M., & Lundquist, J. D. (2021). Evaluating wind fields for use in basin-scale distributed snow models [e2020WR028536 2020WR028536]. *Water Resources Research*, 57(2), e2020WR028536. <https://doi.org/10.1029/2020WR028536>
- RGI Consortium, . (2017). Randolph glacier inventory - a dataset of global glacier outlines, version 6. <https://doi.org/10.7265/4m1f-gd79>
- Ross, D. G., & Fox, D. G. (1991). Evaluation of an air pollution analysis system for complex terrain. *Journal of Applied Meteorology and Climatology*, 30(7), 909–923. [https://doi.org/10.1175/1520-0450\(1991\)030<0909:EOAAPA>2.0.CO;2](https://doi.org/10.1175/1520-0450(1991)030<0909:EOAAPA>2.0.CO;2)
- Ross, D. G., Smith, I. N., Manins, P. C., & Fox, D. G. (1988). Diagnostic wind field modeling for complex terrain: model development and testing. *Journal of Applied Meteorology (1988-2005)*, 27(7), 785–796. Retrieved December 12, 2022, from <http://www.jstor.org/stable/26183717>
- Saigger, M., Sauter, T., Schmid, C., Collier, E., Goger, B., Kaser, G., Prinz, R., Voordendag, A., & Mölg, T. (2023). Snowdrift scheme in the weather research and forecasting model. <https://doi.org/10.22541/essoar.169755043.33054646/v1>
- Sasaki, Y. (1958). An objective analysis based on the variational method. 36(3), 77–88. https://doi.org/10.2151/jmsj1923.36.3_77
- Sauter, T., Arndt, A., & Schneider, C. (2020). Cosipy v1.3 – an open-source coupled snowpack and ice surface energy and mass balance model. *Geoscientific Model Development*, 13(11), 5645–5662. <https://doi.org/10.5194/gmd-13-5645-2020>

Bibliography

- Sauter, T., & Galos, S. P. (2016). Effects of local advection on the spatial sensible heat flux variation on a mountain glacier. *The Cryosphere*, 10(6), 2887–2905. <https://doi.org/10.5194/tc-10-2887-2016>
- Schär, C., Leuenberger, D., Fuhrer, O., Lüthi, D., & Girard, C. (2002). A new terrain-following vertical coordinate formulation for atmospheric prediction models. *Monthly Weather Review*, 130(10), 2459–2480. [https://doi.org/10.1175/1520-0493\(2002\)130<2459:ANTFVC>2.0.CO;2](https://doi.org/10.1175/1520-0493(2002)130<2459:ANTFVC>2.0.CO;2)
- Schlögl, S., Marty, C., Bavay, M., & Lehning, M. (2016). Sensitivity of alpine3d modeled snow cover to modifications in dem resolution, station coverage and meteorological input quantities. *Environmental Modelling & Software*, 83, 387–396. <https://doi.org/https://doi.org/10.1016/j.envsoft.2016.02.017>
- Schlögl, S., Lehning, M., & Mott, R. (2018). How are turbulent sensible heat fluxes and snow melt rates affected by a changing snow cover fraction? *Frontiers in Earth Science*, 6. <https://doi.org/10.3389/feart.2018.00154>
- Schlögl, S., Lehning, M., Nishimura, K., Huwald, H., Cullen, N. J., & Mott, R. (2017). How do Stability Corrections Perform in the Stable Boundary Layer Over Snow? *Boundary-Layer Meteorol*, 165(1), 161–180. <https://doi.org/10.1007/s10546-017-0262-1>
- Schumann, U. (1990). Large-eddy simulation of the up-slope boundary layer. *Quarterly Journal of the Royal Meteorological Society*, 116(493), 637–670. <https://doi.org/https://doi.org/10.1002/qj.49711649307>
- Seifert, A., Baldauf, M., Stephan, K., Blahak, U., & Beheng, K. (2008). The challenge of convective-scale quantitative precipitation forecasting.
- Seity, Y., Brousseau, P., Malardel, S., Hello, G., Bénard, P., Bouttier, F., Lac, C., & Masson, V. (2011). The arôme-france convective-scale operational model. *Monthly Weather Review*, 139(3), 976–991. <https://doi.org/10.1175/2010MWR3425.1>
- Sexstone, G. A., Clow, D. W., Fassnacht, S. R., Liston, G. E., Hiemstra, C. A., Knowles, J. F., & Penn, C. A. (2018). Snow sublimation in mountain environments and its sensitivity to forest disturbance and climate warming. *Water Resources Research*, 54(2), 1191–1211. <https://doi.org/https://doi.org/10.1002/2017WR021172>
- Sharma, V., Gerber, F., & Lehning, M. (2023). Introducing cryowrf v1.0: multiscale atmospheric flow simulations with advanced snow cover modelling. *Geoscientific Model Development*, 16(2), 719–749. <https://doi.org/10.5194/gmd-16-719-2023>
- Sherman, C. A. (1978). A mass-consistent model for wind fields over complex terrain. *Journal of Applied Meteorology and Climatology*, 17(3), 312–319. [https://doi.org/10.1175/1520-0450\(1978\)017<0312:AMCMFW>2.0.CO;2](https://doi.org/10.1175/1520-0450(1978)017<0312:AMCMFW>2.0.CO;2)
- Shin, H. H., & Hong, S.-Y. (2015). Representation of the subgrid-scale turbulent transport in convective boundary layers at gray-zone resolutions. *Monthly Weather Review*, 143(1), 250–271. <https://doi.org/https://doi.org/10.1175/MWR-D-14-00116.1>
- Sigmund, A., Dujardin, J., Comola, F., Sharma, V., Huwald, H., Melo, D. B., Hirasawa, N., Nishimura, K., & Lehning, M. (2022). Evidence of strong flux underestimation by bulk parametrizations during drifting and blowing snow. *Boundary-Layer Meteorology*, 182(1), 119–146. <https://doi.org/10.1007/s10546-021-00653-x>

- Skamarock, W. C., Klemp, J. B., Dudhia, J., Gill, D. O., Barker, D., & Duda, J. G., M. G. . . . Powers. (2008). A description of the advanced research wrf version 3. *University Corporation for Atmospheric Research*. <https://doi.org/10.5065/D68S4MVH>
- Skamarock, W. C., Klemp, J. B., Duda, M. G., Fowler, L. D., Park, S.-H., & Ringler, T. D. (2012). A multiscale nonhydrostatic atmospheric model using centroidal voronoi tessellations and c-grid staggering. *Monthly Weather Review*, *140*(9), 3090–3105. <https://doi.org/10.1175/MWR-D-11-00215.1>
- Smith, R. B. (1979). The influence of mountains on the atmosphere. *Advances in Geophysics*, *21*, 87–230.
- Smith, R. B., & Barstad, I. (2004). A linear theory of orographic precipitation. *Journal of the Atmospheric Sciences*, *61*(12), 1377–1391. [https://doi.org/10.1175/1520-0469\(2004\)061<1377:ALTOOP>2.0.CO;2](https://doi.org/10.1175/1520-0469(2004)061<1377:ALTOOP>2.0.CO;2)
- Sommer, C. G., Lehning, M., & Fierz, C. (2017). Wind tunnel experiments: saltation is necessary for wind-packing. *Journal of Glaciology*, *63*(242), 950–958. <https://doi.org/10.1017/jog.2017.53>
- Sommer, C. G., Lehning, M., & Mott, R. (2015). Snow in a very steep rock face: accumulation and redistribution during and after a snowfall event. *Frontiers in Earth Science*, *3*. <https://doi.org/10.3389/feart.2015.00073>
- Sovilla, B., Burlando, P., & Bartelt, P. (2006). Field experiments and numerical modeling of mass entrainment in snow avalanches. *Journal of Geophysical Research: Earth Surface*, *111*(F3). <https://doi.org/https://doi.org/10.1029/2005JF000391>
- Spacesystems, N., & Team, U. A. S. (2019). Aster global digital elevation model v003, nasa eosdis land processes daac [distributed by NASA EOSDIS Land Processes DAAC].
- Spinoni, J., Vogt, J. V., Naumann, G., Barbosa, P., & Dosio, A. (2018). Will drought events become more frequent and severe in europe? *International Journal of Climatology*, *38*(4), 1718–1736. <https://doi.org/10.1002/joc.5291>
- Steger, C. R., Steger, B., & Schär, C. (2022). Horayzon v1.2: an efficient and flexible ray-tracing algorithm to compute horizon and sky view factor. *Geoscientific Model Development*, *15*(17), 6817–6840. <https://doi.org/10.5194/gmd-15-6817-2022>
- Strasser, U., Bernhardt, M., Weber, M., Liston, G. E., & Mauser, W. (2008). Is snow sublimation important in the alpine water balance? *The Cryosphere*, *2*(1), 53–66. <https://doi.org/10.5194/tc-2-53-2008>
- Sturm, M., Goldstein, M. A., & Parr, C. (2017). Water and life from snow: a trillion dollar science question. *Water Resources Research*, *53*(5), 3534–3544. <https://doi.org/https://doi.org/10.1002/2017WR020840>
- Sturm, M., & Stuefer, S. (2013). Wind-blown flux rates derived from drifts at arctic snow fences. *Journal of Glaciology*, *59*(213), 21–34. <https://doi.org/10.3189/2013JoG12J110>
- Thompson, G., Tewari, M., Ikeda, K., Tessorof, S., Weeks, C., Otkin, J., & Kong, F. (2016). Explicitly-coupled cloud physics and radiation parameterizations and subsequent evaluation in wrf high-resolution convective forecasts. *Atmospheric Research*, *168*, 92–104. <https://doi.org/10.1016/j.atmosres.2015.09.005>

Bibliography

- Umek, L., Gohm, A., Haid, M., Ward, H. C., & Rotach, M. W. (2021). Large-eddy simulation of foehn–cold pool interactions in the inn valley during piano iop 2. *Quarterly Journal of the Royal Meteorological Society*, *147*(735), 944–982. <https://doi.org/10.1002/qj.3954>
- Vionnet, V., Brun, E., Morin, S., Boone, A., Faroux, S., Le Moigne, P., Martin, E., & Willemet, J.-M. (2012). The detailed snowpack scheme crocus and its implementation in surfex v7.2. *Geoscientific Model Development*, *5*(3), 773–791. <https://doi.org/10.5194/gmd-5-773-2012>
- Vionnet, V., Marsh, C. B., Menounos, B., Gascoïn, S., Wayand, N. E., Shea, J., Mukherjee, K., & Pomeroy, J. W. (2021). Multi-scale snowdrift-permitting modelling of mountain snowpack. *The Cryosphere*, *15*(2), 743–769. <https://doi.org/10.5194/tc-15-743-2021>
- Vionnet, V., Martin, E., Masson, V., Guyomarc'h, G., Naaim-Bouvet, F., Prokop, A., Durand, Y., & Lac, C. (2014). Simulation of wind-induced snow transport and sublimation in alpine terrain using a fully coupled snowpack/atmosphere model. *The Cryosphere*, *8*(2), 395–415. <https://doi.org/10.5194/tc-8-395-2014>
- Vionnet, V., Verville, M., Fortin, V., Brugman, M., Abrahamowicz, M., Lemay, F., Thériault, J. M., Lafaysse, M., & Milbrandt, J. A. (2022). Snow level from post-processing of atmospheric model improves snowfall estimate and snowpack prediction in mountains [e2021WR031778 2021WR031778]. *Water Resources Research*, *58*(12), e2021WR031778. <https://doi.org/10.1029/2021WR031778>
- Vionnet, V., Martin, E., Masson, V., Lac, C., Naaim Bouvet, F., & Guyomarc'h, G. (2017). High-resolution large eddy simulation of snow accumulation in alpine terrain. *Journal of Geophysical Research: Atmospheres*, *122*(20), 11,005–11,021. <https://doi.org/10.1002/2017JD026947>
- Viviroli, D., Dürr, H. H., Messerli, B., Meybeck, M., & Weingartner, R. (2007). Mountains of the world, water towers for humanity: typology, mapping, and global significance. *Water Resources Research*, *43*(7). <https://doi.org/10.1029/2006WR005653>
- Voordendag, A., Goger, B., Prinz, R., Sauter, T., Mölg, T., Saigger, M., & Kaser, G. (2023). Investigating wind-driven snow redistribution processes over an alpine glacier with high-resolution terrestrial laser scans and large-eddy simulations. *EGU sphere*, *2023*, 1–27. <https://doi.org/10.5194/egusphere-2023-1395>
- Voordendag, A., Réveillet, M., MacDonell, S., & Lhermitte, S. (2021). Snow model comparison to simulate snow depth evolution and sublimation at point scale in the semi-arid andes of chile. *The Cryosphere*, *15*(9), 4241–4259. <https://doi.org/10.5194/tc-15-4241-2021>
- Voordendag, A., Goger, B., Klug, C., Prinz, R., Rutzinger, M., Sauter, T., & Kaser, G. (2023). Uncertainty assessment of a permanent long-range terrestrial laser scanning system for the quantification of snow dynamics on hintereisferner (austria). *Frontiers in Earth Science*, *11*. <https://doi.org/10.3389/feart.2023.1085416>
- Wagenbrenner, N. S., Forthofer, J. M., Lamb, B. K., Shannon, K. S., & Butler, B. W. (2016). Downscaling surface wind predictions from numerical weather prediction models in complex terrain with windninja. *Atmospheric Chemistry and Physics*, *16*(8), 5229–5241. <https://doi.org/10.5194/acp-16-5229-2016>

- Wan, H., Giorgetta, M. A., Zängl, G., Restelli, M., Majewski, D., Bonaventura, L., Fröhlich, K., Reinert, D., Rípodas, P., Kornbluh, L., & Förstner, J. (2013). The icon-1.2 hydrostatic atmospheric dynamical core on triangular grids – part 1: formulation and performance of the baseline version. *Geoscientific Model Development*, 6(3), 735–763. <https://doi.org/10.5194/gmd-6-735-2013>
- Wang, H., Skamarock, W. C., & Feingold, G. (2009). Evaluation of scalar advection schemes in the advanced research wrf model using large-eddy simulations of aerosol–cloud interactions. *Monthly Weather Review*, 137(8), 2547–2558. <https://doi.org/10.1175/2009MWR2820.1>
- Wang, Z., & Huang, N. (2017). Numerical simulation of the falling snow deposition over complex terrain. *Journal of Geophysical Research: Atmospheres*, 122(2), 980–1000. <https://doi.org/10.1002/2016JD025316>
- Westerhuis, S., Fuhrer, O., Bhattacharya, R., Schmidli, J., & Bretherton, C. (2021). Effects of terrain-following vertical coordinates on simulation of stratus clouds in numerical weather prediction models. *Quarterly Journal of the Royal Meteorological Society*, 147(734), 94–105. <https://doi.org/10.1002/qj.3907>
- Wever, N., Keenan, E., Amory, C., Lehning, M., Sigmund, A., Huwald, H., & Lenaerts, J. T. M. (2023). Observations and simulations of new snow density in the drifting snow-dominated environment of antarctica. *Journal of Glaciology*, 69(276), 823–840. <https://doi.org/10.1017/jog.2022.102>
- Wicker, L. J., & Skamarock, W. C. (2002). Time-splitting methods for elastic models using forward time schemes. *Monthly Weather Review*, 130(8), 2088–2097. [https://doi.org/10.1175/1520-0493\(2002\)130<2088:TSMFEM>2.0.CO;2](https://doi.org/10.1175/1520-0493(2002)130<2088:TSMFEM>2.0.CO;2)
- Winstral, A., Jonas, T., & Helbig, N. (2017). Statistical downscaling of gridded wind speed data using local topography. *Journal of Hydrometeorology*, 18(2), 335–348. <https://doi.org/10.1175/JHM-D-16-0054.1>
- Winstral, A., & Marks, D. (2002). Simulating wind fields and snow redistribution using terrain-based parameters to model snow accumulation and melt over a semi-arid mountain catchment. *Hydrological Processes*, 16(18), 3585–3603. <https://doi.org/10.1002/hyp.1238>
- Winstral, A., Marks, D., & Gurney, R. (2013). Simulating wind-affected snow accumulations at catchment to basin scales [Snow–Atmosphere Interactions and Hydrological Consequences]. *Advances in Water Resources*, 55, 64–79. <https://doi.org/10.1016/j.advwatres.2012.08.011>
- Woods, C. P., Stoelinga, M. T., & Locatelli, J. D. (2007). The improve-1 storm of 1–2 february 2001. part iii: sensitivity of a mesoscale model simulation to the representation of snow particle types and testing of a bulk microphysical scheme with snow habit prediction. *Journal of the Atmospheric Sciences*, 64(11), 3927–3948. <https://doi.org/https://doi.org/10.1175/2007JAS2239.1>
- Wyngaard, J. C. (2004). Toward numerical modeling in the “terra incognita”. *Journal of the Atmospheric Sciences*, 61(14), 1816–1826. [https://doi.org/10.1175/1520-0469\(2004\)061<1816:TNMITT>2.0.CO;2](https://doi.org/10.1175/1520-0469(2004)061<1816:TNMITT>2.0.CO;2)

Bibliography

- Xie, Z., Hu, Z., Ma, Y., Sun, G., Gu, L., Liu, S., Wang, Y., Zheng, H., & Ma, W. (2019). Modeling blowing snow over the tibetan plateau with the community land model: method and preliminary evaluation. *Journal of Geophysical Research: Atmospheres*, *124*(16), 9332–9355. <https://doi.org/https://doi.org/10.1029/2019JD030684>
- Zängl, G. (2008). The temperature dependence of small-scale orographic precipitation enhancement. *Quarterly Journal of the Royal Meteorological Society*, *134*(634), 1167–1181. <https://doi.org/https://doi.org/10.1002/qj.267>
- Zardi, D., & Whiteman, C. D. (2013). Diurnal mountain wind systems. mountain weather research and forecasting: recent progress and current challenges.
- Zhong, S., & Whiteman, C. D. (2008). Downslope flows on a low-angle slope and their interactions with valley inversions. part ii: numerical modeling. *Journal of Applied Meteorology and Climatology*, *47*(7), 2039–2057. <https://doi.org/https://doi.org/10.1175/2007JAMC1670.1>
- Zhu, Y., & Newell, R. E. (1998). A proposed algorithm for moisture fluxes from atmospheric rivers. *Monthly Weather Review*, *126*(3), 725–735. [https://doi.org/10.1175/1520-0493\(1998\)126<0725:APAFMF>2.0.CO;2](https://doi.org/10.1175/1520-0493(1998)126<0725:APAFMF>2.0.CO;2)

Dylan Reynolds

Curriculum Vitae

Flüelastrasse 11
Davos Dorf, 7260
✉ dylan.reynolds@slf.ch
<https://github.com/d-reynolds>

Education

- 2020–2024 **PhD Student**, *Laboratory of Cryospheric Sciences*, EPFL, and WSL Institute for Snow and Avalanche Research SLF, Davos, supervised by Prof. Dr. Michael Lehning and advised by Dr. Rebecca Mott
- 2018–2019 **M.S. Civil and Environmental Engineering**, *University of Washington*, Seattle, WA
- Jan. 2018 **CUAHSI & iSWGR 4-day field-work course**, *Snow Measurement Field School*, Fraser, CO
- 2014–2018 **B.S. Civil and Environmental Engineering, Minor in Physics**, *University of Washington*, Seattle, WA

PhD Thesis

- title Snow-atmosphere modeling at seasonal time scales: Techniques developed and insights gained
- supervisors Prof. Dr. Michael Lehning, Dr. Rebecca Mott

Master's Thesis

- title Evaluating Distributed Wind Forcing Datasets Using Snow Depth Patterns
- supervisors Prof. Dr. Jessica D. Lundquist

Experience

Primary Work and Research Experience

- February. **Snow Hydrology Research Group, SLF, Research Scientist**, Davos, CH
- 2020–Present
- Improving the representation of snow-atmosphere processes in the an operational snow model
 - Quantifying the effects of preferential deposition of snowfall on flooding, water resources, and glacier mass balance
 - Advisor(s): Prof. Dr. Michael Lehning, Dr. Rebecca Mott
- Sept. 2018–
December. **Mountain Hydrology Research Group, CEE University of Washington, Graduate Student Research Assistant (RA)**, Seattle, WA
- 2019
- Using patterns in snow depth data to evaluation wind datasets for use in snow pack modeling
 - Comparison of distributed snow model output when forced with different wind products
 - Advisor(s): Prof. Dr. Jessica D. Lundquist

- May. **Mountain Hydrology Research Group, CEE University of Washington**, *Undergraduate Research Assistant (RA)*, Seattle, WA
 2017–Aug. 2018
- Comparison of snow density and snowpack stratigraphy at an open and forested site
 - Evaluation of different longwave radiation schemes (n=136) for use in hydrologic modeling in the Sierra Nevada
 - Analysis of precipitation patterns from different microphysical schemes in the WRF model
 - Advisor(s): Prof. Dr. Jessica D. Lundquist
- April. **Watershed Science and Engineering**, *Hydrologic Modeling Intern*, Seattle, WA
 2018–June. 2018
- Setup and calibrated the Distributed Hydrologic Soil and Vegetation Model (DHSVM) for the Chehalis River basin to model effects of dam installation
- Jan. **Wind Tunnel Technician**, *Kirstin Wind Tunnel*, Seattle, WA
 2017–Jan. 2018
- Worked as part of a 3-person crew to operate a wind tunnel for research and private testing
 - Experience included management and processing of data, and working with clients to build test programs for evaluation of aerodynamic design
- Summer 2016 **Aeronautics Research Intern**, *Amazon Prime Air*, Seattle, WA
- Determination of the thrust generated by a quadcopter due to the ground affect when landing
- Teaching**
- Winter 2021 & Winter 2022 **Physics and Chemistry of the Atmosphere**, *Teaching Assistant*, Lausanne, CH
- Other Relevant Research and Field Experience**
- Aug. 2018 & Aug. 2019 **Yosemite Hydroclimate Network**, *Field Technician*, Yosemite NP, CA
- Collection of streamflow data for the creation of rating curves using Bayesian statistics
 - Maintenance of existing meteorological towers
- Summer 2015 **Summer Undergraduate Researcher**, *Washington NASA Space Grant*, Seattle, WA
- Wrote and calibrated a script to estimate sublimation of CO₂ ice on the asteroid Ceres in support of NASA's Dawn mission
 - Advisor(s): Dr. Stephen E. Wood

Publications

Published

- 2024 – [6] Haugeneder, M., Lehning, M., Stiperski, I. et al. Turbulence in the Strongly Heterogeneous Near-Surface Boundary Layer over Patchy Snow. *Boundary-Layer Meteorol* 190, 7 (2024). <https://doi.org/10.1007/s10546-023-00856-4>
- 2023 – [5] **Reynolds, D.**, Gutmann, E., Kruyt, B., Haugeneder, M., Jonas, T., Gerber, F., Lehning, M., and Mott, R.: The High-resolution Intermediate Complexity Atmospheric Research (HICAR v1.1) model enables fast dynamic downscaling to the hectometer scale, *Geosci. Model Dev.*, 16, 5049–5068, <https://doi.org/10.5194/gmd-16-5049-2023>, 2023.

- [4] Haugeneder, M., Lehning, M., **Reynolds, D.** et al. A Novel Method to Quantify Near-Surface Boundary-Layer Dynamics at Ultra-High Spatio-Temporal Resolution. *Boundary-Layer Meteorol* 186, 177–197 (2023). <https://doi.org/10.1007/s10546-022-00752-3>
- 2022 – [3] Kruyt B, Mott R, Fiddes J, Gerber F, Sharma V and **Reynolds D** (2022) A Downscaling Intercomparison Study: The Representation of Slope- and Ridge-Scale Processes in Models of Different Complexity. *Front. Earth Sci.* 10:789332. doi: 10.3389/feart.2022.789332
- 2021 – [2] Lundquist, J. D., Dickerson-Lange, S., Gutmann, E., Jonas, T., Lumbrazo, C., & **Reynolds, D.** (2021). Snow interception modelling: Isolated observations have led to many land surface models lacking appropriate temperature sensitivities. *Hydrological Processes*, 35(7), e14274. <https://doi.org/10.1002/hyp.14274>
- [1] **Reynolds, D.**, Pflug, J. M., & Lundquist, J. D. (2020). Evaluating wind fields for use in basin-scale distributed snow models. *Water Resources Research*, 57, e2020WR028536. <https://doi.org/10.1029/2020WR028536>
- Submitted
- [-] **Reynolds, D.**, Quéno, L., Jafari, M., Berg, J., Haugeneder, M., Lehning, M., Mott, M. (2024). Seasonal Snow-Atmosphere Modeling: Let's do it
- [-] **Reynolds, D.**, Haugeneder, M., Lehning, M., Mott, M. (2024). Intermediate Complexity Atmospheric Modeling in Complex Terrain: Is it Right?

Conferences

Oral

- Jan. 2024 **4th International Conference on Snow Hydrology**, Grenoble, France
 “A coupled atmosphere-snow model system for operational snow hydrological modelling”
Reynolds, D., Quéno, L., Berg, J., Jafari, M., Haugeneder, H., Jonas, T., Lehning, M., Mott, R.
- July 2023 **38th General Assembly of the International Union of Geodesy and Geophysics**, Berlin, Germany
 “Validation of a novel high-resolution atmospheric model and its application to seasonal snowcover modeling”
Reynolds, D., Haugeneder, H., Berg, J., Lehning, M., Mott, R.
- Sept. 2022 **International Symposium on Snow**, Davos, CH
 “Explicitly resolving high-resolution, ridge-scale snow deposition patterns over long time periods”
Reynolds, D., Haugeneder, H., Lehning, M., Mott, R.
- Sept. 2022 **International Mountain Conference**, Innsbruck, Austria
 “HICAR: An Intermediate-Complexity Atmospheric Model Capable Of Resolving Ridge-Scale Snow Deposition Processes Over Large Mountain Ranges.”
Reynolds, D., Kruyt, B., Gutmann, E., Jonas, T., Lehning, M., Mott, R.

- May 2022 **EGU General Assembly**, Vienna, Austria
 “HICAR: An Intermediate-Complexity Atmospheric Model Capable Of Resolving Ridge-Scale Snow Deposition Processes Over Large Mountain Ranges.”
Reynolds, D., Kruyt, B., Gutmann, E., Jonas, T., Lehning, M., Mott, R.
- April 2019 **87th Annual Western Snow Conference**, Reno, NV
 “Automated detection of wind patterns in LiDAR snow depth data.”
Reynolds, D., Lundquist, J.
- Posters
- Dec. 2019 **AGU Fall Meeting 2019**, San Francisco, CA
 “Evaluating downscaled wind data using snow depth patterns.”
Reynolds, D., Lundquist, J
- Nov. 2014 **46th Annual Meeting Division for Planetary Sciences**, Tuscon, AZ
 “A 1-D Cryothermal Model of Ceres’ Megaregolith: Predictions for Surface Vapor Flux, Subsurface Temperatures and Pore Ice Distribution.”
Reynolds, D. Wood, SE. Bapst, J. Mehlhaff, Joshua. Griffiths, SG
- Virtual
- February 2022 **3rd International Conference on Snow Hydrology**
 “Improvements to an intermediate complexity atmospheric model for high-resolution downscaling in very complex terrain.”
Reynolds, D., Kruyt, B., Gutmann, E., Jonas, T., Lehning, M., Mott, R.
- April 2021 **EGU General Assembly**
 “Improvements to an intermediate complexity atmospheric model for high-resolution downscaling in very complex terrain.”
Reynolds, D., Kruyt, B., Gutmann, E., Jonas, T., Lehning, M., Mott, R.
- December 2020 **AGU General Assembly**
 “Improvements to an intermediate complexity atmospheric model for high-resolution downscaling in very complex terrain.”
Reynolds, D., Kruyt, B., Gutmann, E., Jonas, T., Lehning, M., Mott, R.

Fellowships and Awards

- 2022 **International Symposium on Snow, Davos**, *Early Career Scientist Presentation Award*
- 2017-2018 **Mary Gates Endowment, University of Washington**, *Mary Gates Undergraduate Research Scholarship*
- 2017 **University of Washington Global Sustainability Case Competition**, *1st Place Oral Presentation Award*
- 2015-2018 **Washington NASA Space Grant Consortium**, *NASA Space Grant Undergraduate Scholarship*

Outreach

- 2017–2019 **UW Engineering Discovery Days**, *Civil and Environmental Engineering, University of Washington, Seattle, WA*
- Running a science fair stand teaching the importance of mountain snow packs to local K-12 students

- 2017 **Middle School Science Fair Mentor**, *Bryant Middle School*, Seattle, WA
- Worked with a group of Middle School kids to design, conduct, and present a science experiment to measure gravitational acceleration

Technical Skills

Programming Languages

Proficient in: Python, Fortran, Unix/Bash, **Experienced in:** Java, C++, C#, HTML
GDAL, \LaTeX

Geophysical Models

Proficient with: HICAR/ICAR, FSM2, WRF, **Familiar with:** Structure for Unifying Multiple
COSMO, SnowModel Modeling Approaches (SUMMA), DHSVM

Field Work

Training with: ADCP+WinRiver, ADV, Salt Discharge Measurements, Harnessed Tower Climbing